Molecular Dynamics Study of Heat Transfer between Dissimilar Materials

by

Chen Shao

A dissertation submitted in partial fulfillment of
the requirements for the degree of
Doctor of Philosophy
(Materials Science and Engineering)
in The University of Michigan
2014

Doctoral Committee:

Professor John Kieffer, Chair
Associate Professor Max Shtein
Associate Professor Kevin P. Pipe
Associate Professor Veera Sundararaghavan

Dedication

To my parents Zhengming Shao and Xijuang Zhang, for their unconditional support.

To my uncle Xianda Zhang, for his guidance and advise.

Last but most importantly, to my love, Jinghan Liu, for our years together and many more to come.

Acknowledgement

Table of Contents

List of Figures

List of Tables

List of Appendices

Abstract

Molecular organics have become materials of considerable interest for electronic devices, due to their low manufacturing cost. Thermal management is a crucial factor in microelectronics because of the high power density associated with miniaturization. In this thesis, molecular dynamics (MD) simulations are used to understand heat transfer process at organic-metal interfaces and to guide materials design for devices with controllable thermal transport properties.

A Hybrid-COMPASS force field for the copper phthalocyanine (CuPc) molecule has been developed and parameterized using ab initio and empirical parameterization techniques. The valence parameters and atomic partial charges were derived by fitting to ab initio calculation results, and the van der Waals (vdW) parameters were derived by comparing MD simulations of CuPc crystal structures to experimentally determined characteristics. The resulting force field successfully predicts accurate molecular structure, crystal structure, and vibrational density of states (VDOS) of CuPc molecule in isolation and in condensed phase. Thermal conductivities for both crystalline and amorphous phase of CuPc are calculated using the Green-Kubo formalism. Calculation results show reasonable agreements with experimental measurements and a significant difference between crystalline and amorphous CuPc. Further analysis of the thermal conductivity spectral modes reveals that this difference mainly stems from the scattering of acoustic phonons, and to a lesser extent from the suppression of optical phonon modes

in the amorphous structure. Accordingly, phonon scattering at amorphous domain walls in nano-crystalline materials effectively eliminates over half of conduction pathways.

The newly optimized force field provides a great means for carrying out a systematic study of the nanoscale processes that govern thermal transport at CuPc/metal interfaces. Non-equilibrium MD simulations (NEMD) are performed on metal–CuPc–metal junctions using the Müller-Plathe method. Also, by varying the density and modulus of a structurally congruent test system, interfaces with matched and mismatched acoustic impedance or speed of sound are constructed and characterized. These simulations show that the traditional acoustic mismatch model (AMM) does not accurately describe heat transfer across weakly bonded interfaces. On the other hand, when controlling the interfacial bonding strength in MD simulations directly by scaling the interaction parameters for the materials juxtaposed at the interface, we find that the thermal boundary conductance is closely related to this interfacial bonding strength. By comparing the MD calculation results with the experimental measurements, the work of adhesion between CuPc and metal substrates is estimated to be 0.046 ± 0.014 J/m^2 for CuPc/Ag, 0.095 ± 0.004 J/m^2 for CuPc/Ag, and 0.439 ± 0.1 J/m^2 for CuPc/Al interfaces. These findings confirm the experimental observation of very weak bonding between CuPc and Au or Ag, and stronger bonding at the CuPc/Al interface. Phonon spectral analysis shows that the majority of heat transfer between CuPc and Au is accomplished via anharmonic coupling, which appears to be facilitated by strongly adhesive interfacial bonding.

The insight gained in the study of factors to influence heat transfer at weakly bonded organic-metal interfaces is further used to design materials with controllable thermal transport properties. MD simulations reveal that the thermal transport properties of piezoelectric polymers such as poly(vinylidene difluoride) (PVDF) thin films depend on the magnitude and direction of externally applied electric fields. Accordingly, the thermal conductivity of PVDF thin films increases with the strength of the applied electric field. Our simulations predict a 33% conductivity boost at 80% of the breakdown field strength. A poled PVDF film possesses a remnant conductivity enhancement that can be removed by an opposing electric field. Finally, the applied electric field raises the adhesive force to the substrate and thereby increases the interfacial thermal boundary conductance by a factor of up to 6. We elucidate the observed behaviors by comparing the phonon spectra of PVDF structures exhibiting various degrees of polarization. Accordingly, the effect of electric fields, either externally applied or resulting from the residual dipole moment of a poled structure, is to distort the structure during reorientation so as to cause a stiffening in the bonding structure, which in turn enhances the phonon contributions to the thermal conductivity.

Overall solid understanding has been achieved in heat transfer at organic-metal interfaces, where anharmonic coupling contributes to most of the transport process. Interfacial bonding strength is identified as dominant factor facilitating this heat transport. Furthermore, MD simulations predict the possibility for active control of thermal conductivity and interfacial conductance in the PVDF-metal system, and helped us identify the underlying materials design principles.

Chapter 1 Introduction

1.1 Thermal management at nano-scale

Technologies have been advancing rapidly in the past few years in the design and manufacturing electro-mechanical devices at micro and nanometer length scales. As the limits of classical and continuum theories are reached, phenomena that may be insignificant at large length scales can become dominant such as interfacial effects etc. Thermal management is one of the important factors to consider when designing devices, especially at nano-scale as the dimensions of the manufactured devices have become smaller and smaller.

One good example of the importance of thermal management would be the application in light emitting diodes (LED) technology. In LED devices, the injected electrical energy is converted into both light and heat. Today, the efficiency of commercially available LEDs is about 10% - 20%, meaning the rest 80% - 90% energy will need to be dissipated as heat.[1] With current research focusing improving light emitting efficiency that boosts the development of the LED technology, it is reported that the luminous output is doubled very 18 to 24 months.[2] This requires better thermal management to conduct heat from LED package to the environment.

Figure 1.1 shows a schematic diagram of typical architecture of LED module. It contains an LED package, thermal solution and a board for electrical and thermal connection.[3]
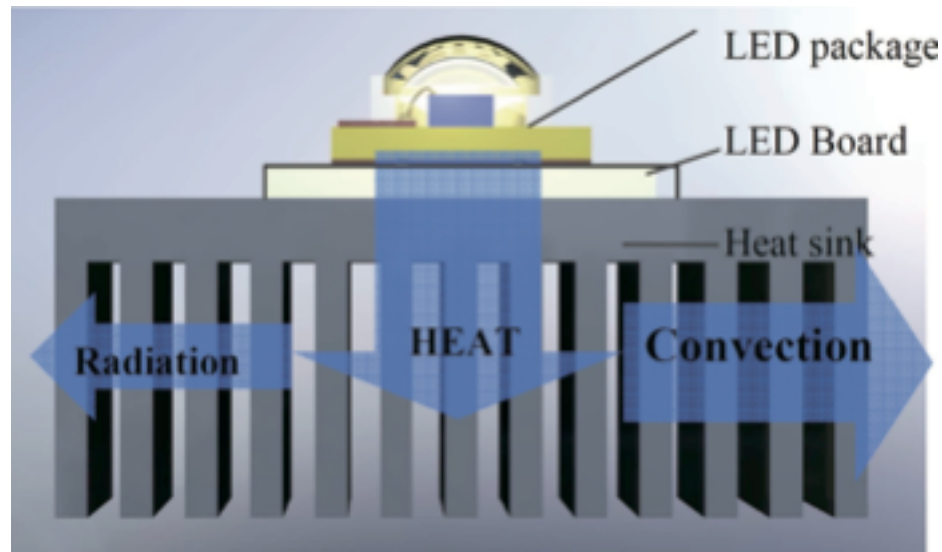
1. Figure 1.1 Schematic diagram of thermal path of LEDs. Huaiyu et al. *Journal of Semiconductors* **32,** 014008 (2011)

In the LED package, the chip is enclosed in a package of polymer lens and plastic carrier holder. Heat is generated by the chip inside the package and most of the heat will be conducted to the heat sink despite some can be dissipated by radiation and convection along the package surfaces. In order to maximize the heat transfer rate, we need to minimize thermal resistance in the module. In addition to using materials with high thermal conductivity such as carbon nanotubes, grapheme, etc., interface effects become crucial in the heat transfer process. In LED module, thermal interface materials (TIMs) are used to connect different components and studies show that 60% of thermal resistance in the system is in TIMs.[4] This type of thermal resistance at interface is called Kapitza

resistance or thermal boundary resistance. Detailed discussion of thermal conductivity and Kapitza resistance can be found in section 1.2.

Conversely, in applications such as thermoelectric devices, low heat transfer rate is desired for better performance. In metals or semiconductors, charge carriers carry both heat and charge. When a temperature gradient is applied to such material, the mobile charge carrier at the hot end will diffuse to the cool end. Eventually, this process will reach a steady state where the chemical potential for diffusion balances the electrostatic repulsion build up due to the charge accumulation of the carriers. This effect is named Seebeck effect and is the basis of thermoelectric devices enabling thermoelectric devices to collect waste heat to produce electrical energy or to serve as a refrigerator for cooling purpose. Figure 1.2 shows a thermoelectric module with direction of charge flow on both cooling and power generation.[5]
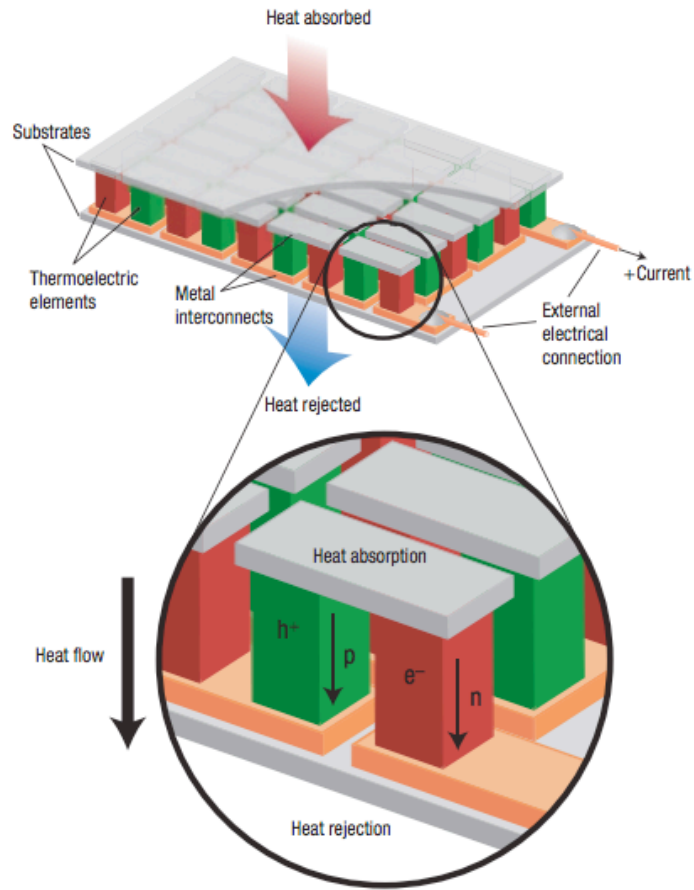
1. Figure 1.2 Thermoelectric module with direction of charge flow. Snyder &

Toberer, *Nature materials* **7,** 105-114 (2008)

Thermoelectric devices contain many thermoelectric couples consisting of both n type and p type thermoelectric elements wired electrically in series and thermally parallel. The efficiency of a thermoelectric material is determined by its figure of merit (*ZT*):

$$ZT = \frac{\alpha^2 T}{\rho \kappa} \qquad (1.1)$$

where α is the carrier concentration, T is absolute temperature, ρ is electrical resistivity, and κ is thermal conductivity. To increase the efficiency of thermoelectric device, we need to maximize its figure of merit by either increasing carrier concentration, by reducing thermal conductivity, or by reducing electrical resisticvity. Many times semiconductors are favored in making thermoelectric devices because people can dope semiconductors and increase carrier concentration α and thus increase *ZT*. For the past few decades, reducing resistivity ρ as well as thermal conductivity κ is the key focus in thermoelectric research. It should be noted that the thermal conductivity in thermoelectric devices comes from two sources: (1) electrons and holes transporting heat (κ_e) and (2) phonons travelling through the lattice (κ_p). So the κ in eqn. (1) should be written as:

$$\kappa = \kappa_e + \kappa_p \qquad (1.2)$$

and most of the electronic term κ_e is directly related to the electrical conductivity through the Wiedemann-Franz law:

$$\kappa_e = L\sigma T = ne\mu LT \qquad (1.3)$$

where L is the Lorenz factor, $2.4 \cdot 10^{-8}$ $J^2K^{-2}C^{-2}$ for free electrons. From eqn. (3) we can see that essentially κ_e and ρ has an inverse relation and the two cancels each other out. Therefore to maximize *zT*, we need to have a material with phonon thermal conductivity as low as possible.

The above examples are just two of many applications where thermal management is crucial in determining the performance of the devices. Although many efforts have been exerted to study and to understand the fundamental science of thermal

transport, there are still a lot that remains unknown. This thesis is thus motivated to study heat transfer process at interfaces of dissimilar materials.

1.2   Thermal boundary resistance and theoretical models

To study the heat transport at interface, we need more than just simple thermal conductivity of materials to consider. The thermal conductivity is defined as the constant of proportionality relating the temperature gradient ∇T and the heat flux q in a bulk material as:

$$q = -k\nabla T \qquad (1.4)$$

This is the Fourier law of conduction and was originally formulated based on empirical results. For two different materials joining at interface, the temperature is usually not continues across the interface. Such phenomenon was first reported by Kapitza in 1941 in his measurements of temperature drop near the boundary between helium and a solid when heat flows across the boundary. It is therefore the thermal boundary resistance is sometimes called Kapitza resistance. Essentially, the thermal boundary resistance is a measure of interface's resistance to heat flow and is defined as:

$$R_b = \Delta T \cdot q \qquad (1.5)$$

where ΔT is the temperature discontinuity at the interface and q is the heat flux passing through the interface. Taking the inverse of the thermal boundary resistance would result in the thermal boundary conductance. Similarly to thermal conductivity, both the energy carriers such as electron and holes and phonons contribute to thermal boundary

resistance. This thesis will focus on the organic material/metal interfaces and the contribution from phonons will dominate the thermal boundary resistance in these systems. Therefore the thermal boundary resistance is mainly determined by the number of phonons incident on the interface, the energy carried by each phonon, and the probability that each phonon is transmitted across the interface. The difficult part in theoretical study of the boundary resistance would be to model the transmission probability correctly.[6,7]

Two primary models have been developed and improved over the years to understand thermal boundary resistance. They are acoustic mismatch model and diffuse mismatch model respectively.

The acoustic mismatch model treats the phonons as plane waves. The materials in which the phonons propagate are treated as continua (no lattice). With these assumptions, the simplest picture derivable from the acoustic mismatch model is that each material can be ascribed an acoustic impedance equal to the product $Z_i = \rho_i c_i$ of the mass density and phonon velocity. For a phonon with normal incidence, the energy transmission probability looks like:[8]

$$\alpha_{1 \rightarrow 2} = \frac{4 Z_1 Z_2}{\left(Z_1 + Z_2\right)^2} \qquad (1.6)$$

A crucial assumption made in the acoustic mismatch model is that no scattering occurs at the interface and the theory does not distinguish between various phonon wavelengths. While such assumption is reasonable at very low temperature where the phonon

wavelength is larger than the surface roughness, it is not accurate at higher temperature where phonon wavelength decreases and compromises the theory.[6]

The second theory is the diffuse mismatch model (DMM) and assumes all the phonons incident on the interface will scatter diffusively. The DMM phonon boundary transmission probability can be approximated as:

$$\alpha_{1 \to 2} = \frac{\sum_i u_{p,2,i}^{-2}}{\sum_i u_{p,1,i}^{-2} + \sum_i u_{p,2,i}^{-2}} \qquad (1.7)$$

At high temperatures, DMM results are in better agreement with experimental measurements. Due to such assumptions made in these two models, neither of them are accurate enough for the thermal boundary resistance prediction and usually serves as upper and lower limit in the boundary resistance calculations. In addition, in both models, continuum materials are assumed, meaning the two materials would have strong bonding connection. However in many real world applications, only weak van der Waals interactions are present at the interfaces such as the organic-metal interface, meaning the materials are not continuous and the assumptions from the models will not hold. In these circumstances, these models would result in large deviations from the experimental measurements and fail to provide useful insights. Therefore new models and techniques are in great need to further understand the heat transfer process at interfaces.

1.3   Experimental challenges

Experiments are the foundation of scientific research and no theory is valid unless it is proven by experiments. As the research reaches smaller and smaller length scale, even with the constant evolution of experimental techniques, it becomes more and more challenging to design and conduct experiments, especially when the experiment is designed to study materials' interfaces. There are many factors that influence property of the interface, such as interface roughness, defects, adhesion etc. For the organic-metal systems that the thesis would focus on, many challenges are difficult to overcome in experiments. It is very difficult to get a sample with clean organic surface in experiments to start with, not to mention isolating a single factor to analysis at the interface. Moreover, characterization of interfaces is also difficult in experiments and it is almost impossible to measure properties of interfaces such as roughness or adhesion strengths without destroying the sample. Computer simulations offer a convenient way to study and analyze properties of materials at atomistic scale and has many advantages over experiments such as easiness of constructing interface systems, fast simulation setup, ability to control specific factors during simulations etc. Therefore this thesis will focus on the simulation study of heat transfer at interfaces.

1.4   Simulation Techniques

In simulation, one builds a model of real system and explores its behavior. The model is a mathematical description of the system and computational power has been used to expedite exploration process. Over the years, many simulation techniques have

been developed and now two of the many are most popular in atomistic simulations: density functional theory (DFT) calculations and MD simulations.

Quantum mechanics provides a reliable way to calculate behaviors of electrons and atomic nuclei in any situation and thereby offering us a means to understand the properties of any material from first-principles, that is, based on fundamental physical laws and without using free parameters, by solving the Schrodinger equation for the electrons in that material. However, one can quickly run into calculation difficulties due to the manybody interaction of electrons. Anything more complex than a hydrogen atom needs to be solved numerically and even the computer power seems to run out if the modeling systems contain a few handfuls of atoms. The birth of density functional theory (DFT) greatly simplifies the calculation process. DFT starts with two deceptively simple principles: (1) the total energy of a system of electrons and nuclei is a unique functional of the electron density, and (2) the variational minimum of the energy is exactly equivalent to the true ground-state energy. By throwing out the fearsome multidimensional wavefunction and instead working with a simple scalar field, the degree of simplification is immense and therefore allows first-principles calculations to be conducted on larger modeling systems.[9,10] Nonetheless, the system size is still a limiting factor in DFT calculations despite all the efforts in the past to improve the computational power. Based on the current cluster computing power, systems containing more than 1000 atoms would not be practical for DFT predictions.

By ignoring the electrons and performing classical calculations at atomistic level, the computational demands are greatly reduced. In MD simulations, the forces from

interacting atoms are calculated from empirical potentials of the atoms, and the position of the atoms are predicted at each time step according to Newton's second law. Given appropriate empirical potentials, materials structures containing interfaces can be constructed to simulate real systems. Compared to DFT calculations, MD simulations have two major advantages: (1) systems in MD simulations can contain hundreds of thousands of atoms, which is far larger than a typical system under DFT calculation and thus makes modeling amorphous materials possible in MD, (2) DFT focus on the ground state calculation while MD simulation takes temperature into calculation and able to study dynamic properties of materials. With the ability to predict the positions of atoms at every time steps, MD simulation allows us to directly observe the structure evolution at the interface during a simulation, which in experiments is almost impossible to observe. Compared to experimental techniques, MD simulation provides a powerful ability to control specific factors in a virtual structure during simulation. Thus, it enables us to systematically study the influence of different factors on transport phenomenon at materials interfaces at a microscopic scale.

1.5 Generating realistic interface structures

In MD simulations, the force field or empirical potential that defines interactions of atoms determines the success or failure of an MD simulation. Therefore the force field needs to be parameterized carefully to experimental measurements or DFT calculation results because the ground state calculation results from DFT are of high accuracy and can serve as the reference value during parameterization. There are several types of interactions that need to be modeled in a force field, which include bonds (interaction

between two bonded atoms), angles (interaction between two bonds), dihedrals (planar angles), and non-bond interactions such as Coulomb and van der Waals interactions. Different functional forms are chosen to model the various types of interactions. The general procedure to parameterize can be divided into two parts: (1) intra-molecular parameterization can be done with the help of DFT calculations (2) non-bond parameters can be obtained by adjusting force field parameters to reproduce experimental measurements such as density etc.[11] For the intra-molecular parameters, we first need to optimize the structure of the target molecules. Then part of the optimized molecule is shifted in space and DFT calculation is used to obtain the single point energy of the shifted structure. Eventually we can get an energy surface with respect to atomic displacements and parameters are then obtained by fitting the force field functions to the calculated energy surface from DFT.[12] Multivariate optimization algorithms are used for the fitting, MATLAB code have been developed for such purpose and is attached in Appendix A. Following these procedures, we can assure the models can successfully reproduce atomic structures in dynamics environment where thermal effect is important.

This thesis focuses on the interface between organic molecules and metals. One of the systems that we explore is the copper phthalocyanine (CuPc) and metal interface. After the force field parameters are optimized with the above procedures, absorption simulations have been conducted to explore if the simulation results successfully predict experimental observations. In Fig. 1.3 (a) and (b), the DFT prediction and high resolution STEM image of FePc absorption on Au (111) surface at saturate coverage are presented. Although we are interested in CuPc, both CuPc and FePc molecule share similar property

and almost the same structure.[13] Therefore we compare our absorption of CuPc on Au (111) results (Fig. 1.3 (c)) to the experimental measurements.
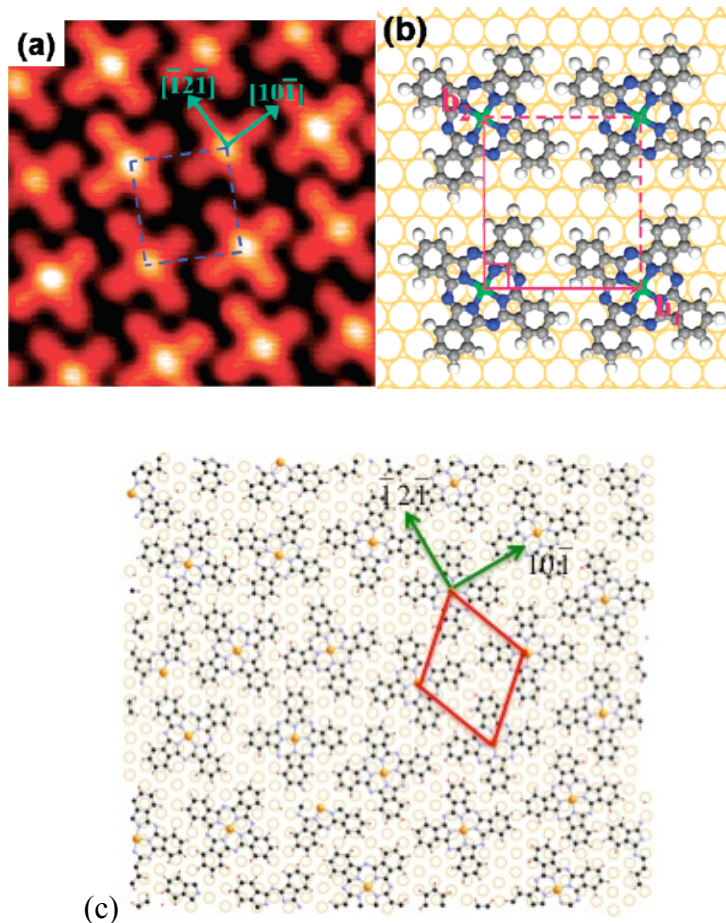
Figure 1.3 (a) High-resolution STM image of FePc on Au(111) surface at saturated coverage (6 nm by 6 nm, V=-0.4 V, I=0.05 nA). (b) Model for one unit cell of FePc molecule monolayer on Au(111). Cheng et al. *The Journal of Physical Chemistry C* **111**, 9240-9244 (2007). (c) MD simulation of CuPc absorption on Au (111)

Due to the limitation of system size and time frame under MD simulation, it is extremely difficult to obtain fully saturated coverage of CuPc molecules. However, the

CuPc layer still assembles key characteristics observed from experiments and tends to form packed domains on Au(111) surface.

Another system that we explored is the SubPc/C_{60} interface. It is discovered in experiments that a tradeoff between open circuit voltage (Voc) and short circuit current (Jsc) occured when deposition order of the active layers in a (SubPc)/C_{60} organic photovoltaic (OPV) is inverted.[14] Such effect is shown in Fig. 1.4 and it is suspected that depending on the deposition order, the SubPc (dipole) orientation allows for a heterojunction comprised of disparate polaron pairs, which can be related to dissociation and recombination rate constants in the OPV specific diode equation proposed by Giebink *et al.*[15]

Despite matched J_X, J_{SC} of inverted device is much higher

$$J = J_{s0}\{\exp(qV_a/k_bT) - 1\} - q\,\eta_{PPd}J_X$$
$$\eta_{PPd} = k_{PPd}/(k_{PPd} + k_{PPr})$$

attributed to greater polaron pair dissociation efficiency

J_{SC} mA/cm²	model J_X	exp J_{SC}	η_{PPd}
std.	10.5	5.24	50%
inv.	10.3	7.47	72%

lower V_{OC}

inv. OPV

Ag	100 nm
MoO₃	4 nm
SubPc	13 nm
C60	30 nm
LiF	2 nm
ITO/SiO₂	

110219AL
Voc 0.87
Jsc 7.47
FF 55.0
η_P 3.55

std. OPV

Al	100 nm
BCP	10 nm
C60	26 nm
SubPc	14 nm
MoO3	1 nm
ITO/SiO₂	

101115AA
Voc 1.10
Jsc 5.24
FF 63.1
η_P 3.64

higher current density

Why is the V_{OC} so high? why are we trading V_{OC} for J_{SC}?

Figure 1.4 Tradeoff between open circuit voltage (V_{oc}) and short circuit current (J_{sc}) observed when deposition order of the active layers in a (SubPc)/C_{60} organic photovoltaic (OPV) is inverted. Experiments conducted by S. Morris et al.

DFT studies have been by H. Hashemi and X. Ma et al[16] to identify the ground state of SubPc absorption on both C_{60} (100) and (111) surface. The interesting finding is that on the (111) surface, the SubPc molecule will stay on top of the C_{60} molecule with the halide containing Cl atom sticking perpendicular out of the surface, while for the (100) surface, SubPC buries its halide in between C60 molecules, offering the tripod of aromatic rings as the substrate for the second growth layer. The configuration of (100) surface ground state is shown in Fig. 1.5
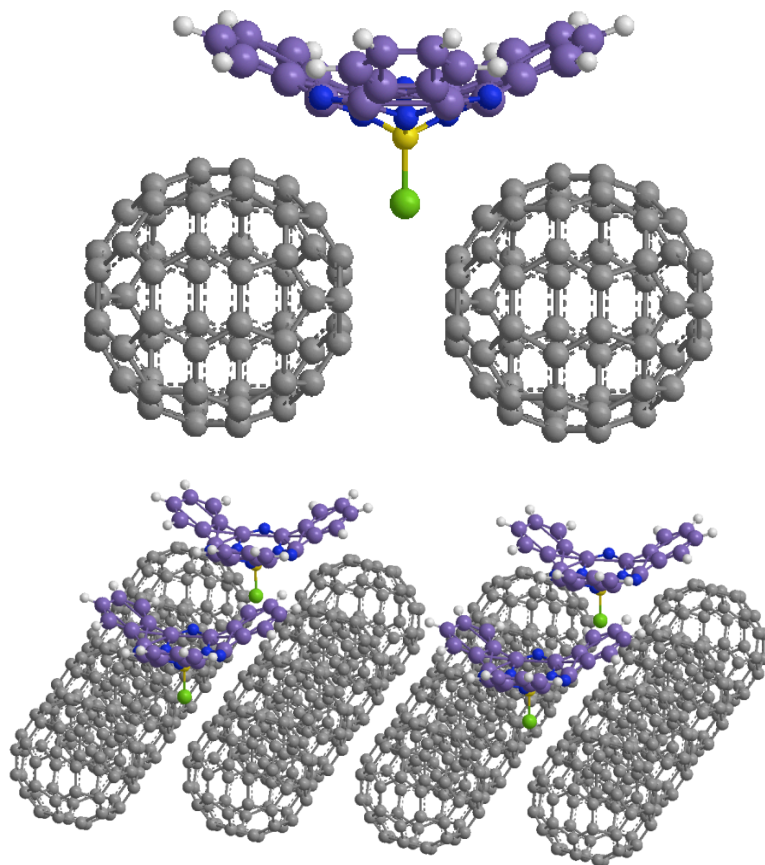
Figure 1.5 Most favorable site for SubPc absorption on C_{60} (100) surface. Simulation studies conducted by H. Hashemi et al.

With the appropriately developed force field parameters for SubPc and C_{60} molecules, MD simulations have also been used to explore temperature influence on the absorption of SubPc. For the (111) surface, the SubPc molecule will stay in the upward position due to the close-packed nature of the C_{60} (111) surface. For (100) surface, even if the SubPc starts with an upward position, the molecule will eventually flip and pursue the most energy stable site as predicted from the DFT study. The process is shown in Fig. 1.6.

(a) 0 ps
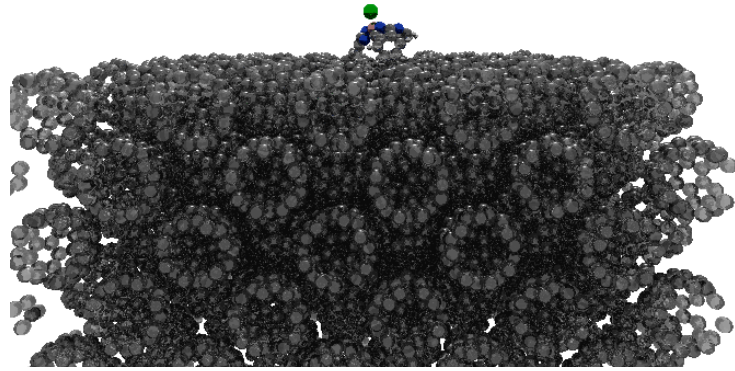
(b) 10 ps
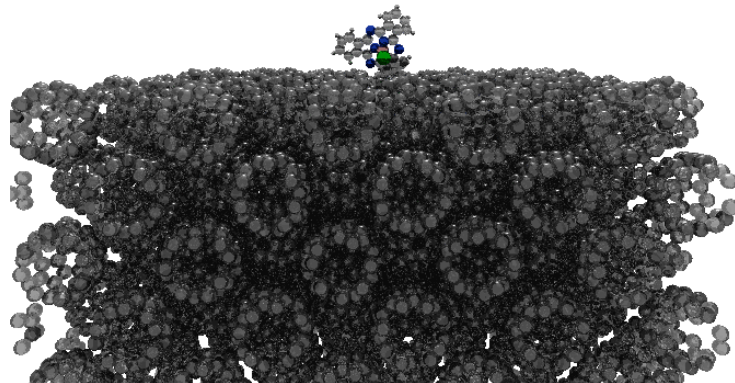
(c) 15 ps
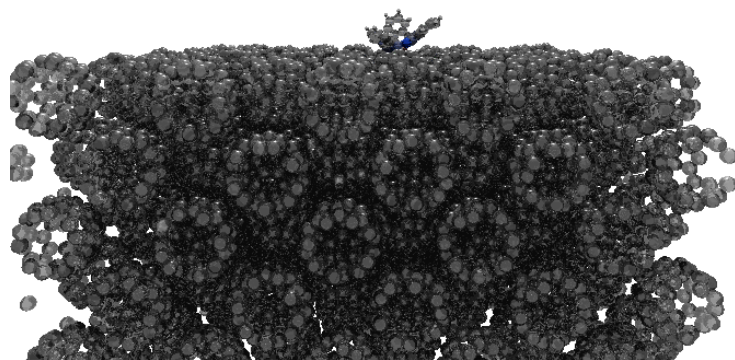
Figure 1.6 MD simulation of SubPc absorption on C_{60} (100) surface

It can be clearly seen that the MD simulations successfully predict same results as DFT calculations for single molecule absorption. It should be noted that under room temperature, as the number of molecules grows, some SubPc molecule will remain the upward position as a result of thermal fluctuation. These findings are all based on the careful parameterization procedure of the force field development and thus can provide useful insight and support to the explanation of experiment observations.

1.6 Thermal transport coefficient calculation in MD simulations

Two general approaches have been adapted to the calculation of thermal transport coefficients in MD simulations. The first approach is called Green-Kubo method and is based on the linear response theory, where the overall system is kept under equilibrium and the response of the system is analyzed when it is driven away from the equilibrium.[17] The steady state thermal conductivity of such equilibrium system is directly related to the time integral of the heat flux – heat flux correlation function. For a cubic isotropic system, the thermal conductivity is written as:

$$k = \frac{1}{3Vk_BT^2}\int_0^\infty \langle \mathbf{J}(0)\cdot\mathbf{J}(t)\rangle dt \qquad (1.8)$$

where $\langle\mathbf{J}(0)\cdot\mathbf{J}(t)\rangle$ is the time autocorrelation function of the heat flux in the equilibrium system. In MD simulations, a typical heat flux autocorrelation function would start with

large fluctuations, but the fluctuation would quickly die out and the autocorrelation function would reach zero and have only minor fluctuations as is shown in Fig. 1.7
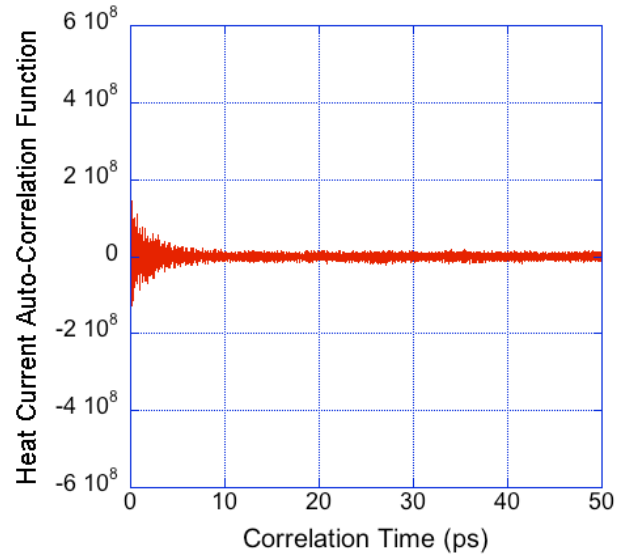
Figure 1.7 Plot of a typical heat current autocorrelation function vs. correlation time from MD simulation

The heat current autocorrelation function is then integrated over time to give thermal conductivity. The integral would first fluctuate and then converge to a certain value. Fig. 1.8 shows a typical plot of thermal conductivity vs correlation time in MD simulation and it is clear that the thermal conductivity value converges after about 10 ps correlation time.
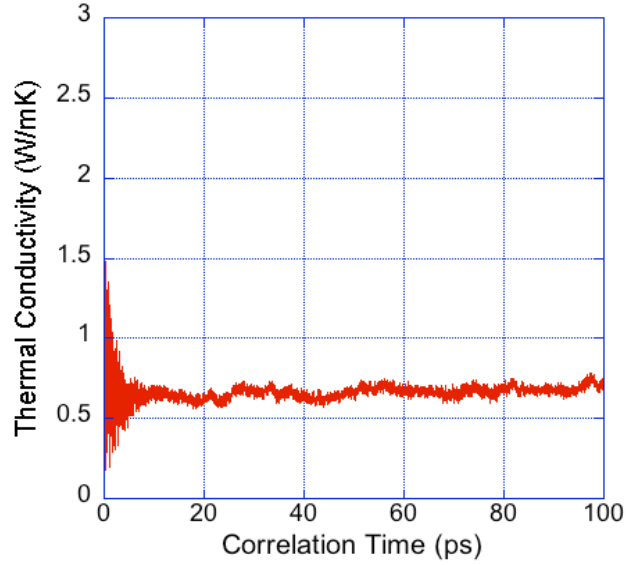
Figure 1.8 Typical plot of thermal conductivity vs. correlation time in MD simulation

The Green-Kubo relation is a generalized theory and is not limited only to the prediction of thermal conductivity. Similarly, an alternative version of equation (1.8) predicts the thermal boundary conductance in an equilibrium system.[18] as:

$$h_{1 \to 2} = \frac{1}{k_B T^2} \int_0^\infty \left\langle \dot{H}_1(0) \cdot \dot{H}_1(t) \right\rangle dt \qquad (1.9)$$

where H is the Hamiltonian of the material.

One major shortcoming of the Green-Kubo method is the computational resources and time it requires to get good statistics on the autocorrelation function. A few decades ago, Green-Kubo calculation may take months to finish and even with the help of super computer and parallel computing, it still needs weeks to get results with convincing statistics. Nonetheless, it is still a reliable method in predicting thermal conductivity

without introducing non-equilibrium conditions in the system, which may potentially bias the thermal transport calculation results.

The second approach is called Müller-Plathe method or non-equilibrium method, where a temperature source and a temperature sink is placed directly in the system. Temperature gradient is thus developed in the system and key parameters can be monitored simultaneously during the simulation process. The formalism uses the periodic boundary feature in MD simulations and divides the system into N slabs (Fig. 1.9).[19]
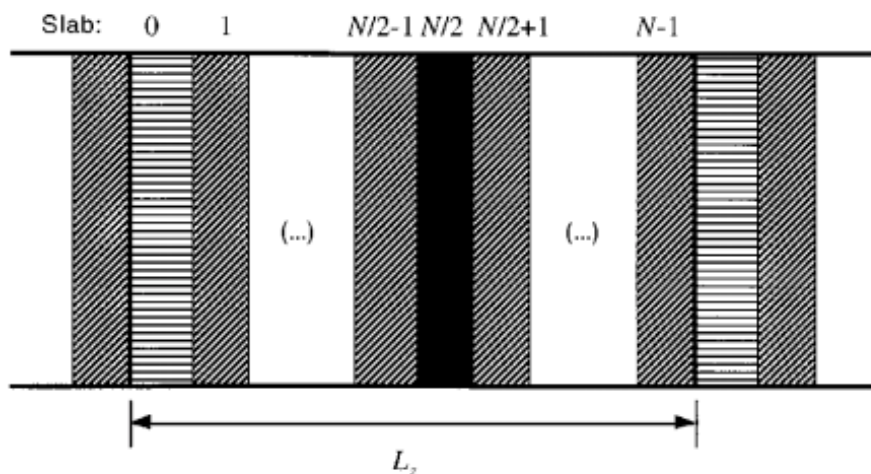
Figure 1.9 System setup for Müller-Plathe formalism. Müller-Plathe, *The Journal of chemical physics* **106,** 6082 (1997)

The slabs are labeled from 0 to N-1 and slab 0 is set to be "cool" slab and N/2 as the "hot" slab. Kinetic energy is transferred from hot slab to cool slab. This is done by exchange velocity vectors of the coolest atom in the hot slab (atom with minimum kinetic energy) with the velocity of the hottest atom in the cool slab. The energy is then flowed back from hot slab to cool slab by heat conduction. Once the system reaches steady state,

the energy transfer imposed by the artificial velocity exchange is exactly balanced by the heat flux in the opposite direction affected by the thermal conductivity of the system. Since one can easily calculate the exchanged kinetic energy, the heat flux is therefore calculated. The temperature profile can be calculated by determining the temperatures in the intervening slabs. The kinetic energies of each atoms are averaged to calculate the temperature of the slab. In general, several thousand of atoms should be included in the slab to achieve reliable statistics for the temperature calculations. A typical temperature profile is shown in Fig. 1.10 for a uniform system.[19]
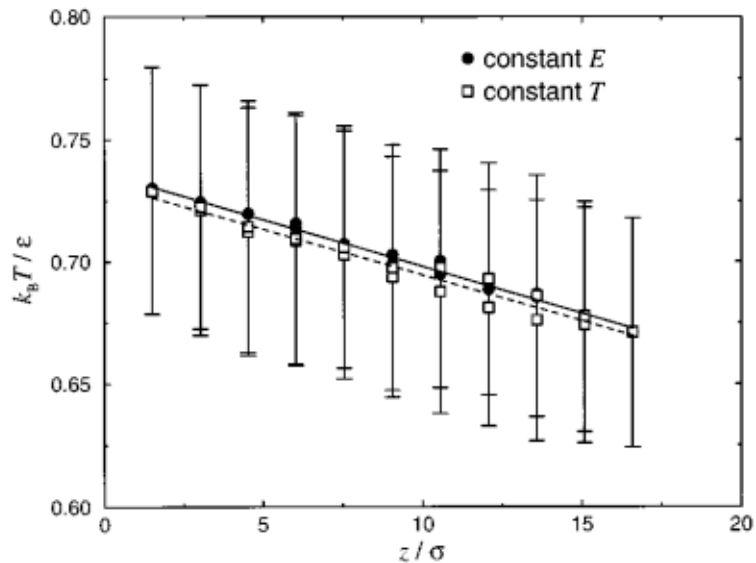
17. Figure 1.10 Typical temperature profile using Müller-Plathe formalism. Müller-Plathe, *The Journal of chemical physics* **106,** 6082 (1997)

If there is a interface in the system, one would observe temperature discontinuity from the temperature profile, which allows the calculation of ΔT in equation (1.5) for thermal boundary resistance prediction.

The Müller-Plathe method has many advantages such as easy to understand, easy to implement in computational codes, moderate calculation time etc. In the work of this thesis, both the Green-Kubo and Müller-Plathe methods will be used in investigations.

1.7   Computational resources and thesis layout

To accomplish the work in this thesis, we use cluster computers from Center for Advanced Computing (CAC) in University of Michigan, Ann Arbor. The MD simulation package LAMMPS developed by Sandia National Lab is used for all the MD simulations. Some extensions have been made to the LAMMPS package in order to facilitate the computing needs in the work of this thesis. The source code for the new features of computing net dipole moment in system and velocity autocorrelation function (vacf) are included in Appendix B.

In the discussion above, we showed the motivation of this thesis as well as theoretical backgrounds needed for the research. The thesis will be organized in the following way to study heat transfer process at interface of dissimilar materials. In Chapter 2, new force field parameters will be carefully developed for CuPc and the force field is validated through many methods that the MD simulations of CuPc will produce comparable results to DFT predictions as well as experimental measurements. With the validated new force field, we then study the thermal boundary resistance at CuPc-metal

interfaces using MD simulations in Chapter 3. Traditional theories such as AMM and DMM will be discussed if they would be appropriate to predict thermal boundary resistance at such weakly bonded interface. Different factors that may influence the heat transfer process will also be discussed. In Chapter 4, with the knowledge that we gained in the CuPc-metal system, we further move forward and explore the possibility of actively control of the heat transport property of piezoelectric polymers such as PVDF. Both the thermal conductivity and the boundary resistance at PVDF-metal interface will be discussed. Finally we will present a summary of this thesis and the outlook in this field.

1.8 References

1. Petroski, J. Thermal challenges facing new-generation light-emitting diodes (LEDs) for lighting applications. **International Symposium on Optical Science and Technology**, 215-222 (2002).

2. Steigerwald, D. A. et al. Illumination with solid state lighting technology. *Selected Topics in Quantum Electronics, IEEE Journal of* **8**, 310-320 (2002).

3. Huaiyu, Y., Koh, S., van Zeijl, H., Gielen, A. W. J. & Guoqi, Z. A review of passive thermal management of LED module. *Journal of Semiconductors* **32**, 014008 (2011).

4. Tonapi, S. S. et al. An overview of thermal management for next generation microelectronic devices. **Advanced Semiconductor Manufacturing Conference and Workshop, 2003 IEEEI/SEMI**, 250-254 (2003).

5. Snyder, G. J. & Toberer, E. S. Complex thermoelectric materials. *Nature materials* **7**, 105-114 (2008).

6. Kaviany, M. *Heat transfer physics* (Cambridge University Press Cambridge, UK, 2008).

7. Swartz, E. T. & Pohl, R. O. Thermal boundary resistance. *Reviews of Modern Physics* **61**, 605 (1989).

8. Little, W. A. The transport of heat between dissimilar solids at low temperatures. *Canadian Journal of Physics* **37**, 334-349 (1959).

9. Hohenberg, P. & Kohn, W. Inhomogeneous electron gas. *Physical review* **136**, B864 (1964).

10. Segall, M. D. et al. First-principles simulation: ideas, illustrations and the CASTEP code. *Journal of Physics: Condensed Matter* **14**, 2717 (2002).

11. Sun, H. COMPASS: An ab initio force-field optimized for condensed-phase applications overview with details on alkane and benzene compounds. *The Journal of Physical Chemistry B* **102**, 7338-7364 (1998).

12. Maple, J. R., Dinur, U. & Hagler, A. T. Derivation of force fields for molecular mechanics and dynamics from ab initio energy surfaces. *Proceedings of the National Academy of Sciences* **85**, 5350-5354 (1988).

13. Cheng, Z. H. et al. Adsorption behavior of iron phthalocyanine on Au (111) surface at submonolayer coverage. *The Journal of Physical Chemistry C* **111**, 9240-9244 (2007).

14. Morris, S. et al. *submitted to APL*

15. Giebink, N. C., Wiederrecht, G. P., Wasielewski, M. R. & Forrest, S. R. Ideal diode equation for organic heterojunctions. I. Derivation and application. *Physical Review B* **82**, 155305 (2010).

16. Hossein., H. et al. in preparation.

17. Kubo, R. Statistical-mechanical theory of irreversible processes. I. General theory and simple applications to magnetic and conduction problems. *Journal of the Physical Society of Japan* **12**, 570-586 (1957).

18. Chalopin, Y., Esfarjani, K., Henry, A., Volz, S. & Chen, G. Thermal interface conductance in Si/Ge superlattices by equilibrium molecular dynamics. *Physical Review B* **85**, 195302 (2012).

19. Müller-Plathe, F. A simple nonequilibrium molecular dynamics method for calculating the thermal conductivity. *The Journal of chemical physics* **106**, 6082 (1997).

Chapter 2 Simulation of Crystalline and Amorphous Copper Phthalocyanine: Force Field Development and Analysis of Thermal Transport Mechanisms

Synopsis

The thermal conductivities of crystalline and amorphous CuPc structures have been studied using molecular dynamics simulations. To this end, a Hybrid-COMPASS force field for the CuPc molecule has been developed and parameterized using *ab initio* and empirical parameterization techniques. The valence parameters and atomic partial charges were derived by fitting to *ab initio* calculation results, and the van der Waals (vdW) parameters were derived by comparing MD simulations of CuPc crystal structures to experimentally determined characteristics. The resulting force field successfully predicts accurate molecular structure, crystal structure, and vibration density of states (VDOS) of CuPc molecule in isolation and in condensed phase. Thermal conductivities calculated using the Green-Kubo formalism show a significant difference between crystalline and amorphous CuPc. Further analysis of the thermal conductivity spectral modes reveals that this difference mainly stems from the scattering of acoustic phonons,

and to a lesser extent from the suppression of optical phonon modes in the amorphous structure. Accordingly, phonon scattering at amorphous domain walls in nano-crystalline materials effectively eliminates nearly two thirds of conduction pathways.

2.1   Introduction

Copper phthalocyanine (CuPc) was originally developed as a paint pigment, a dye for textiles and plastics, and for ballpoint pen inks, printing inks, and even as food coloring.[1] In 1948, Vartanyan and Khim reported the discovery of semiconductor behavior in CuPc.[2] Further research revealed good chemical stability and low photochemical activity, which made CuPc highly suitable and heavily employed in light emitting diodes, organic lasers, and solar cells. CuPc has also been used in chemical sensors[3] and optical data storage applications.[4, 5] The relatively complex geometry of the CuPc molecule can pose challenges for controlling the structural definition of interfaces CuPc thin films form with other materials in these devices, and further molecular design may be indicated to improve performance.

In this context, molecular simulations provide an efficient means for predicting the structure and properties of materials, and thereby guide the conception and optimization of molecular architectures before synthesis is attempted in the laboratory. Key to the correct prediction of materials is the ability to generate realistic materials structures, e.g., by reproducing the reaction and transport processes that underlie molecular assembly in experimental systems. For complex organic molecules this approach can be time consuming and we therefore must rely on molecular dynamics (MD) simulations based on empirical force fields, which provide for the efficient computation

of atomic trajectories. For a successful structure and property prediction, this force field must accurately describe atomic interactions.

To date, very few force fields have been developed specifically for metal phthalocyanine materials. Yin has developed the ESFF force field to study CuPc adsorption on graphite surface and alkane adlayer using molecular mechanics method.[6] Recently, Chen studied CuPc orientation and charge transport based on the CuPc crystal structure generated by MD simulation using CVFF force field.[7] Nonetheless, none of them characterize the thermo-mechanical properties of CuPc to the extent we deemed necessary. Therefore, our first task was to improve upon the current state-of-the-art. As a starting point we selected the COMPASS (condensed-phase optimized molecular potentials for atomistic simulation studies) force field because it is well-accepted for simulating organic molecules.[8-10] The COMPASS force field was introduced by Sun in 1998.[9] It is a "Class II" force field that evolves from previous force fields such as MM4,[11] CFF93,[12] OPLS,[13] etc. and it has been parameterized as a universal force field to study most common organic molecules, organic and inorganic polymers, zeolites, and metal/trasition-metal oxides. Indeed, a number of bonding interactions between species that are part of the CuPc molecule are available in the literature, have been directly adopted for the present study of CuPc.

In this chapter, we report new parameters for the Hybrid-COMPASS force field. Hybrid-COMPASS, proposed by Ionescu,[14] is a simplified version of the COMPASS force field with acceptable simulation accuracy. The first optimization step consists of adjusting interaction parameters so that the CuPc crystal structure reported in literature is

reproduced. Interaction energy magnitudes and local charges are obtained using first-principles calculations. Next, comparison between calculated and experimental phonon density of states serves to fine-tune the interaction parameters. Finally, the force field parameterization so obtained is validated by computing thermal conductivities for both crystalline and amorphous CuPc and directly compared with experimental measurements carried out in our laboratory. The remainder of the paper is organized as follows: first, we provide a detailed description of the force field used in this work, followed by the details of simulations procedure, including the determination of thermal conductivities. Subsequently, we analyze and discuss our findings regarding heat transport in amorphous and crystalline CuPc, and conclude with a summary of our findings.

2.2 Force Field Description

In the COMPASS force field, the potential energy, U, is given by,

$$U = U_b + U_\theta + U_\varphi + U_\chi + U_{bb'} + U_{b\theta} + U_{b\varphi} + U_{\theta\varphi} + U_{b\theta\varphi} + U_{coul} + U_{vdw} \qquad (2.1)$$

The potential energy (U) given in COMPASS force field can be divided into valence and non-bonding terms. The valence terms include bond-stretching (U_b), bond-angle-bending (U_θ), torsion (U_φ), out-of-plane bending (U_χ), cross-coupling terms (such as bond-bond ($U_{bb'}$), bond-angle ($U_{b\theta}$), bond-torsion ($U_{b\varphi}$), angle-torsion ($U_{\theta\varphi}$) and bond-angle-torsion ($U_{b\theta\varphi}$) interactions). The non-bonding terms are electrostatic interactions (U_{coul}) and van der Waals interaction (U_{vdw}). In the hybrid-COMPASS force field used here, the out-of-plane bending and cross-coupling terms are neglected, which greatly reduces the amount of parameters to be developed, without significantly sacrificing

accuracy in reproducing experimental observations. The functional forms of bond-stretching (U_b) and bond-angle-bending (U_θ) terms are described as

$$U_b = k_2 (b - b_0)^2 + k_3 (b - b_0)^3 + k_4 (b - b_0)^4 \quad (2.2)$$

$$U_\theta = V_2 (\theta - \theta_0)^2 + V_3 (\theta - \theta_0)^3 + V_4 (\theta - \theta_0)^4 \quad (2.3)$$

where b_0 and q_0 are equilibrium bond length and equilibrium bond angle, respectively. b and q are the equilibrium bond lengths and bond angles, and k_2, k_3, k_4, H_2, H_3, and H_4 are constants. The functional form of the torsional term is given by

$$U_\varphi = H_1 (1 - \cos\varphi) + H_2 (1 - \cos 2\varphi) + H_3 (1 - \cos 3\varphi), \quad (2.4)$$

where j is the equilibrium torsional angle and H_1, H_2, and H_3 are constants. The electrostatic interaction can be described by the Coulomb law,

$$U_{coul} = \sum_{i,j} \frac{q_i q_j}{r_{ij}} \quad (2.5)$$

where the atomic partial charges can be evaluated through bond increments, d_{ij}, which represent the charge transfer between two valence-bonded atoms i and j. Accordingly, for atom i, the resulting partial charge is the result of summing up all bond increments for valence-bonded atoms j,

$$q_i = \sum_j \delta_{ij} \quad (2.6)$$

Lennard-Jones 9-6 potential is implemented to model non-bonding van der Waals interactions. The functional form is given by

31

$$U_{vdw} = \sum_{i,j} \varepsilon_{ij} \left[2\left(\frac{r_{ij}^0}{r_{ij}}\right)^9 - 3\left(\frac{r_{ij}^0}{r_{ij}}\right)^6 \right] \qquad (2.7)$$

where r_{ij}^0 is the equilibrium distance between atom i and atom j. ε_{ij} and r_{ij}^0 for the same atomic species, $i = j$, we use published parameters for C, H, N and parameterize Cu-Cu interaction. For the parameters between different species, $i \neq j$, a 6th order mixing rule is applied,

$$r_{ij}^0 = \left(\frac{\left(r_i^0\right)^6 + \left(r_j^0\right)^6}{2} \right)^{1/6} \qquad (2.8)$$

$$\varepsilon_{ij} = 2\sqrt{\varepsilon_i \cdot \varepsilon_j} \left(\frac{\left(r_i^0\right)^3 \cdot \left(r_j^0\right)^3}{\left(r_i^0\right)^6 + \left(r_j^0\right)^6} \right) \qquad (2.9)$$

For non-bonding interactions, a cutoff distance of around $10 \sim 15$ Å is selected and it is assumed to be a sharp cutoff.[9]

2.3 Force field parameterization procedure

We determined the force field parameters for the CuPc molecule, shown in Fig. 2.1, using a method similar to that pioneered by Maple[15] and subsequently adopted by Sun[9, 10] and Bunte[8] in their quest to establish COMPASS force field parameters for a series of organic molecules. Empirical adjustments are also performed to achieve better results.
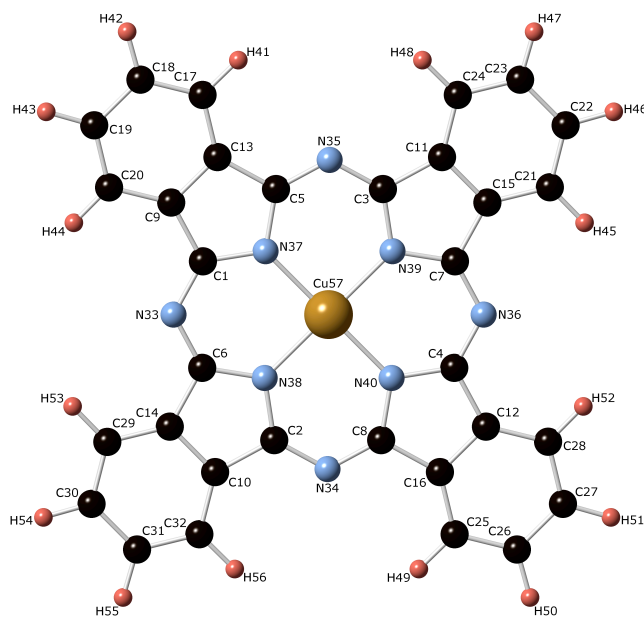
Figure 2.1 Copper phthalocyanine molecular structure

The valence bond parameters and charge bond increments are derived by least squares fitting the force field to the energy surface of a single CuPc molecule obtained by means of density functional theory (DFT) calculations using the B3LYP/6-311G(d,p) basis set. The optimized equilibrium structure of the CuPc molecule and the corresponding energy surface are obtained using the Gaussian 09 suite of quantum chemistry code, with the default convergence criteria in all cases. To fit the force field to DFT calculation results, we first compute atomic partial charges in the CuPc molecule using DFT calculation. These partial charges are then converted to charge bond increments, with some adjustments to maximize agreement between the two calculation methods for the entire molecule. The atomic partial charge for the copper atom is calculated to be +0.876 electronic charge units, which suggests that the bonding between copper and nitrogen is mostly covalent in nature and the functional form in Hybrid-

COMPASS force field is appropriate in this case. The valence bonding parameters are obtained by multivariate optimization of up to 10 force field parameters simultaneously, until the deviations between the energy surfaces for the CuPc molecule obtained from DFT calculations and MD simulations are minimized. Once the valence parameters are obtained, MD simulations are performed to optimize non-bonding interaction parameters and to validate the force field via its ability to reproduce other properties of CuPc based materials. MD simulations were carried out using LAMMPS simulation package. All the parameters needed to define the potential functions used in this work are listed in Table 2.1.

2.4   Simulation procedure Details

To validate the force field, we first study the intra-molecular properties by comparing the energy-minimized equilibrium structure of a single CuPc molecule resulting from MD simulations to the optimized equilibrium structure obtained from DFT calculation, as well as from experimental observations. Then CuPc crystal structures are studied to validate non-bonding parameters of the force field. Depending on temperature, CuPc can exhibit α-, β-, γ-, δ-, ε-, R-, π-, and X-forms. Among these eight polymorphs of crystalline CuPc , only the β-form has good thermal stability and all other forms convert to β-form when heated above 473 K.[16] Thus we perform MD simulations on CuPc crystals both at room temperature (300 K) and at elevated temperature (500K) in order to validate the α- and β-forms of crystalline CuPc structures corresponding to these temperatures. Both constant volume (NVT) simulation and constant pressure (NPT) simulations, with time integration based on Nose-Hoover style non-Hamiltonian

equations of motion, are performed using a time step of 1fs. Both conditions give identical system properties. Amorphous CuPc structure is also generated according to following procedures: CuPc molecules are loosely placed in space with intermolecular distance of 20 Å which is larger than the cutoff radius of the potential. The system is first equilibrated under NPT ensemble at 700K then cooled slowly to 300K for amorphous structure. Finally we calculate the vibrational density of states from MD simulation results and compare to the experimental IR/Raman spectra as well as the normal modes study of CuPc molecule.

2.5 Results and Discussion

2.5.1 Intra-Molecular Properties

A schematic of the CuPc molecule is shown in Fig. 2.1. In principle, atoms N33 and N37 represent two different types of nitrogen. However, for the purpose of keeping the Hybrid-COMPASS force field as simple as possible, we treat them the same, except for their coordination numbers. This latter attribute sufficiently differentiates the two types of nitrogen, so that the structure and dynamical properties of the molecule are reproduced with sufficient accuracy, as illustrated below. Energy minimization is performed on isolated a CuPc molecule. All 68 bond lengths and 116 bond angles are compared with the values obtained from DFT calculations. Fig. 2.2(a) and (b) show the correlation between MD and DFT results. For the bond lengths, the data range from 1.0 Å to 2.0 Å. The maximum absolute deviation is 3.2%, the average deviation is 0.68% and the root mean squares (rms) deviation is 1.8%. For the bond angles, the data range from

90$^\mathrm{o}$ to 135$^\mathrm{o}$. The maximum absolute deviation is 1.6%, the average deviation is -0.13%, and the rms deviation is 1.0%.

(a)
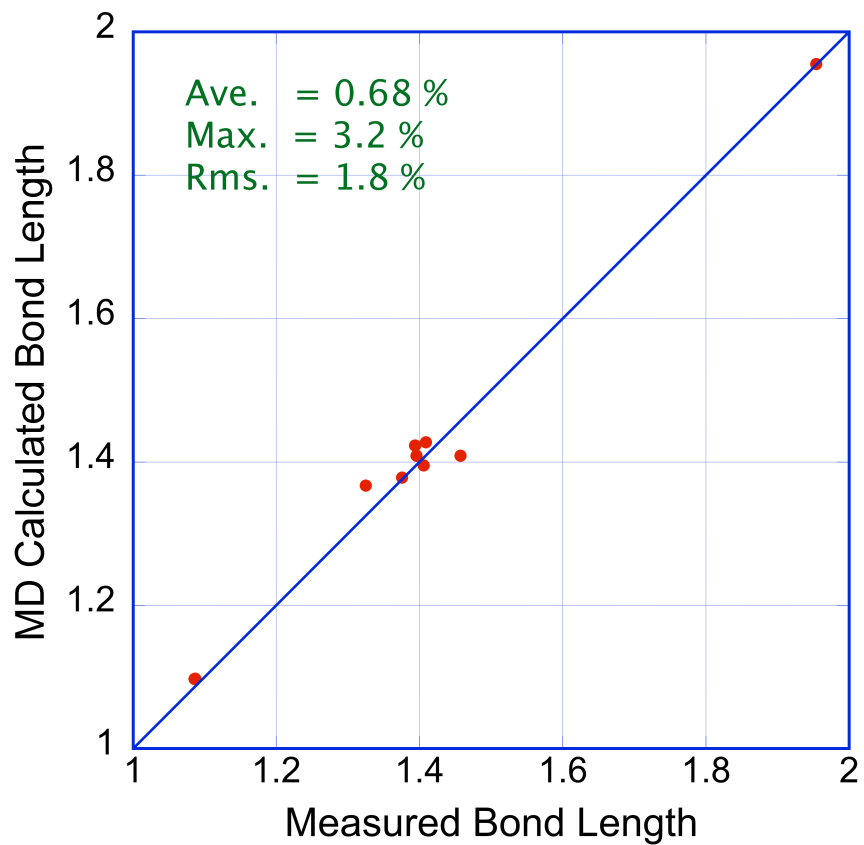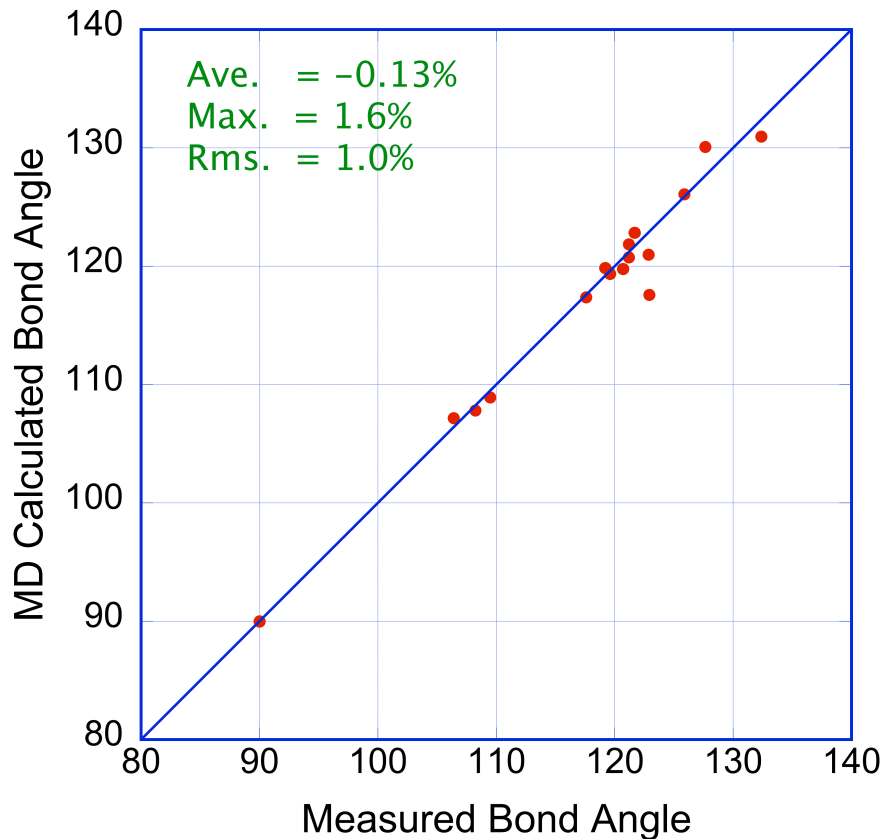
Figure 2.2 Comparison of (a) bond lengths and (b) bond angles calculated using our force field with experimental data. The maximum absolute percentage deviation (max), average percentage deviation (ave), and root mean squares (rms) percentage deviation are listed.

The detailed comparison between the bond lengths and angles obtained using MD simulations based on this force field, DFT calculations, and experiments is provided in Table 2.2 and Table 2.3. The atom labeling here is consistent with the labeling in Fig. 2.1. The dihedral angle of CuPc molecule is 180° in all three cases. Compared to experimental data, we find the bond length of C1-N33 to be 2.9% larger in MD simulation results, which is within the acceptable error range for these simulations. It is interesting to note that the C1-N33 type of bond (1.36 Å) is slightly shorter than C1-N37 type of bond (1.37

Å), which is in agreement with experimental observations and DFT calculations.[17] C. J. Brown proposed two possible explanations for this trend:[17] On one hand, this could be the result of the copper atom more strongly attracting the N37 atom; on the other hand the five-membered isoindole ring may have some influence on N37 atom by diverting some of π electrons away from N37 atom and thus cause the C-N bond to be longer. Since in our force field, N33 and N37 are treated the same, their interactions with neighboring carbons are identical, and hence, the influence of the copper atom appears to be sufficient to induce the difference in bond lengths. In general, the force field based calculation results of the bond lengths and bond angles are in excellent agreement with both experimental and DFT calculated values.

2.5.2 Vibrational Density of States

To further validate the force field, the vibrational density of states (VDOS), $D(w)$, is calculated by Fourier transform of the velocity autocorrelation function (VACF), according to

$$D(\omega) = \mathrm{Re}\left(\int_0^\infty \left\langle \frac{\mathbf{v}_j(t) \cdot \mathbf{v}_j(0)}{\left| \mathbf{v}_j(0) \right|^2} \right\rangle e^{i\omega t}\, dt \right) \quad (2.10)$$

where ω is the frequency and $\mathbf{v}_j(t)$ is the velocity of atom j at time t. Correlation with the velocity at time zero is assessed by computing the vector dot product, and the angular brackets indicate both the time and ensemble average of this quantity.

The calculated VDOS is then compared with the spectrum of normal mode frequencies obtained from DFT B3LYP/6-311G(d,p) calculations, as well as the

experimentally observed in Raman scattering and IR absorption spectra of CuPc.[18] The values are listed in Table 2.4. The standard deviation between normal mode frequencies due to interactions based on the force field and experimentally measured peak frequencies is 15.24 cm^{-1}, and the maximum deviation is 82 cm^{-1}. Both are considered acceptable for force field calculations. For the CuPc molecule all the normal mode frequencies below 1700 cm^{-1} are strongly correlated[19] and each normal mode involves motion along more than one direction in the internal coordinate system.[18] It is very difficult to obtain accurate vibrational spectra for such a complicated molecule, and previous efforts in calculating normal mode frequencies for CuPc molecule resulted in errors as large as 10%.[19] Accordingly, calculations based on our force field yield much better accuracy.

2.5.3 Crystalline Structure

The CuPc crystalline structure is obtained using constant pressure MD simulation of a 5 by 5 by 5 supercell, allowing for a more stringent test of structural stability. Fig. 2.3(a) and (b) show the supercell for α- and β-form of crystalline CuPc, respectively. The Parrinello-Rahman pressure control method, in which all cell parameters are relaxed, is used in these simulations. Unit cell parameters from simulations are averaged over the supercell and several oscillatory periods of the lowest-frequency cell shape fluctuations. Values so obtained for both the α- and β-form are listed, alongside experimental data, in Table 2.5 and Table 2.6. The maximum deviation between simulation-based and experimental values is 6.25%. The deviation in cell parameters for the α-form appears to be larger than that for the β-form of CuPc. This can be attributed to the relatively weak

van der Waals interactions between CuPc molecules, which are nevertheless responsible for the crystalline configurations these molecules assume. Consequently, the unit cell parameters of weakly bonded CuPc are very sensitive to the simulated environment. For CuPc, the α-form is metastable at ambient conditions, and easily transforms to the more stable β-form at elevated temperature. It is therefore to be expected that α-CuPc is characterized by shallow or even multiple local energy minima, and that precise location of these minima very delicately responds to potential parameter adjustments. As can be seen in Table 2.7, the calculated densities of both α- and β-CuPc crystals are in good agreement with experimental observations. Overall, we find the structural characteristics derived from MD simulations of this newly optimized force field to be very acceptable for such weakly bonded crystals.

(a)
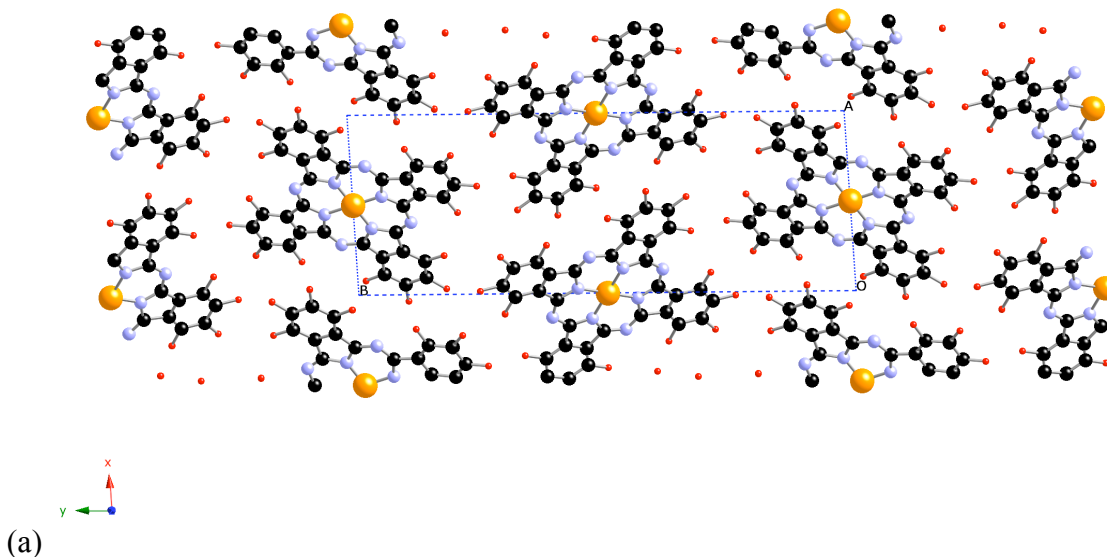
(b)
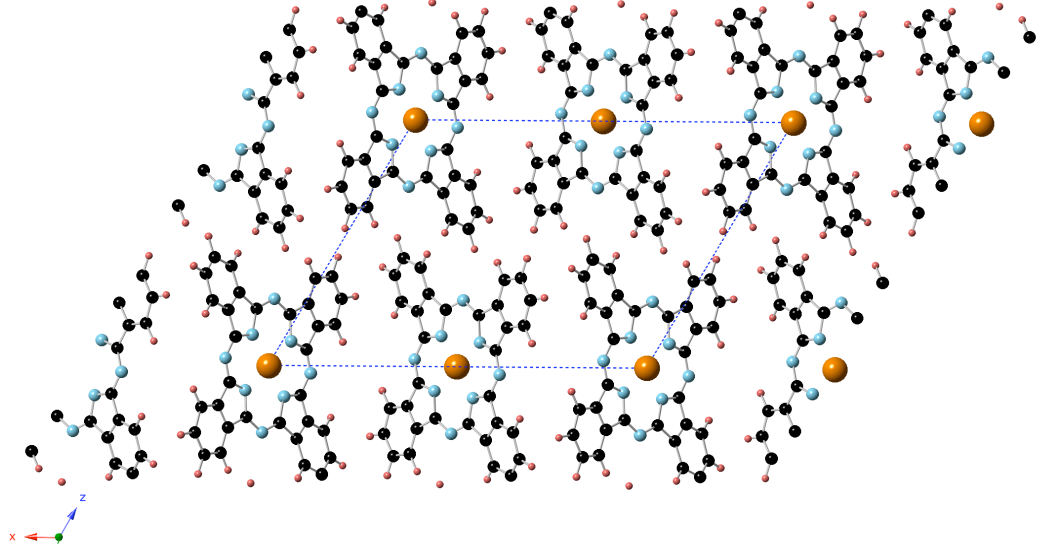
Figure 2.3 Unit cell structures of: (a) α-CuPc and (b) β-CuPc crystals

2.5.4 Thermal Conductivity of CuPc

At the molecular scale, materials are subject to small statistical temperature fluctuations, the spatio-temporal evolution of which is governed by instantaneous heat fluxes. The thermal conductivity of such a system can be calculated from the heat current autocorrelation function (HCACF) according to the Green-Kubo formalism:[20]

$$k = \frac{1}{Vk_BT}\int_0^\infty \langle \mathbf{J}(\tau)\cdot\mathbf{J}(0)\rangle d\tau \qquad (2.11)$$

where $\vec{J}(\tau)$ is the instantaneous heat current and the HCACF, $\langle \vec{J}(0)\vec{J}(\tau)\rangle$, is again time and ensemble averaged. V is the volume of the simulated system, and T is the mean temperature during the MD simulation. The instantaneous heat current is calculated as

41

$$\vec{J} = \frac{\partial}{\partial t}\left(\sum_j \vec{r}_j E_j\right)_,$$

(2.12)

where the summation is over all the atoms, and E_j is the total energy of atom j.

Both the crystalline β-form and amorphous structures of CuPc are created and relaxed at 300K and ambient pressure using NPT conditions using MD simulation. In Fig. 2.4, We plot the volume of the system vs. temperature during the cooling process to make amorphous CuPc structure. The glass transition temperature T_g in our simulation is about 518 K which is slightly higher than actual T_g of 513 K. The accurate T_g obtained by MD simulation validates the amorphous CuPc structure in simulation. X-ray diffraction (XRD) analysis on both crystalline and amorphous CuPc structures further validates the correctness of the structures used. The XRD patterns for both structures are calculated using the CrystalDiffract software and are shown in Fig. 2.5(a). The wavelength used in the calculation is 1.54 Å. In experiments, crystalline and amorphous CuPc films were deposited on silicon (100) substrates under different deposition temperature, 20 and -60 degree Celsius respectively. Their X-ray diffraction (XRD) spectra were obtained by Rigaku rotating anode X-ray diffractometer. The experimentally measured XRD for β-crystalline and amorphous CuPc are shown in Fig. 2.5(b).
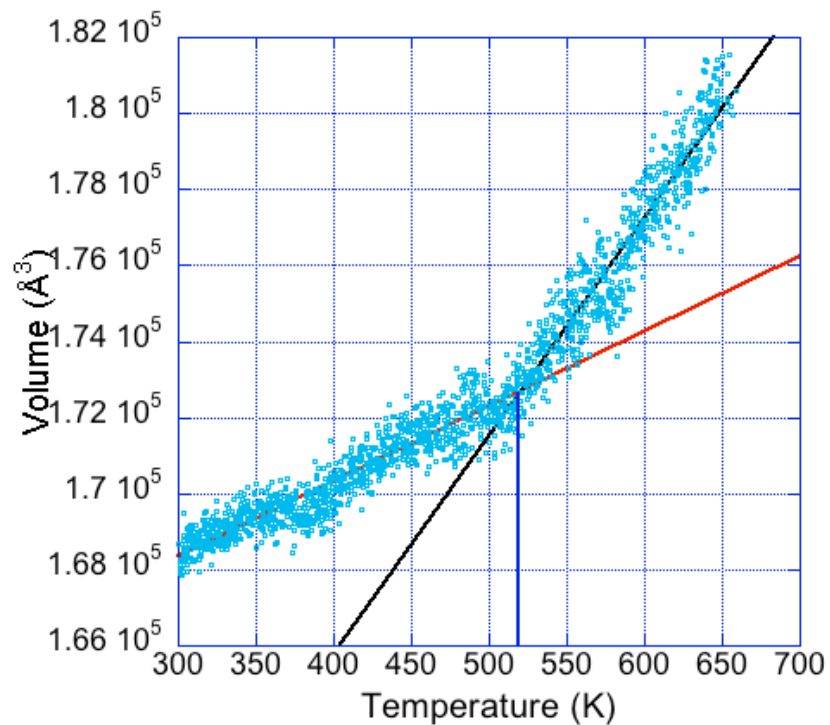
Figure 2.4 Plot of system volume vs. temperature for amorphous CuPc
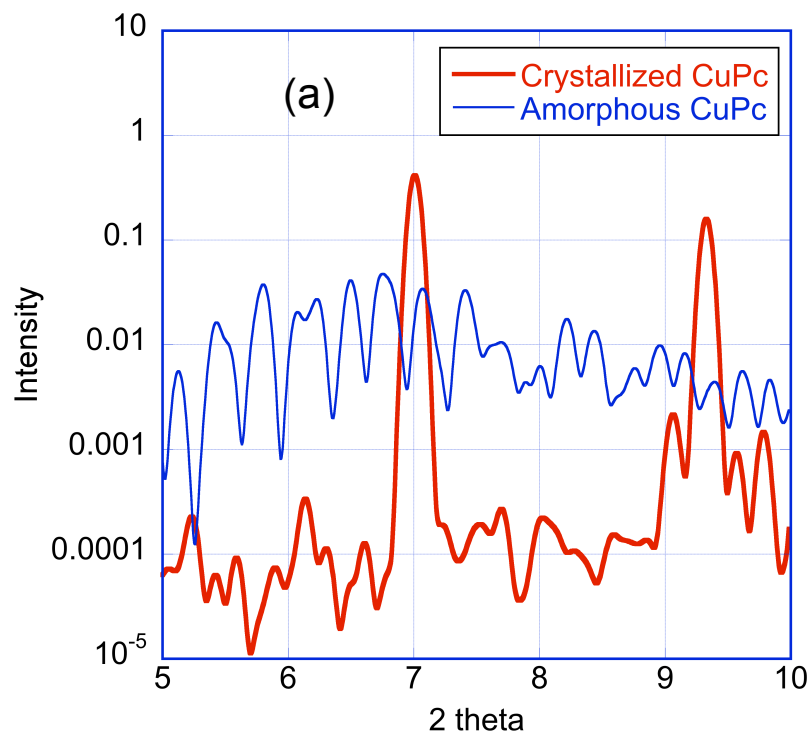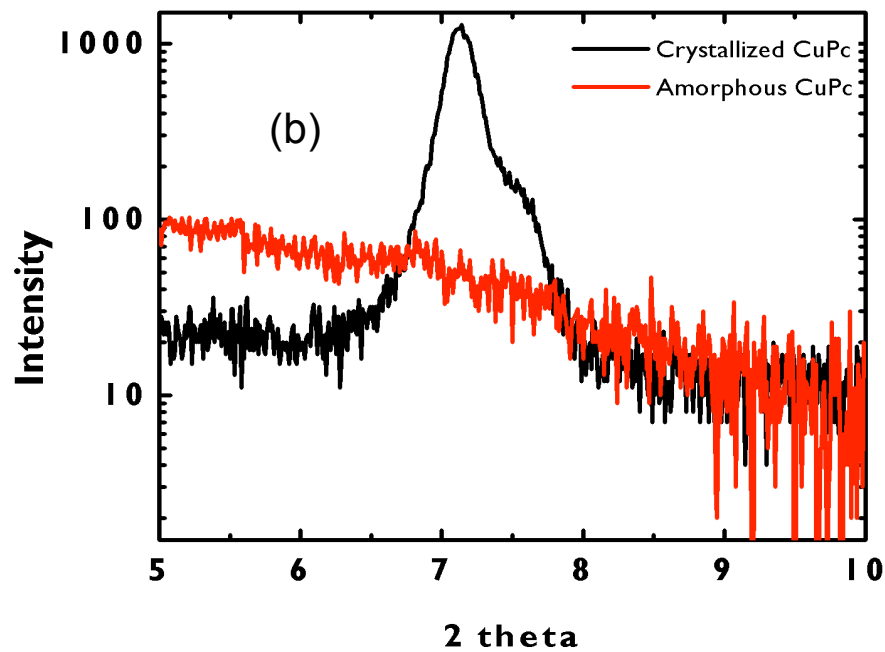
Figure 2.5 XRD patterns for crystalline and amorphous CuPc: (a) calculated based on a

structure relaxed in MD simulations, and (b) experimental data. Experiments completed

by Y. Jin

In experiments, the broadening of the peak at 7° indicates the measured sample displays chain ordering in one or two crystalline directions, but has not developed well-formed three-dimensional crystallites. Using FWHM of the 7° peak and Scherrer equation, we estimate the mean size of the crystalline domains to be around 312 Å. This is in agreement with estimated domain size of 20-50 nm from TEM image in Fig. 2.6.
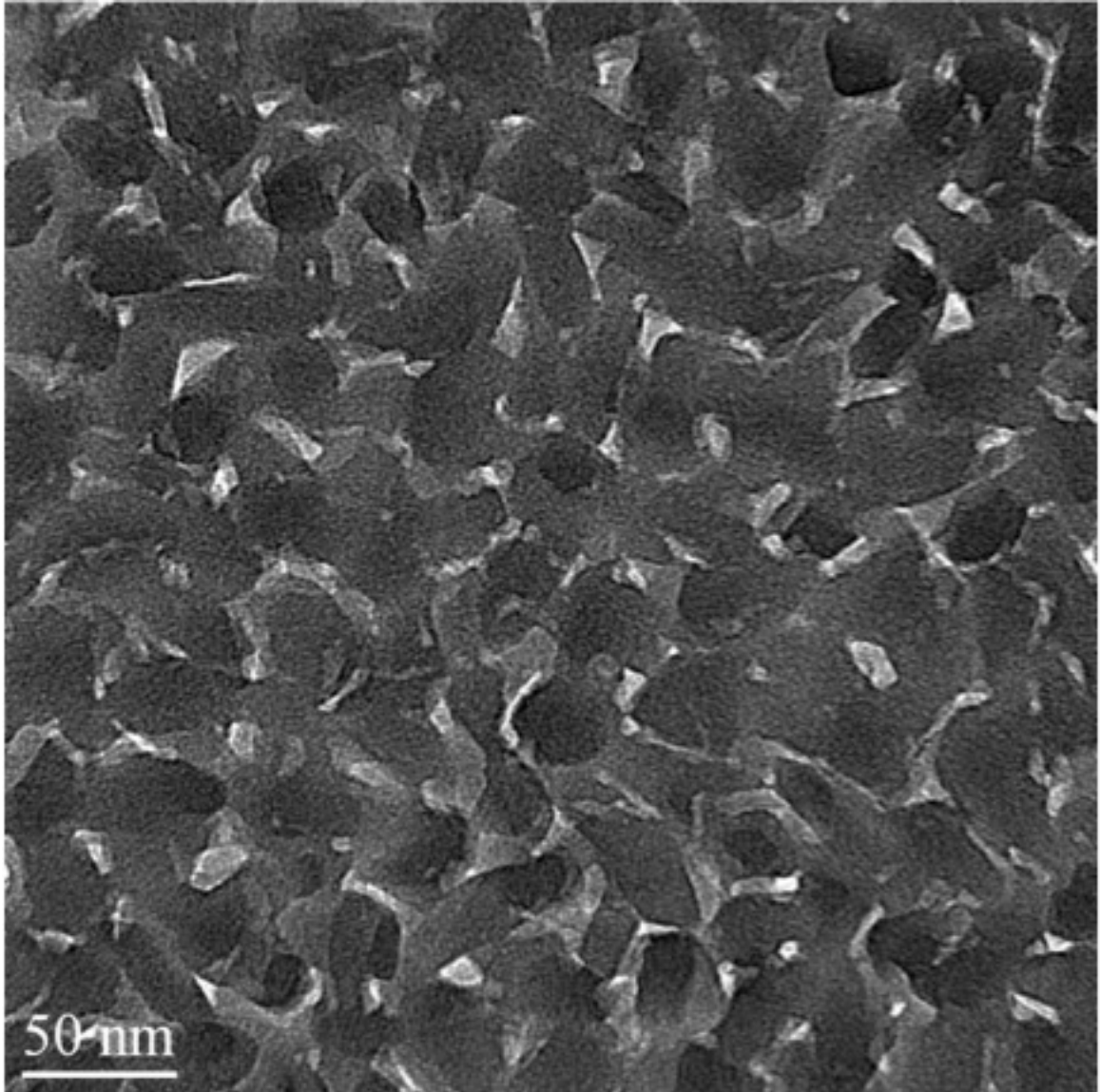
Figure 2.6 Transmission Electron Microscropy (TEM) image of β-CuPc sample. Domain

size is estimated to be 20-50 nm. TEM image of CuPc was taken on a JEOL 2010F

Analytical Electron Microscope at 200 kV. 50 nm of CuPc was vacuum thermal

evaporated onto thin holey carbon film coated Copper grid (Cu-400HN) from Pacific

Grid-Tech, then imaged by TEM to show the domain size. Image taken by Y. Jin

Given that the unit cell coordinates of our simulated structure remain within close agreement to those reported from experimental characterization, we conclude that the 9° peak we see in simulations but is absent in our experimental XRD, is too weak to be detected as a result of the small crystallite size. The relaxed structures are used in MD simulation to calculate thermal conductivities of CuPc in the NVE ensemble. A typical HCACF is plotted vs. time in Fig. 2.7(a) and (b). The rapid oscillations are due to optical phonons in CuPc.

(a)

(b)
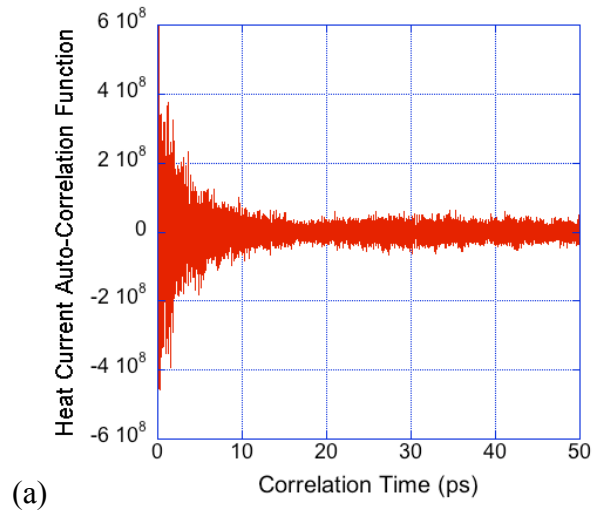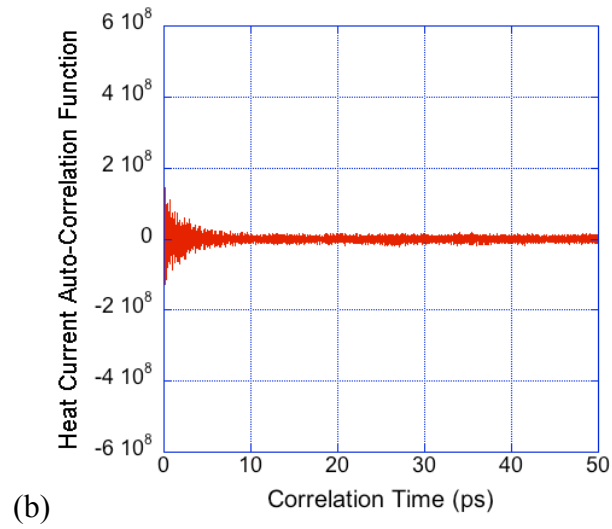
Figure 2.7 Heat current autocorrelation functions for (a) crystalline CuPc, (b) amorphous

CuPc, shown up to 50 ps, beyond which the noise levels remain constant.
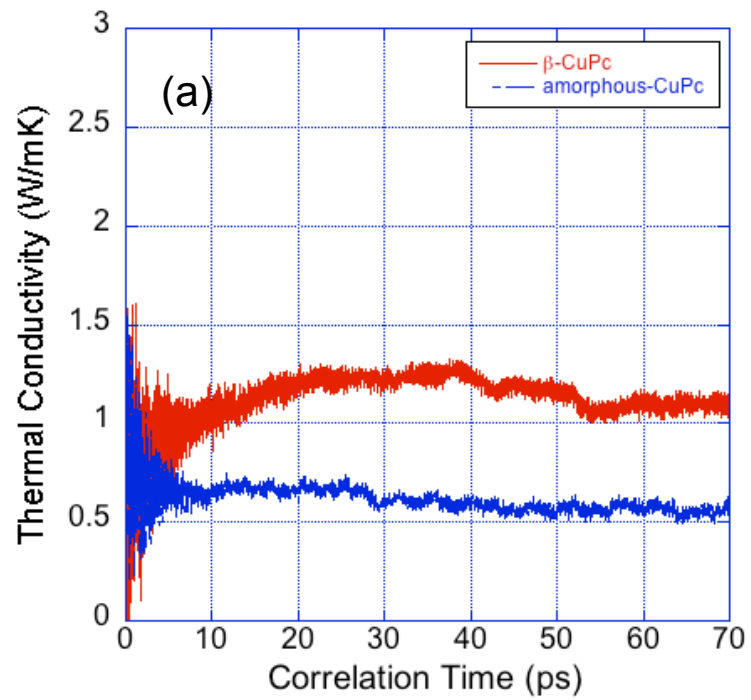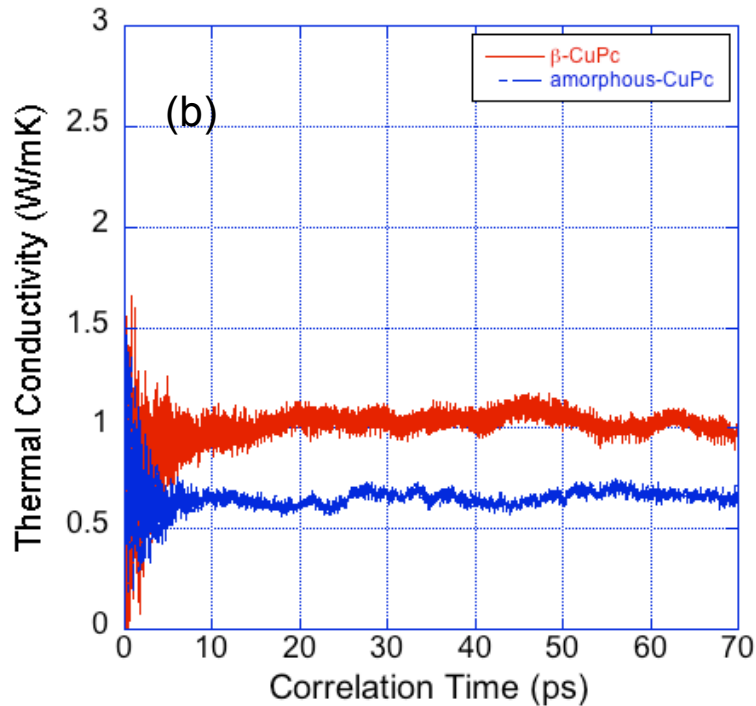
Figure 2.8 Thermal conductivity of crystalline and amorphous CuPc for (a) small and (b) large systems.

We also studied the impact of size effect and cutoff distance of force field on the calculation of thermal conductivity. The sets of both crystalline and amorphous structures are simulated for this study: small systems contain 250 CuPc molecules and large systems contain 2000 CuPc molecules. Cutoff distance of 10 and 15 Å are applied to the two sets of structures respectively.

The running integrals of the HCACF of the two sets of crystalline and amorphous CuPc are plotted in Fig. 2.8. In order to have good statistics on the HCACF, long simulation time is needed so that the average value of HCACF becomes stable. In our simulations, the run time for the Green-Kubo calculation is set to be 1 ns simulation time and the correlation time is 70 ps. These settings will give us enough run time averages of

the auto-correlation function calculated. We found that using cutoff distance of 15 Å would result better consistency for both small and large systems investigated. It is therefore that we choose to use 15 Å as our cutoff distance in our thermal conductivity calculations so that the size of the system will not have much impact on calculation results. The thermal conductivity reaches a value of ~1.1 W/m-K for crystalline and 0.65 W/m-K for amorphous CuPc. Note that the thermal conductivity coefficient, evaluated according to eq. (2.11) is the limit of the Fourier transform of the HCACF at zero frequency. Hence, analyzing the complete Fourier spectrum of the HCACF can provide additional insights into the thermal conduction mechanisms. Fundamentally, the functional form of a HCACF can be expressed as a linear combination of damped harmonic oscillators terms, each representing a particular phonon mode in the structure. Such a model was first proposed by McGaughey and Kaviany,[21, 22] who differentiated between short range acoustic, long range acoustic and optical phonons. Adopting this formalism, the attenuation and oscillatory features of the HCACF are satisfactorily described by

$$\langle \mathbf{J}(t) \cdot \mathbf{J}(0) \rangle = \sum_k A_{r,k} e^{-t/\tau_{r,k}} + \sum_i B_{o,i} e^{-t/\tau_{o,i}} \cos(\omega_{o,i} t), \qquad (2.13)$$

and an exact fit to the HCACF determined in simulations can be achieved by using the appropriate number of terms in the summation, and by choosing the various decay time constants, t_m, oscillatory frequencies, w_m, and mode intensities, A_m and B_m, correctly. The subscripts $m = r$ and o refer to purely relaxational and oscillatory modes, respectively, where the purely relaxational modes could formally also be viewed as zero-frequency modes. In practice, determining these parameters is aided by taking the numerical

49

Fourier transform of the HCACF derived from simulations, which yields spectra such as shown in Fig. 2.9.
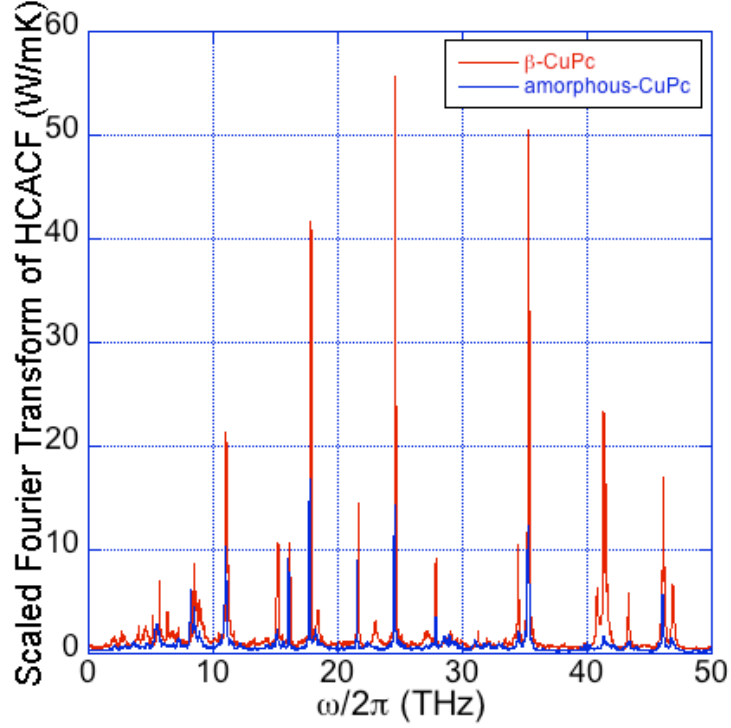
Figure 2.9 Heat current autocorrelation spectrum for β-crystalline and amorphous CuPc.

The spectral peak heights, their positions on the frequency scale, and their full widths at half maximum (FWHM), provide relatively easy access to the quantities A_m, B_m, w_m, and t_m (= FWHM/p). To this end, consider the analytical Fourier transform of expression (2.13),

$$g(\omega) = \mathrm{Re}\left[\int_0^\infty \langle \mathbf{J}(t){\cdot}\mathbf{J}(0)\rangle e^{-j\omega t}\, dt\right] = \sum_k A_{r,k} \frac{\tau_{r,k}}{1+\omega^2\tau_{r,k}^2} + \sum_i B_{o,i}\,\mathrm{Re}\left[\frac{\tau_{o,i}\left(1+j\omega\tau_{o,i}\right)}{\left(1+j\omega\tau_{o,i}\right)^2 + \omega_{o,i}^2\tau_{o,i}^2}\right], \quad (2.14)$$

which yields the expression for the line shape to be fit to the spectra resulting simulations (Fig. 2.8). Once the values for A_m, B_m, w_m, and t_m. are known, we can evaluate $g(\omega)$ consider the zero-frequency limit to recover the definition of the thermal conductivity according to the Green-Kubo formalism of eq. (2.11),

$$k = \frac{1}{k_B V T^2} \left(\sum_k A_{r,k} \tau_{r,k} + \sum_i B_{o,i} \frac{\tau_{o,i}}{1 + \omega_{o,i}^2 \tau_{o,i}^2} \right) = k_r + k_o . \qquad (2.15)$$

where k_r represents all aperiodic contributions to heat propagation and k_o all processes that rely on acoustic or optical phonons for the transport of energy. When calculating the spectra for both crystalline and amorphous CuPc shown in Fig. 2.9, we apply a Savitzky-Golay smoothing filter and assume time reversal symmetry for the HCACF, which yields only real components for the spectra. We then fit the peaks in the spectrum using Lorentzian function to determine time constants τ_m, peak positions $w_{m,,}$ and peak intensities B_m.

Note that eq. (2.15) corresponds to eq. (2.14) evaluated at $w = 0$, and scaled by $1/(k_B V T)$. Accordingly, every vibrational mode in the heat current spectrum contributes to the overall thermal conductivity to an extent that depends on the corresponding peak position, $w_{o,i}$. The amount each mode contributes decreases approximately as $1/\omega_{o,i}^2$, as is illustrated in the inset in Fig. 2.10 (a). This schematic shows two spectral peaks that exhibit a Lorentzian line shape, as expected based on eq. (2.14), located in close enough proximity to the abscissa origin that the wings of these peaks intersect with the ordinate at a finite magnitude. The value of this intersection represents the contribution to the

thermal conductivity. Evidently, the higher the mode frequency, the lower the contribution to the thermal conductivity.

Figs. 2.10 (a) and (b) show the peak fitting results in the 0-10 THz frequency range, which includes acoustic phonon and low-lying optical phonon modes. The calculated time constants and their corresponding peak frequencies are listed in Table 9. The small time constants make for narrow peaks, i.e., they decay rapidly from the peak centers and contribute little to the intercept with the ordinate at $\omega = 0$. We calculated that all oscillatory modes contribute about 15% in crystalline and 11% in amorphous CuPc to the total thermal conductivity, which accounts for a small fraction of the difference between the thermal conductivities in crystalline and amorphous CuPc. The amorphous structure has fever and less intense oscillatory heat current modes. However, the majority of the difference comes from purely relaxational contributions to the conductivity, k_r. From Figs. 2.10(a) and (b), it is clear that the zero-frequency spectral intensity for crystalline CuPc is much stronger than for amorphous CuPc. According to the model expressed by eqs. (2.14) and (2.15), zero-frequency modes correspond to a continuously dissipative propagation of energy, i.e., there no momentary reversal of heat flow. It accounts for the amount of energy passed to adjacent molecular groups during each oscillatory period. Evidently, this mechanism is facilitated by the regularity of a defect-free periodic structure. In β-CuPc the time constant associated with this process is 7.60 ps, one of the slowest mode decays observed in our simulations. This suggests that the majority of the diffuse heat flux is carried by acoustic phonons between about 65 GHz and the Brillouin zone limit. Conversely, the randomness in the amorphous structure strongly suppresses this diffuse heat conduction.
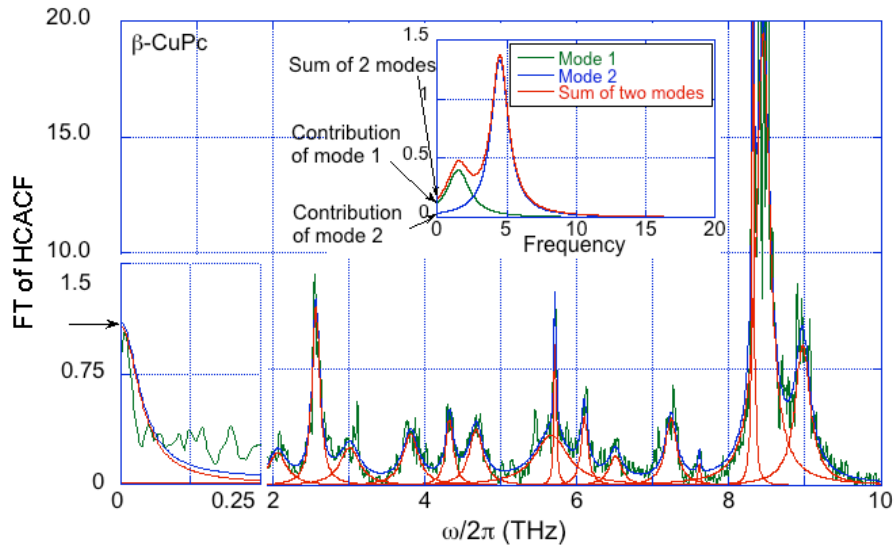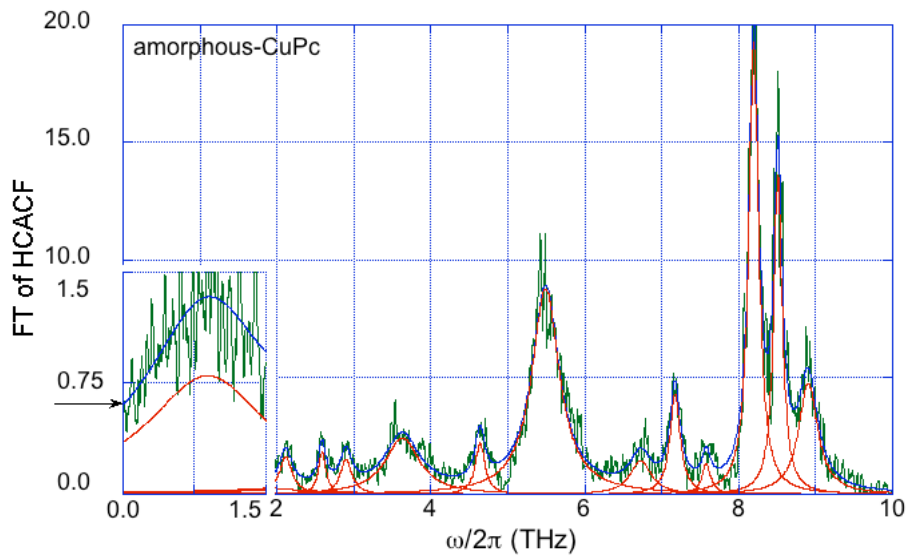
Figure 2.10 Mode analysis of the heat current auto-correlation spectrum for (a) β–crystalline and (b) amorphous CuPc using Lorentzian functional fits. Inset in (a): illustration of how individual modes contribute to the thermal conductivity (intercepts at zero frequency). The low-frequency region of both spectra is magnified along the frequency and intensity axes to better reveal these intercepts.

Thermal conductivities of both crystalline and amorphous CuPc were measured experimentally by Jin[23] and are listed along with the values derived from our simulations in Table 2.8. While the calculated thermal conductivity for the amorphous phase is somewhat larger than the experimentally measured value, that for crystalline CuPc is significantly higher in simulations than in experiment. These discrepancies can be attributed to the differences in sample preparation between experiments and simulations, inaccuracies in the interaction model, or a combination of both. The time allowed for structural relaxation in amorphous materials is much shorter in simulations than in experiments. To compensate for this lack of relaxation, amorphous structures in simulations are prepared at elevated temperatures, compared to cryogenic temperatures in experiments. Conversely, in simulations we construct perfect crystals straightforwardly, while materials obtained under experimental growth conditions consist of nano-crystalline domains with highly disordered domain boundaries. In fact, the experimental sample we have available for comparison consists of nano-crystalline domains with an average size of roughly 30 nm, separated by strongly disordered regions that cause strong phonon scattering. It is known that in polycrystalline Si the thermal conductivity can be reduced by orders of magnitude upon reduction of the grain size.[24] Given that in CuPc crystal, the phonon mean free path is about 14 nm, i.e., well within the estimated domain size, we can express the overall thermal conductivity using Matthiessen's rule as

$$\frac{1}{k_{total}} = \frac{\chi_X}{k_X} + \frac{\chi_A}{k_A} \qquad (2.16)$$

where the subscripts X and A refer to well developed crystalline domains and amorphous regions in between, respectively. The factors χ_i reflect the relative weight of the

conduction mechanisms, which essentially differ in their mean free paths. Accordingly, the experimentally determined thermal conductivity could be explained by attributing to about 55% of heat flow through amorphous and 45% through crystalline regions. This estimate is based the ratio between thermal conductivities in perfect crystalline and amorphous structures derived from simulations. In a one-dimensional geometry, this ratio would correspond to the volume fractions of crystalline domains and amorphous domain boundaries. However, assuming that all crystalline domains are encased in amorphous regions and thus separated from each other, thermal diffusion is naturally three-dimensional in such complex structures, and simple models easily overestimate the effect of amorphous phase.

2.6 Conclusion

The Hybrid-COMPASS force field has been expanded to accurately simulate CuPc isolated molecules, as well as crystalline and amorphous condensed phases. The structure of the isolated CuPc molecule is in good agreement with experimental observations. The MD simulations also predict α- and β-form CuPc crystal structures at different temperatures with reasonable accuracy when compared with experimental measurements. The vibrational density of states calculated from MD simulation also agrees well with both experimental and theoretical studies of normal mode frequencies of CuPc molecule. Based on this new force field, we analyzed the thermal conduction mechanisms in amorphous and crystalline CuPc using the Green-Kubo formalism. Comparing with experimental measurements we observe reasonable agreement for amorphous samples, and we conclude that the crystalline samples consist of nano-

domains isolated from each other by significant amounts of amorphous domain boundaries, possibly exceeding half the sample volume.

2.7 References

1 F.H. Moser and A.L. Thomas, '*The phthalocyanines*,' (CRC Press, Boca Raton, Fla., 1983).

2 A. Vartanyan, 'Poluprovodnikovye Svoistva Organicheskikh Krasitelei.1. Ftalotsianiny,' *Zh Fiz Khim+* **22**, 769 (1948).

3 G.G. Fedoruk, D.I. Sagaidak, A.V. Misevich, and A.E. Pochtenny, 'Electrical and gas sensing properties of copper phthalocyanine polymer composites,' *Sensor Actuat B-chem* **48**, 351 (1998).

4 T. Reinot, W.H. Kim, J.M. Hayes, and G.J. Small, 'New standard for high-temperature persistent-hole-burning molecular materials: Aluminum phthalocyanine tetrasulphonate in buffered hyperquenched glassy films of water,' *J Opt Soc Am B* **14**, 602 (1997).

5 H. Hoppe and N.S. Sariciftci, 'Organic solar cells: An overview,' *J. Mater. Res.* **19**, 1924 (2004).

6 S.X. Yin, C. Wang, B. Xu, and C.L. Bai, 'Studies of CuPc adsorption on graphite surface and alkane adlayer,' *J. Phys. Chem. B* **106**, 9044 (2002).

7 S.A. Chen and J. Ma, 'The influence of orientations and external electric field on charge carrier mobilities in CuPc and F16CuPc films on highly ordered pyrolytic graphite and octane-1-thiol terminated Au(111) substrates,' *Phys Chem Chem Phys* **12**, 12177 (2010).

8 S.W. Bunte and H. Sun, 'Molecular modeling of energetic materials: The parameterization and validation of nitrate esters in the COMPASS force field,' *J. Phys. Chem. B* **104**, 2477 (2000).

9 H. Sun, 'COMPASS: An ab initio force-field optimized for condensed-phase applications - Overview with details on alkane and benzene compounds,' *J. Phys. Chem. B* **102**, 7338 (1998).

10 H. Sun, P. Ren, and J.R. Fried, 'The COMPASS force field: parameterization and validation for phosphazenes,' *Comput Theor Polym S* **8**, 229 (1998).

11 N.L. Allinger, K.S. Chen, and J.H. Lii, 'An improved force field (MM4) for saturated hydrocarbons,' *J. Comput. Chem.* **17**, 642 (1996).

12 M.J. Hwang, T.P. Stockfisch, and A.T. Hagler, 'Derivation and Characterization of a Class-II Force-field, CFF93, for the Alkyl Functional-Group and Alkane Molecules,' *J. Am. Chem. Soc.* **116**, 2515 (1994).

13 T.A. Halgren, 'Merck molecular force field.1. Basis, form, scope, parameterization, and performance of MMFF94,' *J. Comput. Chem.* **17**, 490 (1996).

14 T.C. Ionescu, F. Qi, C. McCabe, A. Striolo, J. Kieffer, and P.T. Cummings, 'Evaluation of force fields for molecular simulation of polyhedral oligomeric silsesquioxanes,' *J. Phys. Chem. B* **110**, 2502 (2006).

15 J.R. Maple, U. Dinur, and A.T. Hagler, 'Derivation of Force-fields for Molecular Mechanics and Dynamics From Abinitio Energy Surfaces,' *P Natl Acad Sci Usa* **85**, 5350 (1988).

16 D.C. Xia, W.C. Li, X. Wang, S.K. Yu, C.X. Fan, C.Y. Ma, C.H. Cheng, Z.Q. Fan, G.T. Du, F.D. Cong, and X.G. Du, 'Preparation of copper phthalocyanine, crystals using solvothermal synthesis,' *Chem Res Chinese U* **24**, 407 (2008).

17 C.J. Brown, 'Crystal Structure of Beta-copper Phthalocyanine,' *J Chem Soc A* 2488 (1968).

18 D.C. Li, Z.H. Peng, L.Z. Deng, W.F. Shen, and Y.H. Zhou, 'Theoretical studies on molecular structure and vibrational spectra of copper phthalocyanine,' *Vib Spectrosc* **39**, 191 (2005).

19 R. Aroca, Z.Q. Zeng, and J. Mink, 'Vibrational Assignment of Totally Symmetric Modes in Phthalocyanine Molecules,' *J. Phys. Chem. Solids* **51**, 135 (1990).

20 R. Kubo, M. Yokota, and S. Nakajima, 'Statistical-mechanical Theory of Irreversible Processes 2. Response to Thermal Disturbance,' *J. Phys. Soc. Jpn.* **12**, 1203 (1957).

21 A.J.H. McGaughey and M. Kaviany, 'Thermal conductivity decomposition and analysis using molecular dynamics simulations. Part I. Lennard-Jones argon,' *Int. J. Heat Mass Transfer* **47**, 1783 (2004).

22 A.J.H. McGaughey and M. Kaviany, 'Thermal conductivity decomposition and analysis using molecular dynamics simulations: Part II. Complex silica structures,' *Int. J. Heat Mass Transfer* **47**, 1799 (2004).

23 Y. Jin, A. Yadav, K. Sun, H. Sun, K.P. Pipe, and M. Shtein, 'Thermal boundary resistance of copper phthalocyanine-metal interface,' *Appl. Phys. Lett.* **98**, ARTN 093305 (2011).

24 Z. Wang, J.E. Alaniz, W. Jang, J.E. Garay, and C. Dames, 'Thermal conductivity of nanocrystalline silicon: Importance of grain size and frequency-dependent mean free paths,' *Nano letters* **11**, 2206 (2011).

25 H. Heinz, R.A. Vaia, B.L. Farmer, and R.R. Naik, 'Accurate Simulation of Surfaces and Interfaces of Face-Centered Cubic Metals Using 12-6 and 9-6 Lennard-Jones Potentials,' *J. Phys. Chem. C* **112**, 17281 (2008).

26 A.A.M. Farag, 'Optical absorption studies of copper phthalocyanine thin films,' *Opt Laser Technol* **39**, 728 (2007).

27 M. Ashida, N. Uyeda, and E. Suito, 'Unit Cell Metastable-form Constants of Various Phthalocyanines,' *B Chem Soc Jpn* **39**, 2616 (1966).

Table 2-1 Hybrid-COMPSS force field parameters for CuPc

Quartic Bond

i	j	b_0 (Å)	k_2 (kCal/mol·Å^{-2})	k_3 (kCal/mol·Å^{-3})	k_4 (kCal/mol·Å^{-4})
C	N	1.3750	325.3433	-204.4082	466.3989
C	C[a]	1.4170	470.8361	-627.6179	1327.6345
C	H[a]	1.0982	372.8251	-803.4526	894.3173
Cu	N	1.9540	245.0000	-88.9193	-55.4174

Quartic Angle

i	j	k	θ_0 (°)	H_2 (kCal/mol·deg^{-2})	H_3 (kCal/mol·deg^{-3})	H_4 (kCal/mol·deg^{-4})
C	C	N	122.8550	74.2474	-50.0000	0.0000
N	C	N	127.6575	90.5230	-20.8010	-18.0000
C	C	C[a]	118.9000	61.0226	-34.9931	0.0000
C	N	C	115.5720	48.2320	-5.7980	-9.9660
C	C	H[a]	117.9400	35.1558	-12.4682	0.0000
C	N	Cu	125.8850	49.8203	-13.4750	5.8570
N	Cu	N	90.0000	59.5741	-35.2545	16.0517

Torsion

i	j	k	l	V_1 (kCal/mol)	V_2 (kCal/mol)	V_3 (kCal/mol)
N	C	C	C	3.1952	11.2745	-1.4456
C	C	N	C	0.0000	1.0000	0.0000
N	C	N	C	0.0000	1.0000	0.0000
C	C	N	Cu	1.8405	5.4779	3.1407
N	C	N	Cu	-3.9545	4.8864	10.0000
C	C	C	C[a]	8.3667	1.2000	0.0000
C	C	C	H[a]	0.0000	3.9661	0.0000
H	C	C	H[a]	0.0000	2.3500	0.0000
C	N	Cu	N	-6.9564	17.7309	-5.0508

Nonbond (LJ9-6)

i	ε_0 (kCal/mol)	r_0 (Å)	i	ε_0 (kCal/mol)	r_0 (Å)
C[a]	0.068	3.915	N	0.120	3.400
H[a]	0.023	2.878	Cu[b]	3.840	2.661

Bond Increments

i	j	Bond Increments (e⁻)
Cu	N	0.2191
C	C^9	0.0000
C	H^{25}	-0.1268
C	N	0.2448

Table 2-2 Bond lengths of the CuPc molecule

Bond lengths (Å)	Experiment [17]	B3LYP/6-311G(d,p)	Hybrid COMPASS	Percentage Deviation
C1-C9	1.453	1.457	1.411	-2.9%
C1-N33	1.328	1.325	1.367	2.9%
C1-N37	1.366	1.375	1.377	0.8%
C9-C13	1.400	1.406	1.396	-0.3%
C9-C20	1.391	1.396	1.410	1.4%
C19-C20	1.391	1.394	1.422	2.2%
C18-C19	1.413	1.409	1.427	1.0%
C20-H44		1.087	1.098	1.0%
N37-Cu57	1.940	1.954	1.958	0.9%

Table 2-3 Bond angles of CuPc molecule

Bond angles (°)	Experiment [17]	B3LYP/6-311G(d,p)	Hybrid COMPASS	Percentage Deviation
Cu57-N37-C1	126.350	125.891	126.148	-0.2%
C1-N37-C5	107.300	108.228	107.703	0.4%
N33-C1-N37	127.550	127.651	129.768	1.7%
N33-C1-C9	122.700	122.855	121.153	1.3%
N37-C1-C9	109.750	109.490	109.079	-0.6%
C1-C9-C13	106.600	106.399	107.069	0.4%
C20-C9-C13	121.050	121.210	121.820	0.6%
C9-C20-C19	117.950	117.606	117.390	-0.5%
C20-C19-C18	120.975	121.190	120.790	-0.2%
C19-C20-H44		120.702	120.239	-0.4%

Table 2-4 Vibrational Frequencies of the CuPc Molecule

no.	Symmetry	Experiment (cm⁻¹)[18, 19, 26]	B3LYP/6-311G(d,p) (cm⁻¹)[18]	Hybrid COMPASS (cm⁻¹)	Difference (cm⁻¹)
1	$12A_{1g}$	1590	1580.1	1595	5
2	$11A_{1g}$	1528	1511.1	1562	34
3	$9A_{1g}$	1431	1421	1449	18
4	$8A_{1g}$	1341	1335.7	1367	26
5	$6A_{1g}$	1140	1115.8	1107	-33
6	$5A_{1g}$	1037	998.7	1042	5
7	$4A_{1g}$	831	825.4	813.8	-17.2
8	$3A_{1g}$	678	668.7	732.4	54.4
9	$2A_{1g}$	588	580.6	602.2	14.2
10	$1A_{1g}$	236	250.5	244.1	8.1

Table 2-5 Unit cell parameters for α-CuPc

	Experiment[19]	Hybrid COMPASS
a (Å)	25.92	26.22
b (Å)	3.79	4.03
c (Å)	23.92	23.39
α (°)	90	88.15
β (°)	90.4	89.50
γ (°)	90	90.09

Table 2-6 Unit cell parameters for β-CuPc

	Experiment[17]	Hybrid COMPASS
a (Å)	19.407	19.46
b (Å)	4.79	4.98
c (Å)	14.628	14.51
α (°)	90	90.01
β (°)	120.56	121.83
γ (°)	90	89.99

Table 2-7 Densities of CuPc crystals

	α-form	β-form
Molecule/unit cell	4	2
Unit cell volume ($Å^3$)	2451.55	1201.70
Density (g/cm^3) (calc.)	1.56	1.59
Density (g/cm^3) (found) [17,27]	1.62	1.63

Table 2-8 Thermal conductivities from MD simualtions and experiments

Thermal conductivity	MD (W/mK)	Experiment (W/mK)
amorphous CuPc	0.65 ± 0.2	0.32
crystalline CuPc	1.1 ± 0.2	0.39

Table 2-9 Peak location and time constants in HCACF spectrum

β-CuPc		amorphous CuPc	
Peak Location (THz)	τ (ps)	Peak Location (THz)	τ (ps)
0	7.60	2.08	2.17
2.06	1.84	2.84	0.99
2.57	5.72	3.64	1.08
2.88	3.32	4.69	4.52
3.99	2.76	7.22	2.21
4.60	2.20	8.20	5.41
5.13	11.5	8.47	3.91
5.69	11.9	8.90	2.17
6.31	6.24		
6.71	1.40		

Chapter 3 Molecular Dynamics Study of Interface Bonding and Thermal Boundary Conductance at Copper Phthalocyanine Metal Interfaces

Synopsis

We use classical molecular dynamics (MD) simulations to carry out a systematic study of the nanoscale processes that govern the thermal boundary conductance at copper phthalocyanine (CuPc)/metal interfaces. Non-equilibrium MD simulations (NEMD) are performed on metal–CuPc–metal junctions to study thermal energy transport across the interfaces through the Müller-Plathe method. By varying the density and modulus of the structurally congruent system, interfaces with matched acoustic impedance, speed of sound are constructed. Heat transfer simulation results show that the traditional acoustic mismatch model (AMM) does not predict correct results. The interfacial bonding strength is controlled directly in the MD simulation by scaling the interaction parameters for the materials juxtaposed at the interface. The thermal boundary conductance is closely related to the interfacial bonding strength. By comparing the MD calculation results with the experimental measurements, the work of adhesion between CuPc and metal substrates is estimated to be 0.046 ± 0.014 J/m^2 for CuPc/Ag, 0.095 ± 0.004 J/m^2 for CuPc/Ag, and 0.439 ± 0.1 J/m^2 for CuPc/Al interfaces. These findings confirm the experimental

observation of very weak bonding between CuPc and Au or Ag and strong bonding at the CuPc/Al interface. Phonon spectral analysis shows that the majority of heat transfer between CuPc and Au is accomplished via anharmonic coupling, which appears to be facilitated by strongly adhesive interfacial bonding.

3.1 Introduction

With their unique properties and wide range of applications, molecular organic semiconductors have attracted increasing attention. Strong optical absorption, ultra-efficient light emission, room-temperature operation, and long-lived excitons are just a few of the attractive properties that molecular organic semiconductors can offer. Furthermore van der Waals bonding among molecules in the condensed phase enables the non-epitaxial deposition of device-quality thin films on large area substrates, potentially facilitating the scale-up of the next generation of large-area lighting, photovoltaic, and electronic devices. Organic-inorganic interfaces are ubiquitous in these applications and closely related to many crucial thermally activated processes such as charge transport and exciton dissociation or recombination.[1-5] However, the thermal transport properties of such organic-inorganic interfaces remain poorly understood. Studying the mechanisms for phonon transport across such interfaces can help us better understand and control the energy transport in devices. In this work, we use molecular dynamics simulations to investigate the effect of interfacial bonding strength on the thermal transport across interfaces between organic and inorganic materials.

When energy is transported across the interface of dissimilar materials, there is a resistance to the heat flow at the interface that leads to a temperature discontinuity ΔT at

the interface.[6,7] Such resistance is referred to as Kapitza resistance or thermal boundary resistance (TBR). The thermal boundary conductance (TBC) is defined as the inverse of TBR: $G = 1/R = q/\Delta T$, where q is the heat flux (W/m^2) across the interface.[8] The primary thermal energy carriers in semiconductors and dielectric materials are acoustic phonons. Consequently, the TBC of dissimilar dielectric materials is often reduced due to phonon scattering caused by the discontinuity in mechanical properties at the interface. There have been two primary theoretical models developed to estimate TBC of interfaces: the acoustic mismatch model (AMM) and the diffuse mismatch model.(DMM)[8] However, both models assume very strong bonding at the interface, typically in excess of the relatively weak van der Waals interactions that prevail at organic-inorganic interfaces. Moreover, anharmonic processes are not considered in either model, and both fail to accurately predict the TBC values for many systems. In particular, in experiments the TBC of metal-organic interfaces[9-11] are measured to be an order of magnitude lower than that of the majority of metal-inorganic dielectric interfaces,[12] while the models predict a smaller difference.[13]

Lattice-dynamics calculations have been utilized to numerically determine TBC by considering purely harmonic oscillations and elastic scattering only.[14-17] Molecular dynamics (MD) simulations are a better method to understand and investigate realistic transport between dissimilar materials because it accounts for anharmonic processes in simulations and it allows for systematic control over the interfacial structure and definition, which is difficult to do experimentally. Prior work has been done to investigate the thermal transport in many systems numerically. Lattice dynamics calculations by Stoner et al.[18] and Young et al.[17] showed that the phonon transmission

70

coefficient is strongly affected by the spring constant linking the two materials. Using MD simulations, Stevens[19] showed a linear dependence of TBC on temperature, and that interface mixing would improve the thermal transport across solid-solid interfaces. Torii[20] determined that weakening the interaction between solid and liquid would decrease the TBC (increase the TBR) at interface. Work by Ong and Pop[21] revealed a nearly linear dependence of the TBC on the strength of the interface interaction for weakly bonded carbon nanotubes and SiO_2. Recently, Shen[22] investigated the effect of hydrostatic pressure on TBC of simple fcc metal system using MD simulations and found that the interfacial stiffness increases linearly with pressure for weakly bonded interface, and consequently TBC first increases proportionally to interfacial stiffness before saturating at high values, while for strongly bonded interface, TBC was almost independent of pressure increase.

Motivated by the fact that interfacial bonding strength appears to play an important role in TBC at interfaces, we use MD simulations to systematically investigate the role that interfacial bonding strength across CuPc-metal interfaces has on its TBC. We compare the predictions of the AMM model to experimental observation, and conduct a parametric study of interfacial bonding strength to identify the dominant TBC mechanism. The remainder of this chapter is organized as follows: MD simulations details are described Section 3.2, simulation results are presented and discussed in Section 3.3 and conclusions are presented in Section 3.4.

3.2 Molecular dynamics simulation details

The materials system we prepared for this study is composed of fcc metal lattice and α-crystalline copper phthalocyanine (CuPc). The CuPc crystal is comprised of $3 \times 25 \times 3$ unit cells. The COMPASS force field is used to describe interactions in CuPc and the 9-6 Lennard Jones (LJ) potential[23] is used for the metal substrates. The interaction between CuPc and metal substrate is modeled using mixing rules for the COMPASS force field. In this paper, all van der Waals interactions are modeled with the 9-6 Lennard Jones (LJ) potential:

$$U_{vdw} = \sum_{i,j} \varepsilon_{ij} \left[2\left(\frac{r_{ij}^0}{r_{ij}}\right)^9 - 3\left(\frac{r_{ij}^0}{r_{ij}}\right)^6 \right] \qquad (3.1)$$

$$r_{ij}^0 = \left(\frac{\left(r_i^0\right)^6 + \left(r_j^0\right)^6}{2}\right)^{1/6} \qquad (3.2)$$

$$\varepsilon_{ij} = 2\sqrt{\varepsilon_i \cdot \varepsilon_j} \left(\frac{\left(r_i^0\right)^3 \cdot \left(r_j^0\right)^3}{\left(r_i^0\right)^6 + \left(r_j^0\right)^6}\right) \qquad (3.3)$$

where ε_{ij} is the depth of the potential well and r_{ij}^0 represents the spacing between atom i and atom j where the potential is minimum. The simplicity of this potential allows us to tune the elastic modulus of the simulated material by simply scaling the parameter ε_{ij}. The metal substrate and crystlline β-CuPc are first equilibrated at room temperature. The CuPc crystal is then sandwiched between two metal slabs and the whole structure is duplicated in the sandwiched dimension, creating one more pair of layers to allow

placement of a heat source in one and a heat sink in other metal slab so generated. The schematic of the system is shown in Figure 3.1.
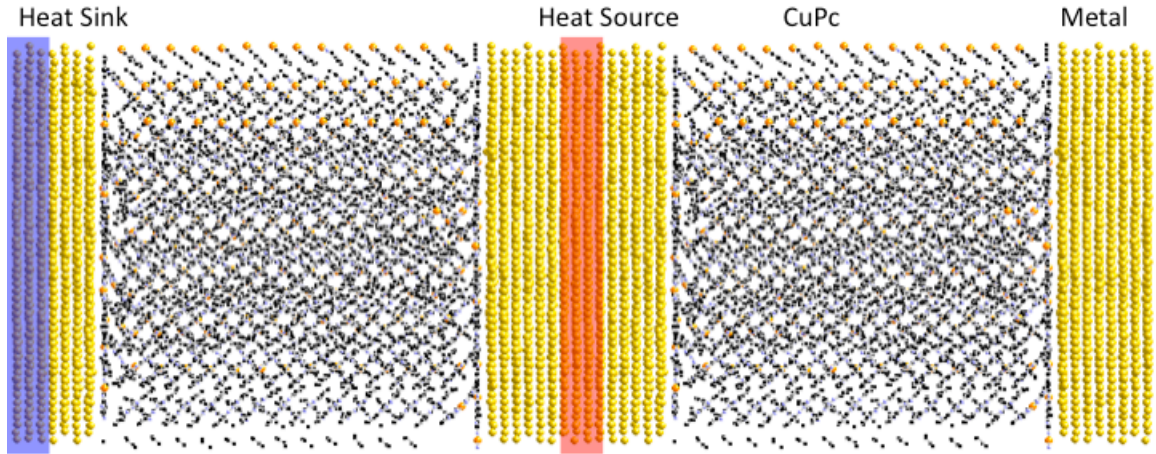
Figure 3.1 Schematic setup for CuPc-metal junction

For this study, we adopt the non-equilibrium molecular dynamics (NEMD) simulation[24] to calculate the TBC at the CuPc-metal interfaces. For direct measurement in MD simulation, the structure is numerically coupled to a heat source and a heat sink as shown in Figure 3.1. When the heat flux across the CuPc-metal interfaces reaches stead-state, the resulting temperature discontinuity at the CuPc-metal interface is gauged to obtain the TBC. Ideally, the temperature change should be sharp and localized at the interface to allow for the unequivocal identification of a quantity ΔT. From our

simulation results, however, it can be seen that the temperature change is gradually accelerated upon approaching the interface plane, especially in the organic region. The following procedures are implemented to calculate ΔT at the interface in a consistent way (shown in Figure 3.2): (i) the temperature profile for the CuPc region of the system is fit by a tangent function; (ii) the minimum derivative of the tangent curve is calculated and a straight line with that same slope is extrapolated from the inflection point to the material interfaces; (iii) for the metallic region, a linear regression is used to describe the temperature profile across the metal slab; (iv) ΔT is then determined as the difference between the two points of intersection with the interfacial plane of the geometric constructs pertaining to each layer. After computing the magnitude of the steady-state heat flux, we can estimate the TBC.
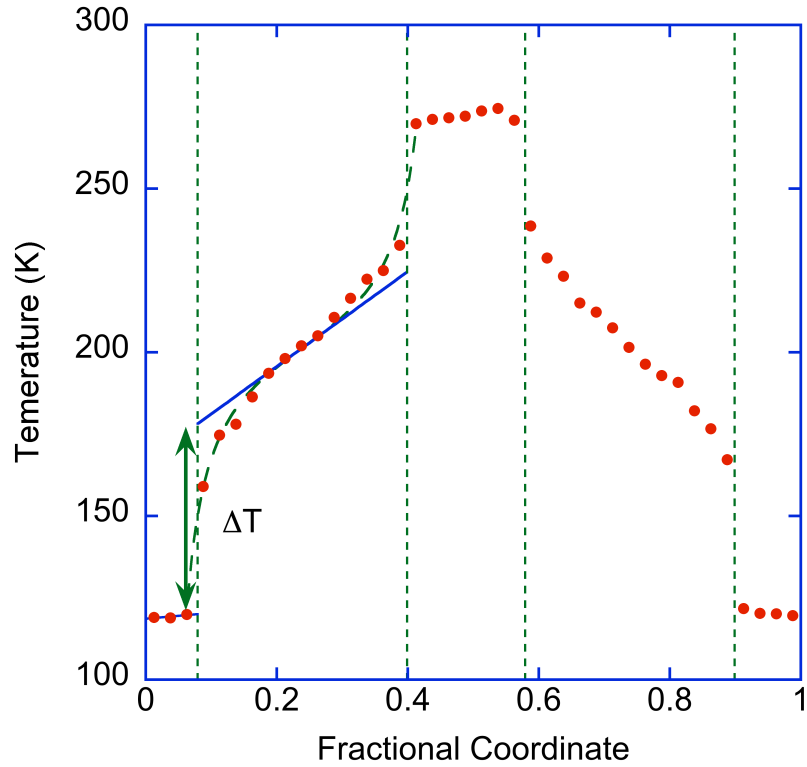
Figure 3.2 Procedures to calculate ΔT at the interface: minimum slope is extrapolated to

the interface to determine ΔT

3.3   Results and discussion

3.3.1   TBC at CuPc-metal interfaces with fixed bonding strength

The traditional theory of acoustic mismatch model (AMM) states that TBC is directly related to the phonon transmission coefficient, τ_b, at the interface, which combines the mechanical impedance of the adjacent materials,

$$\tau_b = \frac{4Z_1Z_2}{\left(Z_1 + Z_2\right)^2} \qquad (3.4)$$

where Z_i. is the mechanical impedance of material i, and is defined as the product of density and the speed of sound. Rewriting equation, the mechanical impedance can be expressed as

$$Z = \rho \cdot u_p = \sqrt{\rho \cdot E} \quad (3.5)$$

where ρ is the density and E is the elastic modulus of the material. In MD simulations, both ρ and E can be controlled straightforwardly. In this study, we controlled the density of the metal substrate by scaling the mass of the atoms in the substrate. Fundamentally, the elastic modulus of a material is proportional to the second derivative of the interaction energy.[25] The second derivative of eq. (3.1) is still proportional to ε, and hence, the elastic modulus is simply adjusted by varying the interaction potential well depth. This causes the potential well curvature and consequently the mechanical stiffness of the metal to change. Accordingly, we start with the potential for FCC Au, and change the substrate to lighter and softer metal. Even though these new atoms with scaled mass may not be realized in the laboratory, in MD simulation they provide a powerful method to uncover the governing principles of materials behavior. In particular, we can tune the material's acoustic impedance. Note that gold and silver have an FCC structure with almost identical unit cell parameters, but they have different atomic mass and the elastic modulus of silver is about half that of gold. Hence, to convert a gold to silver, computationally, one only needs to change the atomic mass and interaction potential well depth, while keeping the lattice parameters unchanged. In Figure 3.3, we therefore show two sets of data of the thermal boundary conductance between an FCC lattices with 4.08 Å unit cell size and CuPc. In both cases we vary the atomic weight between 2 and 197

amu, but one set of data (squares) is calculated using force field parameters that yield the elastic modulus of gold, and the other set (circles) is calculated using a force field with half the potential well depth, i.e., mimicking the elastic response of silver. The solid and dashed lines in Figure 3.3 represent the best fit of the data using the AMM model. In all these simulations, the bonding strength at the interface is kept the same for all systems.
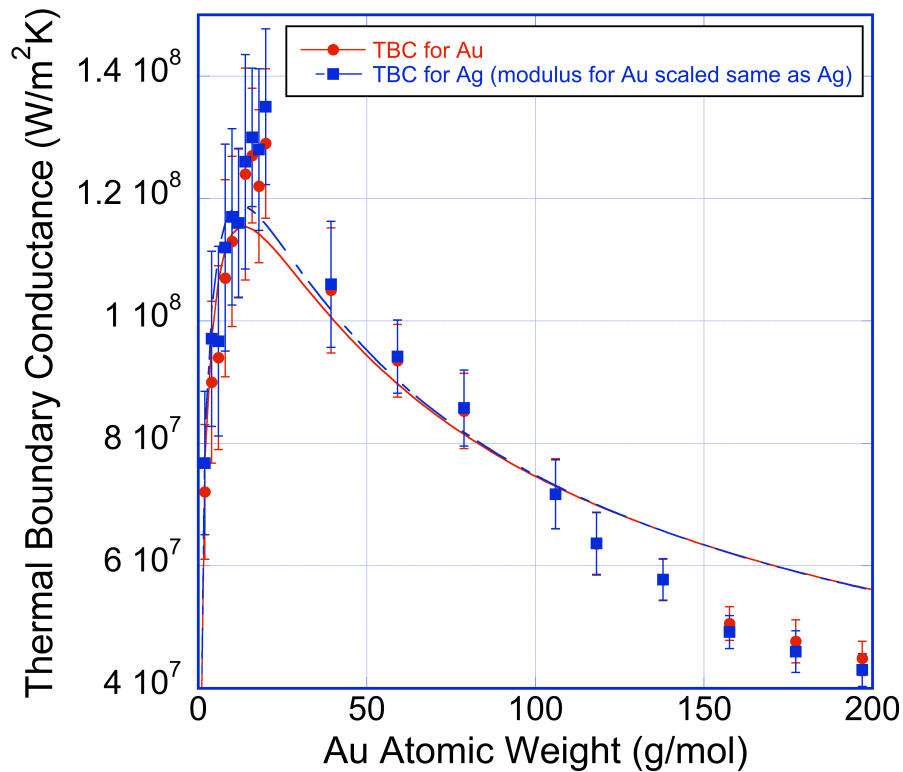
Figure 3.3 TBC for systems with scaled gold atomic mass

From the graph we can see that, if we neutralize the influence of interfacial bonding strength and only consider the effect of impedance mismatch, AMM can explain MD simulation results fairly well. Based on experiments, CuPc is reported to have an elastic modulus of 9.6 GPa while the bulk elastic modulus for Au is 180 GPa. The density of CuPc is 1.6 g/cm^3 and it is 19.3 g/cm^3 for Au. The huge mismatch in both density and

elastic modulus explains why for the Au-CuPc interface the AMM model predicts a low TBC. Figure 3.3 also shows a maximum for TBC where the impedance of substrate matches impedance of CuPc. Further decrease of the substrate density results in an increased impedance mismatch and decreased TBC. In our simulations, we generated a second set of data with a bulk modulus of ~100 GPa, keeping the same interfacial interaction strength and varying the atomic weight over the same range as for the first set. This second set encompasses a system representative of silver for M = 107.8682 g/mol. We then compare TBC at CuPc/Ag(111) and CuPc/Au(111) interfaces, assuming the two interfaces have the same interfacial bonding strength. MD simulation results, as well as the AMM model predict a larger TBC for the CuPc/Ag than for the CuPc/Au interface. In experiments, however, Y. Jin et al.[10] report the opposite, a lower TBC for CuPc/Ag interface than for the CuPc/Au interface (Table 3.1). These authors also report a distinctly higher work of adhesion for the CuPc/Ag interface than for the CuPc/Au interface, based on peel-off tests. This suggests that for weakly bonded systems, the acoustic impedance may not be the key factor that controls TBC, but that perhaps the interfacial bonding strength may play an important role.

3.3.2 TBC at a congruent interface between metals with tunable properties

Note that the AMM model does not take structural mismatch at the interface into consideration. Hence, to further investigate the validity of the AMM model, we eliminate incongruencies at the interface by starting with a defect-free single crystal structure and dividing it into two segments. The atoms in each segment are assigned masses and interaction potential well depths so as to achieve four different materials pairings, based

on their densities and elastic constants. This can be done straightforwardly in MD simulations. In all cases do the paired materials retain identical equilibrium structures and lattice constants, and the interface between the segments is not identifiable based on structural characteristics alone. We constructed and compared the thermal transport properties of four different pairings: (1) the masses and interaction potentials in both compartments are identical, i.e., in effect, the structure consists of only one material and serves as a reference configuration; (2) the masses and interaction well depths are arbitrarily mismatched, i.e., neither the product nor the ratio of the elastic constant and density are matched; (3) while the elastic constants and masses of atoms in either compartment are different, their products are equal, i.e., the acoustic impedances of the two adjacent materials are matched; (4) again masses and elastic constants differ between compartments, but now their ratios are equal, i.e., the velocity of sound is the same in both materials. We use EAM potential for Au in these studies as it is well parameterized to simulate key properties of metals.[26]

We then subjected the structures so generated to the Müller-Plathe non-equilibrium MD simulations to determine the thermal conductance at the structurally invisible interfaces of these systems. The results are summarized in Figure 3.4, which shows the steady state temperature profiles across the materials bi-layers. Sharp discontinuities in the temperature profiles demarcate the interfaces, and the larger drop in temperature at the interface, the smaller the thermal boundary conductance. As expected, when the materials properties are identical, there is no interface and there is no temperature discontinuity. Similarly, when the densities and elastic constants are arbitrarily mismatched, a pronounced discontinuity in temperature at the interfaces is

apparent. Surprisingly, when the acoustic impedances of the adjoining materials are matched the temperature jump at the interface is still clearly identifiable and much larger than when matching the sound velocities. Hence, it seems that, even after clearing the materials system of structural mismatches at the interface, the AMM model does not grasp the essence of thermal transport across interfaces. Instead, focusing on the propagation speeds of elastic deformations, and possibly phonon dispersion behavior or spectral features, may be more opportune. In the next section we address the question of whether coupling between acoustic spectral modes across the interface are important for transferring energy from one phase to the other.
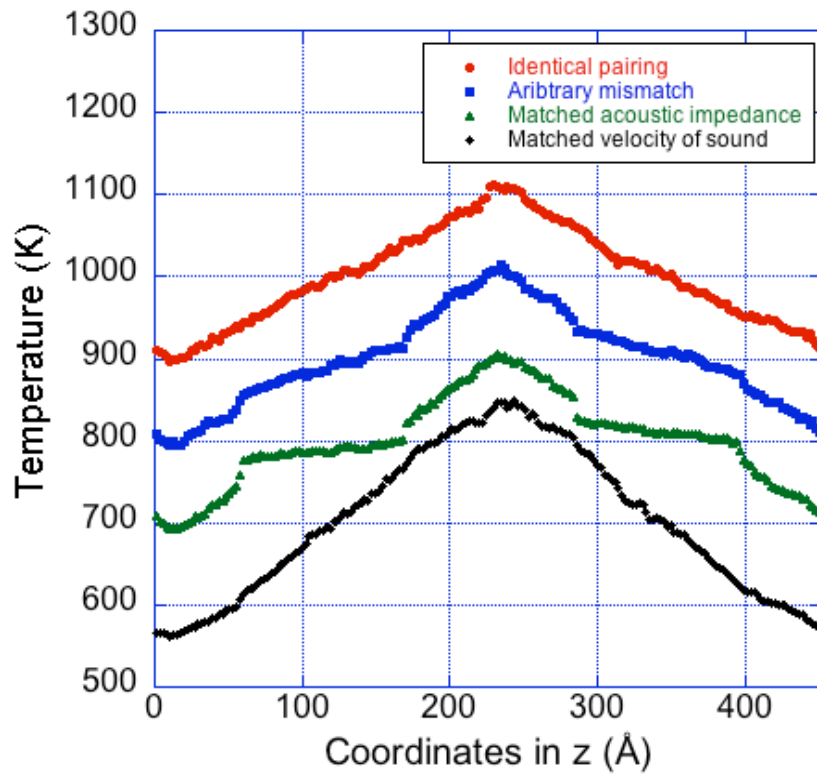
Figure 3.4 Temperature profiles for 4 different pairings of the structurally congruent

interfaces

3.3.3 Phonon mode coupling across the interface

In the real world, the density and modulus of materials cannot be easily adjusted at will and therefore it is difficult to have materials with matched acoustic impedance or speed of sound. For the weakly boned CuPc/metal systems, such mismatches between the two materials are large. The VDOS for metal and CuPc differs tremendously as is shown in Fig. 3.5.
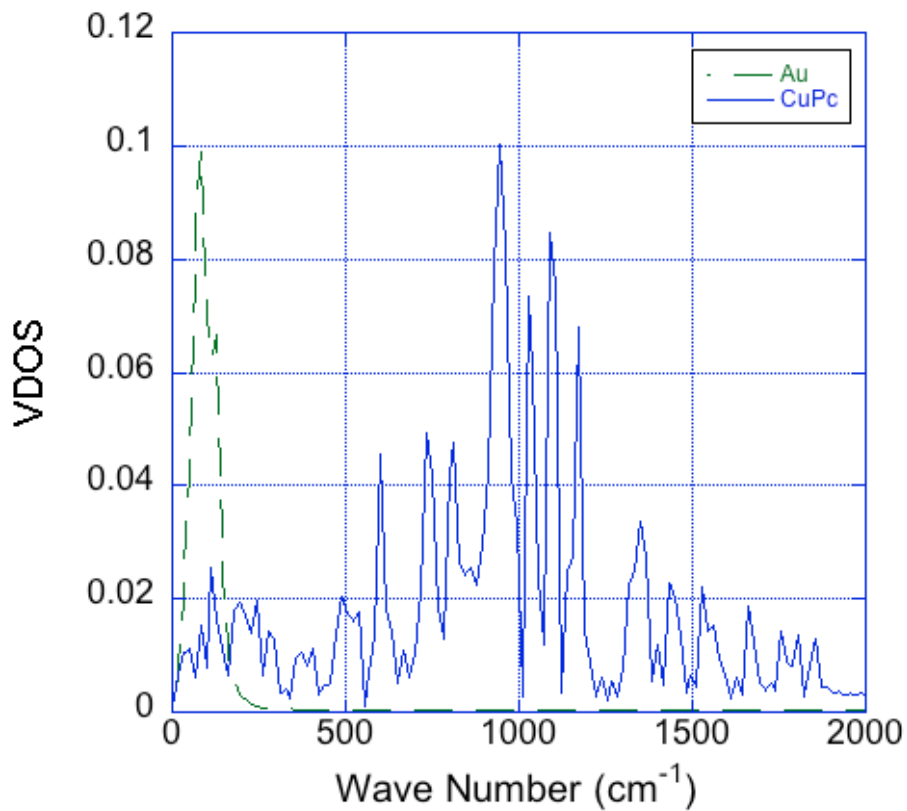
Figure 3.5 VDOS of Au and CuPc

The VDOS peaks of metal do not overlap with those of CuPc very well, especially in the acoustic region which dominants phonon transport in these materials. Here we examine how specific phonon mode is transported through the CuPc/Au

interface. We disturb one atomic plane oriented parallel to the interface by moving all the atoms in that layer 0.5 Å towards the interface and releasing it. We then compare atomic trajectories to those of a simulation of the same system with no initial perturbation, and record the difference in coordinates and velocities for each atom as a function of time. The Fourier transform of these differential trajectories yields the vibrational spectrum of the additional phonon modes introduced by the initial perturbation. Spectra are calculated for both Au and CuPc, and shown Fig. 3.6 at 0.25 ps, 0.5 ps, and 1.0 ps after introducing the perturbation. Almost immediately after the additional thermal energy introduced by the perturbation arrives at the Au-CuPc interface, vibrational modes in CuPc are excited that are quite different in frequency from those in Au (Fig. 3.6a). This indicates that phonon modes arriving from Au couple to modes in CuPc without requiring a strong match in frequency. This point is illustrated more clearly by simultaneously examining the product of the two spectra, which identifies the overlap of spectral features, and is shown in the lower part of each graph. Accordingly, while the principal overlap between the two spectra occurs at about 40 cm^{-1} and 120 cm^{-1}, the intensity of peaks above 260 cm^{-1} grows immediately and more rapidly than that of the peaks in the spectral overlap regime. As time progresses, the vibrational spectra associated with the differential motion originating from the perturbation gradually develop all spectral features of the regular VDOS of both phases (see Fig. 3.5), reflecting the fact that the additional perturbation energy is dissipated by spreading onto all available vibrational excitations. During this process, the magnitude of the product of spectra in the overlap regime momentarily rises, but this is more likely due to the redistribution of energy among the modes associated with CuPc vibrations (e.g., decay of

higher-frequency excitations) than due to direct coupling between modes in Au and CuPc.

These observations indicate that the majority of the heat transfer between these dissimilar materials is achieved through anharmonic coupling between their respective characteristic modes. In other words, a mismatch between the vibrational properties of the two adjacent materials is not necessarily a strong impediment for heat transfer, whereas strongly adhesive bonding at the interface is likely to facilitate anharmoninc coupling.
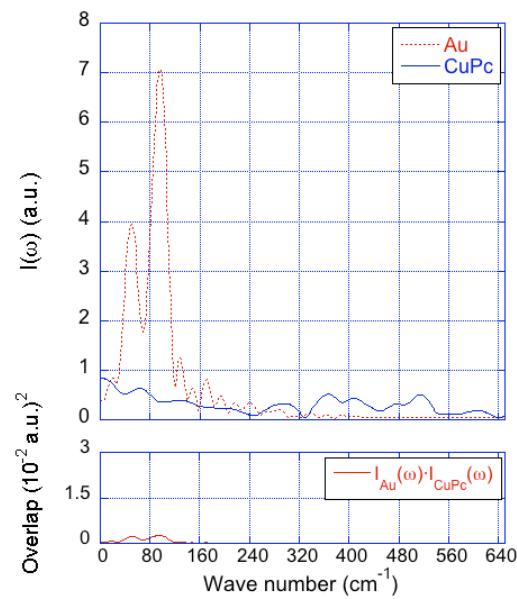
(a)
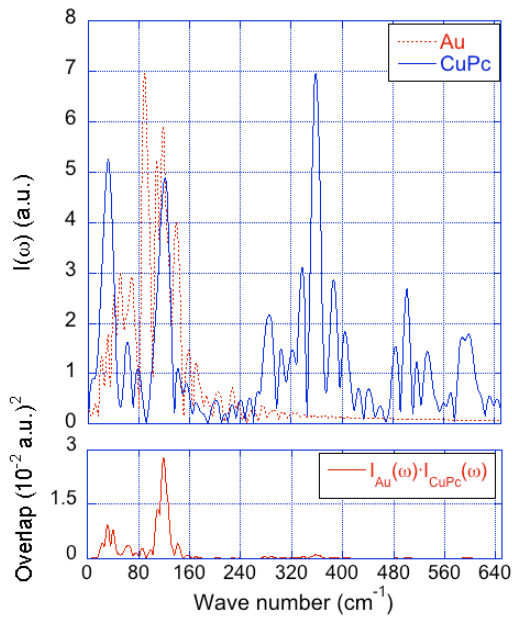
(b)
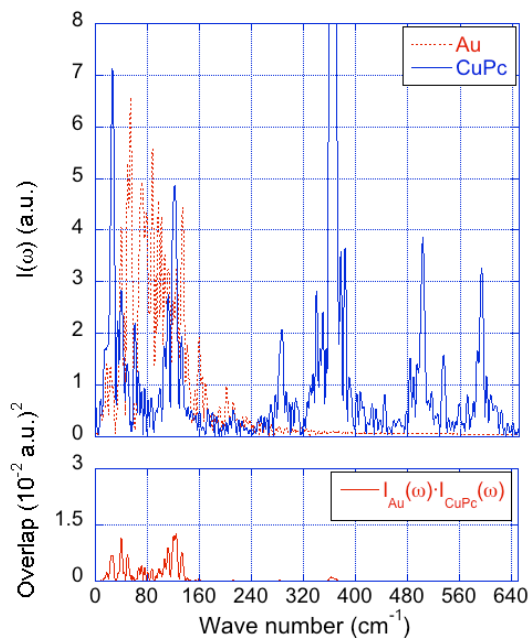
(c)

Figure 3.6 Vibrational density of states spectra attributed to the differential trajectories
upon displacing a single Au plane for the Au and CuPc layers (upper pane), and the

product of these spectra (lower pane) at different times after the initial perturbation: (a)

0.25 ps, (b) 0.5 ps, (c) 1 ps.

3.3.4   Calculation of work of adhesion at CuPc-metal interfaces

As pointed out earlier, experimental observations reveal a correlation betweenzz interfacial bonding strength and TBC for these weakly coupled interfaces. In MD simulations, the bonding strength can be easily tuned by scaling the factor ε in equation (3.1). This allows us to conduct a parametric study of the effect of interfacial adhesion on the heat transfer properties of the interface. The work of adhesion at the interface is calculated as the difference between the total energies of a metal and a CuPc slab in contact with each other, and the sum of the energies of the two slabs separated so as to expose the corresponding two free surfaces. The adjoining slab system with the CuPc/metal junction is first relaxed at room temperature with periodic boundary conditions applied in all dimensions. The total energy of the system is minimized under these conditions to obtain E_p. The two slabs are then separated at the CuPc/metal interface by a distance beyond the range of the force field, leaving two free surfaces, one with CuPc and the other with metal atoms. The total energy of the system with free surfaces is again minimized to yield E_s. The work of adhesion at the interface is then calculated as $W = E_s - E_p$. The calculated work of adhesion is plotted versus the magnitude of ε in Figure 3.7 for different CuPc/metal interfaces. In this graph, the ratio of 1 corresponds to the ε calculated from mixing rules of the force field and it can be seen that there's a linear relationship between the work of adhesion and ε. Thus the bonding strength of the two materials can be controlled via the ε parameter. Using this approach,

we calculated the work of adhesion for interfaces between CuPc and three fcc metals with (111) surface: Al, Au, Ag.
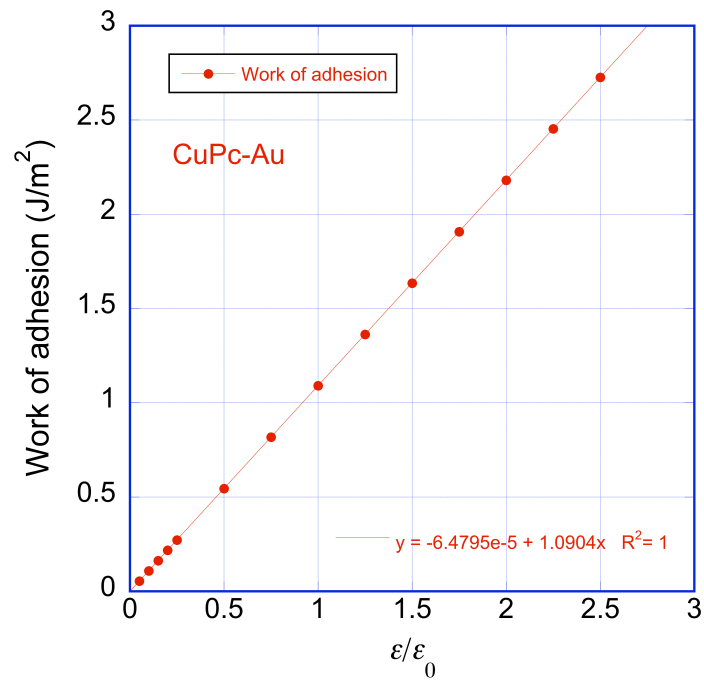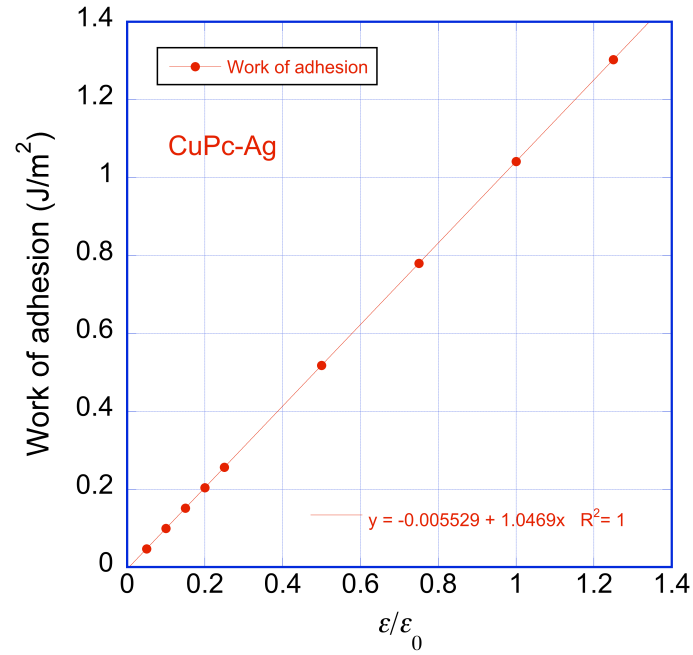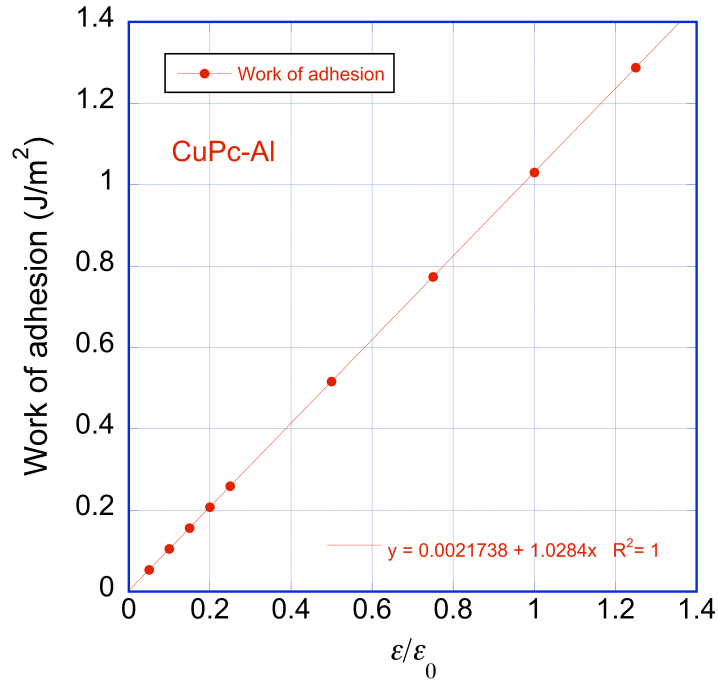
Figure 3.7 Work of adhesion versus ε for CuPc-Ag,Au,Al, ε_0 corresponds to the potential well depth between different atom species calculated from mixing rules(Eqn. 3.2-3.3)

3.3.5   Effect of interfacial bonding strength on the TBC

We calculated the TBC for the same interfacial systems.. The metallic phases in all systems have the same crystal structure and closely matched lattice constants, i.e., 4.05 ± 0.04 Å, which allows us to make a rigorous comparison between their heat transport behaviors.   For these weakly bonded systems, we find a clear log-linear relationship between the work of adhesion and TBC of CuPc-metal interfaces, as shown in Figure 3.8.

88
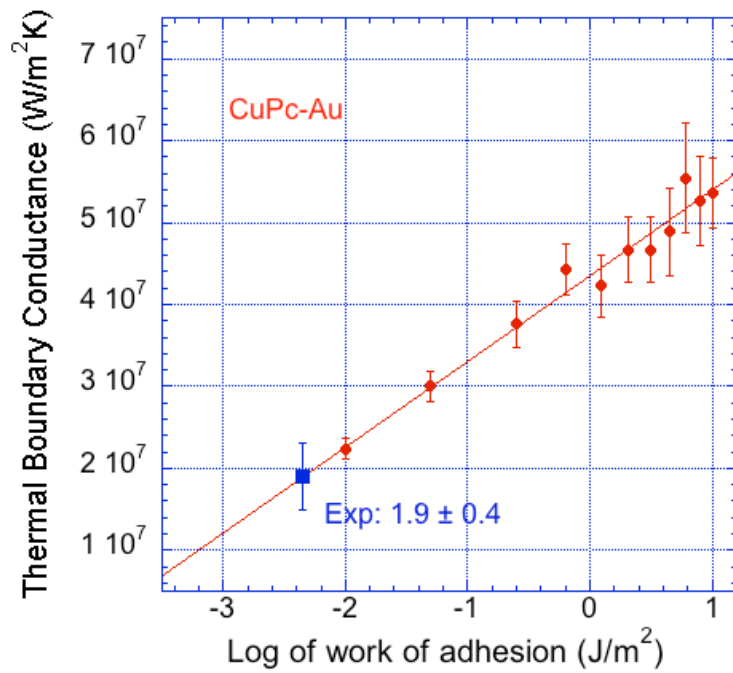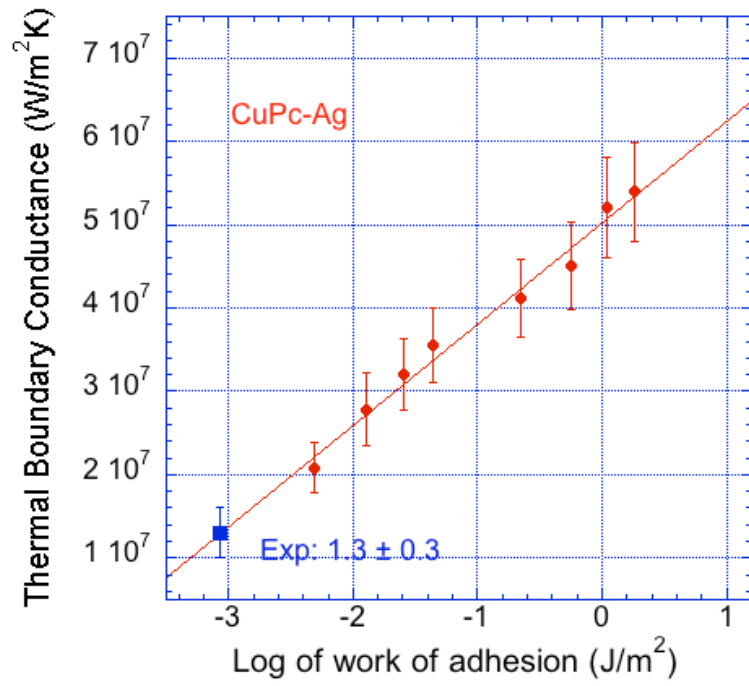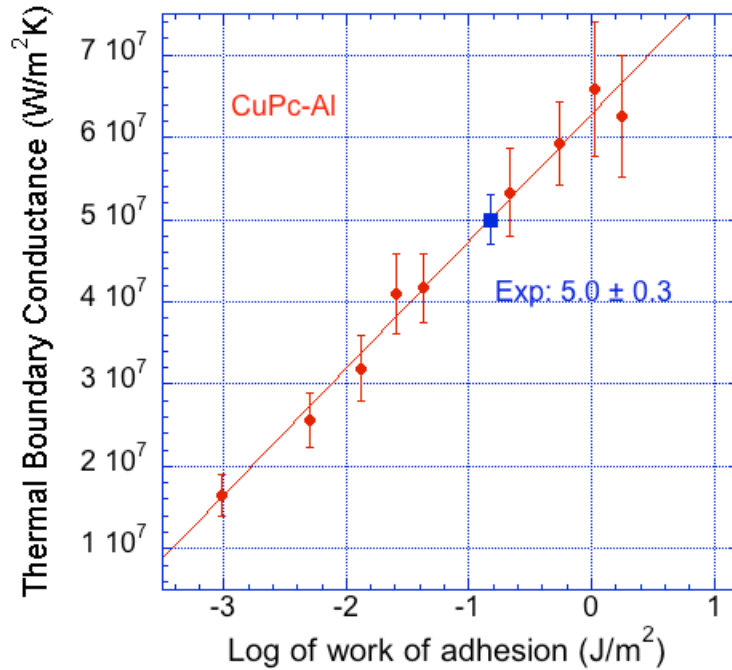
Figure 3.8 Thermal boundary conductance versus work of adhesion for CuPc/Ag,

CuPc/Au, and CuPc/Al interfaces

Accordingly, the TBC decreases as the interfacial bonding becomes weaker, which is in agreement with the experimental peel-off test observations.[10] Superimposed on the results from simulations in these figures are the experimentally measured TBC for these materials pairings.[27] The intersections of these TBC levels with the best fit lines allow us to estimate the work of adhesion between CuPc and these three metals. The results are summarized in Table 3.2. The free surface energy of CuPc[28] is reported to be 0.035 J/m^2. The work of adhesion for one material is the work needed to create a free surface in the material. Thus the work of adhesion for CuPc is: $W_{CuPc} = 2 \cdot \gamma = 0.07$ J/m^2, which is larger than the work of adhesion for CuPc-Ag and comparable with CuPc-Au interfaces. This indicates that the bonding strength between CuPc and gold/silver

substrate is very weak. The experimental peel-off test results confirm the weak bonding between CuPc and Au or Ag: over 90% of the film breaks at the CuPc/metal interface in the silver/metal/CuPc/ITO structure. On the other hand, Al shows strong bonding with CuPc and in experiment, less than 1% peel-off is observed. In Figure 3.9, the estimated work of adhesion calculated from MD simulations is plotted versus the fraction of CuPc, in terms of contact area, that cleanly peeled off the surface for different CuPc/metal systems. A strong correlation is observed in this plot: higher work of adhesion or stronger interfacial bonding strength result in a lower fraction of the substrate surface completely freed of CuPc, albeit more CuPc/metal systems may need to be explored to rigorously confirm such a correlation between work of adhesion and peel off percentage.
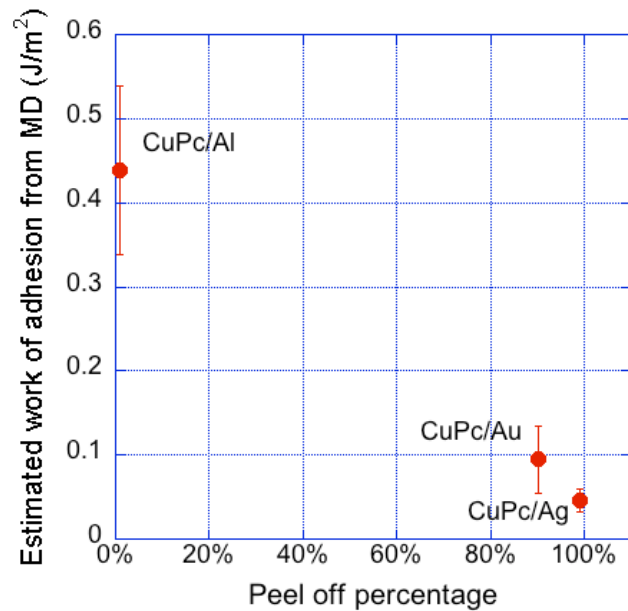
Figure 3.9 Estimated work of adhesion using MD vs. peel off percentage in experiments

Linear behavior in lin-log representation of the TCB vs. work of adhesion data in Fig. 3.8 means that plotted vs. a linear work of adhesion axis, the TCB tend to saturate

towards high work of adhesion values. This indicates that for interfaces with strong bonding, all the existing transmission modes are supported and further increments in bonding strength does not enhance the transport rates.

3.4 Conclusion

We investigated the effect of interfacial bonding strength on the thermal boundary conductance across CuPc-metal interfaces using nonequilibrium MD simulations. We control the interfacial bonding strength by changing the potential well depth parameter, ε, in the 9-6 Lennard-Jones potential for Van der Waals interactions.

When we fixed the interfacial bonding strength and only controlled the density and elastic modulus of the metal substrate in CuPc-metal systems, MD calculations of TBC predicted the same trend as the AMM results. However, eliminating the effect of interfacial bonding strength would result in false predictions both from MD and AMM calculations: CuPc-Ag would have a larger TBC than CuPc-Au interface while in experiment, the opposite trend was observed. This clearly indicated that interfacial bonding strength should be the dominant factor on the TBC at CuPc-metal interfaces. Interfacial bonding strength was controlled for different CuPc-metal (Ag, Au, Al) systems and TBC with different bonding strength was calculated from MD simulations. For weak bonding, a clear log-linear relationship was observed between work of adhesion and TBC at CuPc-metal interfaces. For strong bonding, TBC values saturated as expected. The work of adhesion for different CuPc-metal systems in experiment were also estimated from MD simulations: CuPc-Ag ~ 0.046 J/m^2, CuPc-Au ~ 0.095 J/m^2, CuPc-Al ~ 0.439 J/m^2, which agreed with peel-off experiment results very well. From

this we demonstrated strong correlation between interfacial bonding strength and TBC at

weakly bonded organic-inorganic interfaces.

3.5   References

1.   Eremtchenko, M., Schaefer, J. A. & Tautz, F. S. Understanding and tuning the epitaxy of large aromatic adsorbates by molecular design. *Nature* **425**, 602-605 (2003).

2.   Kilian, L., Umbach, E. & Sokolowski, M. Molecular beam epitaxy of organic films investigated by high resolution low energy electron diffraction (SPA-LEED): 3,4,9,10-perylenetetracarboxylicacid-dianhydride (PTCDA) on Ag(111). *Surf Sci* **573**, 359-378 (2004).

3.   Sun, Y. R. et al. Management of singlet and triplet excitons for efficient white organic light-emitting devices. *Nature* **440**, 908-912 (2006).

4.   Kalinowski, J. et al. Quenching effects in organic electrophosphorescence. *Phys Rev B* **66**, ARTN 235321 (2002).

5.   Kilian, L. et al. Role of intermolecular interactions on the electronic and geometric structure of a large pi-conjugated molecule adsorbed on a metal surface. *Phys Rev Lett* **100**, ARTN 136103 (2008).

6.   Kapitza, P. L. The study of heat transfer in helium II. *J Phys-ussr* **4**, 181-210 (1941).

7.   POLLACK, G. L. KAPITZA RESISTANCE. *Rev Mod Phys* **41**, 48-4& (1969).

8.   SWARTZ, E. T. & POHL, R. O. THERMAL-BOUNDARY RESISTANCE. *Rev Mod Phys* **61**, 605-668 (1989).

9.   Huxtable, S. T. et al. Interfacial heat flow in carbon nanotube suspensions. *Nat Mater* **2**, 731-734 (2003).

10. Jin, Y. et al. Thermal boundary resistance of copper phthalocyanine-metal interface. *Appl Phys Lett* **98**, ARTN 093305 (2011).

11. Schmidt, A. J., Collins, K. C., Minnich, A. J. & Chen, G. Thermal conductance and phonon transmissivity of metal-graphite interfaces. *J Appl Phys* **107**, ARTN 104907 (2010).

12. Stevens, R. J., Smith, A. N. & Norris, P. M. Measurement of thermal boundary conductance of a series of metal-dielectric interfaces by the transient thermoreflectance technique. *J Heat Trans-t Asme* **127**, 315-322 (2005).

13. Koh, Y. K., Cao, Y., Cahill, D. G. & Jena, D. Heat-Transport Mechanisms in Superlattices. *Adv Funct Mater* **19**, 610-615 (2009).

14. Fagas, G., Kozorezov, A. G., Lambert, C. J. & Wigmore, J. K. Lattice-dynamical

calculation of phonon scattering at a disordered interface. *Physica B* **263**, 739-741 (1999).

15. Fagas, G. et al. Lattice dynamics of a disordered solid-solid interface. *Phys Rev B* **60**, 6459-6464 (1999).

16. PETTERSSON, S. & MAHAN, G. D. THEORY OF THE THERMAL-BOUNDARY RESISTANCE BETWEEN DISSIMILAR LATTICES. *Phys Rev B* **42**, 7386-7390 (1990).

17. YOUNG, D. A. & MARIS, H. J. LATTICE-DYNAMICAL CALCULATION OF THE KAPITZA RESISTANCE BETWEEN FCC LATTICES. *Phys Rev B* **40**, 3685-3693 (1989).

18. STONER, R. J. & MARIS, H. J. KAPITZA CONDUCTANCE AND HEAT-FLOW BETWEEN SOLIDS AT TEMPERATURES FROM 50 TO 300 K. *Phys Rev B* **48**, 16373-16387 (1993).

19. Stevens, R. J., Zhigilei, L. V. & Norris, P. M. Effects of temperature and disorder on thermal boundary conductance at solid-solid interfaces: Nonequilibrium molecular dynamics simulations. *Int J Heat Mass Tran* **50**, 3977-3989 (2007).

20. Torii, D., Ohara, T. & Ishida, K. Molecular-Scale Mechanism of Thermal Resistance at the Solid-Liquid Interfaces: Influence of Interaction Parameters Between Solid and Liquid Molecules. *J Heat Trans-t Asme* **132**, ARTN 012402 (2010).

21. Ong, Z. Y. & Pop, E. Molecular dynamics simulation of thermal boundary conductance between carbon nanotubes and SiO2. *Phys Rev B* **81**, ARTN 155408 (2010).

22. Shen, M., Evans, W. J., Cahill, D. & Keblinski, P. Bonding and pressure-tunable interfacial thermal conductance. *Phys Rev B* **84**, ARTN 195432 (2011).

23. Heinz, H., Vaia, R. A., Farmer, B. L. & Naik, R. R. Accurate Simulation of Surfaces and Interfaces of Face-Centered Cubic Metals Using 12-6 and 9-6 Lennard-Jones Potentials. *J Phys Chem C* **112**, 17281-17290 (2008).

24. MullerPlathe, F. A simple nonequilibrium molecular dynamics method for calculating the thermal conductivity. *J Chem Phys* **106**, 6082-6085 (1997).

25. QUESNEL, D. J., RIMAI, D. S. & DEMEJO, L. P. ELASTIC COMPLIANCES AND STIFFNESSES OF THE FCC LENNARD-JONES SOLID. *Phys Rev B* **48**, 6795-6807 (1993).

26. Foiles, S. M., Baskes, M. I. & Daw, M. S. Embedded-atom-method functions for the fcc metals Cu, Ag, Au, Ni, Pd, Pt, and their alloys. *Physical Review B* **33**, 7983 (1986).

27. Jin, Y., Shao, C., Kieffer, J., Pipe, K. P. & Shtein, M. Origins of thermal boundary conductance of interfaces involving organic semiconductors. *Journal of Applied Physics* **112**, 093503 (2012).

28. Wei, H. X. et al. Thermal annealing-induced vertical phase separation of copper phthalocyanine: Fullerene bulk heterojunction in organic photovoltaic cells. *Appl Phys Lett* **97**, ARTN 083302 (2010).

Table 3-1 Experimental TBC results for CuPc/Ag and CuPc/Au interfaces

	Ag	Au
Exp. Elastic modulus (GPa)	100	180
Lattice Constant (Å)	4.09	4.08
Atomic Weight (g/mol)	107.8682	196.97
Exp. TBC (10^8 W/m^{2}K)	1.3 ± 0.3	1.9 ± 0.4

Table 3-2 Estimated work of adhesion for CuPc-metal interfaces

	Work of Adhesion (J/m^2)	exp. TBC (10^8 W/m^{2}K)
CuPc-Ag	0.046 ± 0.014	1.3 ± 0.3
CuPc-Au	0.095 ± 0.04	1.9 ± 0.4
CuPc-Al	0.439 ± 0.100	5.0 ± 0.3

Chapter 4 Active Control of Thermal Transport using PVDF Thin Films – An MD Simulation Prediction

Synopsis

Molecular organics have become materials of considerable interest for electronic devices, due to their low manufacturing cost. Thermal management is a crucial factor in microelectronics because of the high power density associated with miniaturization. In this chapter, we discuss how the thermal transport properties of poly(vinylidene difluoride) (PVDF) thin films depend on the magnitude and direction of externally applied electric fields, as revealed molecular dynamics (MD) simulations. Accordingly, the thermal conductivity of PVDF thin films increases with the strength of the applied electric field. Our simulations predict a 33% conductivity boost at 80% of the breakdown field strength. A poled PVDF film possesses a remnant conductivity enhancement that can be removed by an opposing electric field. Finally, the applied electric field raises the adhesive force to the substrate and thereby increases the interfacial thermal boundary conductance by a factor of up to 6. We elucidate the observed behaviors based on the comparison of the phonon spectra of PVDF structures exhibiting various degrees of polarization.

4.1 Introduction

Due to the ever-smaller feature sizes of integrated circuits, thermal management has become a bottleneck issue in device performance. This particularly true when heat dissipation must occur at heterojunctions dissimilar materials, involving disordered molecular organics. Thermal conductivity and the ability to control it in such materials systems has therefore been the subject of extensive investigations.[1-4] In earlier chapters we established that the interfacial adhesion is the dominant factor governing thermal conductance at weakly bonded CuPc/metal interfaces.[2] Similarly, Hu and coworkers reported that, to improve thermal transport across the interface between single-crystalline silicon and carbon nanotubes (CNT), it is more important to tailor the interfacial bond strength than to balance the elastic moduli of adjoining materials via MD simulations.[1] Stevens et al. studied thermal transport in metals using MD simulations, using a Lennard-Jones (L-J) potential to describe atomic interactions, and found that inelastic phonon scattering, which traditional theories like acoustic mismatch model (AMM) and diffuse mismatch model (DMM) tend to ignore, has a high impact on interfacial conductance. Increasing the temperature of the L-J metal system would increase the thermal conductance linearly. Adding defects at the interface or introducing interfacial mixing creates scattering sites and is accompanied by a reduction in the thermal boundary conductance.[4] However, these studies focus on passive thermal transport, exploring measures to tune thermal transport properties only during device fabrication, but they do not examine the potential for active control of thermal transport in organic materials. With regard to the latter prospect, Shen et al. predict, based on MD simulations, that

applying pressure to metal junctions can improve thermal transport in weakly bonded interfaces.[3] This effect subsides in more strongly bonded interfaces, and in most actual devices, it would be impractical to control thermal transport using high pressures. For example, pressure can significantly affect the morphology and other properties of organic materials, and has the potential to permanently damage devices.

In this chapter, we investigate how thermal transport properties of organic polymers depend on externally applied electric fields. Although many types of electroactive polymeric materials are available, poly(vinylidene difluoride) (PVDF) is of particular interest because of its strong piezo- and pyroelectric response, high breakdown voltage, low cost, and graceful failure nature.[5] There are three common phases for PVDF, a, b and g. The α-phase consists of a series non-polar antiparallel chains and has a chain conformation of approximately TGTG (trans-gauche-trans-gauche).[6,7] b-PVDF has a planar TTTT (all trans) chain conformation.[6,7] The γ-phase has a TTTGTTTG' chain conformation.[8] Among these three phases, the β-phase exhibits the largest spontaneous polarization per unit cell and thus exhibits superior ferroelectric and piezoelectric properties.[9] It is therefore important to maximize β-phase in PVDF films. Many efforts have been exerted in fabricating PVDF films with high percentage of β-phase for electronic applications. PVDF films are commonly produced via deposition from solution. Using DMF (dimethylformamide) as a solvent has been reported to generate significant amounts of polar β-phase in the resulting film. However, the β-phase is only stable at temperatures below 50° C, and these films are too porous to be used in device applications.[9,10] Dense β-phase PVDF films can be obtained by spin coating a PVDF/DMF solution with addition of $Mg(NO_3)_2 \cdot 6H_2O$, and drying at $100°C$.[9,10] It is

also possible to convert the other PVDF phases into β-phase once a film has been deposited. For example, mechanically stretching a PVDF film tends to orient the molecular bonds. The most practical way to achieve strong piezoelectric coefficients is via poling, i.e., orienting molecules by applying electrical fields in excess of 10 MV/m. Poling can be carried out while the film is under tension or while it is heated. Salimi *et al*. showed that a maximum β-phase concentration can be achieved at 90 °C upon stretching a film made of α- PVDF film.[11,12] In contrast to such elaborate experimental procedures for achieving high-quality β-phase PVDF films, MD simulations offer a rather more expedient means for controlling the degree and type of crystallinity in structural models of dense PVDF thin films. For this investigation we took advantage of this fact in order to explore the possibility of using electric fields to actively control thermal transport properties in PVDF films, to identify the underlying mechanisms, and to assess the magnitude of the effect one may expect in experimental systems.

This chapter is organized as follows: in section 2 we describe the molecular dynamics simulation details, in section 3 we discuss the limit of electric fields that is estimated from Stark-Garton model to be used in MD simulations. Simulation results are given and discussed in Section 4 and a summary of work and conclusions are presented in Section 5.

4.2   Molecular dynamics simulation details

In our study, we simulate PVDF chains with eight –[CF_2–CH_2]– repeat units, and two terminal CH_3 units. The simulation system consists of 250 such PVDF molecules. The dimension of the simulation box is $40 \times 40 \times 120$ Å, which we verified to be

sufficiently large to avoid system size effects due to periodic boundary conditions. The COMPASS force field is used to describe inter- and intra-molecular interactions of PVDF. At the outset of our investigation, a specific force field for PVDF was not available in the literature. For instance, Zeng et al. studied elastic properties of PVDF using MD simulation features in commercially available Materials Studio but no details are provided about the force field.[13] Polarization switching phenomena of PVDF was studied by Bystrov using HyperChem package, giving no potential details either.[14] However, PVDF chains have a similar molecular structure as alkanes, except that on every second carbon hydrogen is replaced by fluorine. We therefore adapted the COMPASS force field parameters for alkanes to simulate PVDF,[15] essentially by changing the mass, size, and partial charge of fluorine atoms. Since we expect that the behaviors under scrutiny are principally governed by electrostatic interactions, we focused on optimizing the partial charges associated with each species. Partial charges were derived from DFT calculations using Gaussian 09 simulation package with the B3LYP/6-311G(d,p) basis set. The Muliken charge identification scheme is used and the calibrated partial charges for each labeled atom are shown in Fig. 4.1. Note how the partial charges of carbon coordinated by hydrogen and fluorine alternate between negative and positive values. Also, near the end groups, the partial charges of species deviate from those in the central segment of the polymer chain, but reach a steady value about four repeat units away from the chain ends.
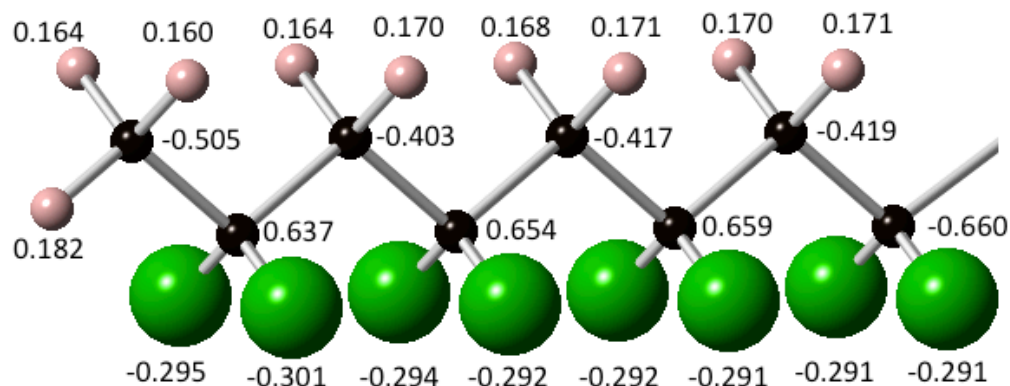
Figure 4.1 PVDF polymer chain in the β-conformation, showing a terminal hydrogen on the left and side (pink) and four CH_2–CF_2 repeat units (carbon in black, fluorine in green). Atoms are labeled with the partial charges determined using DFT calculations. Note that chain termination affects these charges. Repeat units are shown until charges stabilize.

Our systems are created using the following procedure: the PVDF molecules are placed loosely in space and equilibrated under NPT conditions at 600 K and zero pressure, which is significantly above the melting temperature of the system and provides for significant structural mobility. During this thermalizing phase we optionally apply

electric fields of different strength (i.e., from 0 to 1 V/Å) to the system so as to create structures with different levels of ordering. Once the system reaches equilibrium at high temperature, it is quenched to 100 K at a cooling rate of 25 K/ps, while the electric field is maintained. A temperature well below the glass transition of PVDF was chosen to prevent thermally induced structural relaxation even in the high-temperature segments of the specimens, once thermal gradients are imposed to calculate thermal conductance data as described below.

4.3   Force field validation

The purpose of this investigation is to establish whether electric fields applied to electro-active polymers have an effect on their thermal transport behavior. We therefore verify the degree of realism with which the COMPASS force field that we use to simulate PVDF allows us to reproduce the structural response of the material to imposed electrical fields. As with many force fields, computational expediency is achieved by simplifying underlying physical models. For example, in the COMPASS force field fixed point charges are assigned to each atom. Neither charge transfer nor local polarization of the charge distribution is accounted for in this interaction model. Therefore, a larger electric field may be needed in our MD simulation to achieve the same charge polarization as in experiments. In other words, in our simulations dipoles form entirely at the expense of bond deformation, and the interaction model may underestimate the charge polarizability of PVDF. Case in point, in their MD simulations, Ma *et al.* applied electric fields of 2 V/Å to self-assembled monolayers (SAM) to study electric field induced conformational transitions and frictional performance of SAM films.[16] However, realistically a field of

this magnitude exceeds the breakdown voltage for most materials. Indeed, Zhou et al. report the breakdown voltage for PVDF is 700 – 800 MV/m at room temperature.[17]

For our investigation it would be most appropriate to consider the effects of applied electric fields not exceeding the breakdown field strength of the simulated structure. While this field strength cannot easily be determined via direct non-equilibrium MD simulations of the process in question, we can derive a good estimate of the breakdown voltage based on the knowledge of the elastic modulus of the material. To this end, we employ the widely used Stark-Garton electromechanical breakdown model,[18-21] which allows us to estimate the breakdown voltage for our simulated PVDF structures based on the calculated elastic properties.. This model is derived from the balance between mechanical stress due to the elastic response of the material and the field induced Maxwell stress. Assuming that the electric field exerts a compressive force on a PVDF film of initial thickness d_0, equivalent to a biaxial planar stress in the perpendicular directions, the film is contracting to a thickness ld_0. The force balance is expressed by

$$Y\left(\ln \lambda^{-1}\right)^N = \frac{1}{2}\varepsilon E^2, \quad (4.1)$$

where Y is the Young's modulus of PVDF, ε is the product of the dielectric permittivity of vacuum and the relative permittivity of PVDF, i.e., $\varepsilon = \varepsilon_0 \varepsilon_r$, and E is the electric field strength resulting from the voltage V applied across the film thickness, i.e., $E = V/\lambda d_0$. N is the exponent that accounts for the non-linearity in the elastic response of the material. As the voltage is increased, the force on the film rises and its thickness decreases, which

in turn enhances the applied field strength. This self-reinforcing effect by the applied voltage leads to an instability, at the maximum voltage the material can sustain, or breakdown voltage. We can determine this breakdown voltage as the maximum in the relationship

$$\frac{1}{2}\varepsilon\left(\frac{V}{d_0\lambda}\right)^2 = Y\left(\ln\lambda^{-1}\right)^N \Rightarrow V = \sqrt{\frac{2Y}{\varepsilon}}d_0\lambda\left(\ln\lambda^{-1}\right)^{N/2}. \qquad (4.2)$$

Taking the derivative of this expression with respect to *l*, and equating it to zero yields $\left(\ln\lambda_c^{-1}\right) = N/2 \Leftrightarrow \lambda_c = e^{-N/2}$, and for the breakdown voltage

$$V_c = \sqrt{\frac{2Y}{\varepsilon}}d_0\left(\frac{N}{2}\right)^{N/2}e^{-N/2}. \qquad (4.3)$$

The factor N depends on the material. We chose $N = 1$ for this calibration, as it causes the strongest deviation from linear elasticity and smallest breakdown voltage for a given elastic modulus of the material. It therefore provides the most conservative estimate for the predicted effect. According to eq. (4.3), the breakdown voltage is proportional to the square root of the Young's modulus, which is predominantly determined by the curvature of the interaction potential and the polymer network topology. Hence, we next determine the Young's modulus of our simulated PVDF structure using a simulated tensile test experiment. At the strain rate that is reasonably achievable in simulations, i.e., 10^9 s^{-1}, and at 100 K, the Young's modulus of our simulated PVDF is 20 GPa. Experimentally reported elastic moduli range between 2.9 GPa for the isothermal modulus[22] to 16 GPa for the adiabatic modulus, measured using Brillouin light scattering.[23] The modulus derived from MD simulations should be

compared to the adiabatic modulus, and the value we obtained is therefore quite reasonable for the intended purpose, especially considering that our force field was derived from that for alkane chain molecules by optimizing only species size and charge distribution.

Nevertheless, in order to provide for convenient comparisons between the effects observed in our simulation and those that may be expected in experiments, we normalize the applied electric field in terms of the electromechanical breakdown field strength, E_c, for the simulated structure. In other words, if we observe a change in the thermal transport properties of PVDF as a result of applying an electric field of strength E_S in our simulations, we expect to see the same change in an experimental system upon applying a field of strength $E_X = E_S\left(E_{c,X}/E_{c,S}\right)$, where the subscripts X and S denote experimental and simulation values, respectively.
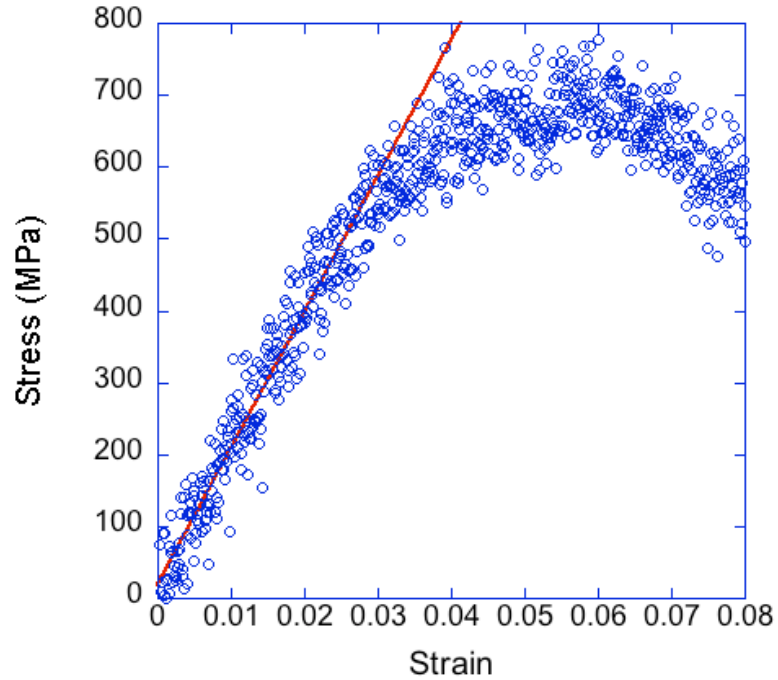
Figure 4.2 Stress strain curve from tensile test simulation of PVDF

Fig. 4.2. shows the initial close to linear elastic region of the stress-strain relationship obtained from the tensile test simulation, which served to compute the elastic modulus from the slope in the low-strain region. Using the Young's modulus so obtained, we calculate a breakdown field strength of E_c = 1.22 V/Å in our PVDF model system, based on Stark-Garton model. With value in mind, in our simulations described in the following, we applied electric fields with strengths between 0 and 1 V/Å, i.e., up to 82% of the breakdown field strength.
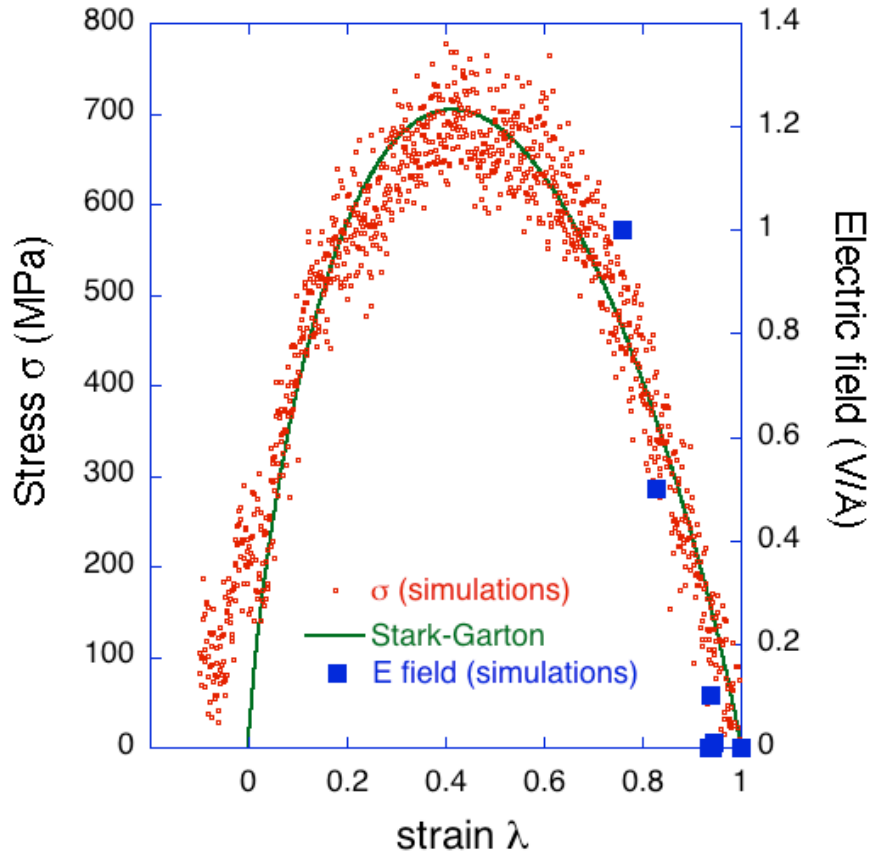
Figure 4.3 Comparison between the stress-strain relationship resulting from the tensile test simulations, the Stark-Garton model, and the film deformation resulting from an applied electric field.

In Fig. 4.3 we compare the complete data set of the stress-strain relationship obtained from the tensile test simulations with the Stark-Garton model. To this end the tensile strain resulting from the applied stress was converted to a compressive perpendicular strain using a literature Poisson's ratio value of 0.34. The curve does not represent a best fit because the stress applied in simulations is uniaxial, as opposed to biaxial as the model assumes. We felt that this deviation from the model conditions was too severe to attempt extracting parameter values from a best fit. Instead we present the

graph in order to illustrate the above discussion and provide a qualitative measure for the reasonableness of using this model in the present context. The graph also includes deformation data obtained by applying electric fields to the PVDF structures in our simulations, as discussed below. The left- and right-hand side scales are matched based on the breakdown voltage determined using the Stark-Garton model.

4.4 Results and discussion

4.4.1 Glass transition of PVDF constrained by electric fields

The poling at high temperature and maintaining a strong electric field during cooling of the PVDF structures appears to have an effect on the glass transition behavior of this system. Fig. 4.4 shows the volume-temperature dependence of PVDF configurations cooled at the same rate but with different strength electric fields applied. With no field applied, we observe the two regimes typical for a glass-forming material, i.e., that of a supercooled liquid where volume changes involve structural rearrangements as well as anharmonic contributions to the bond distance, and the glassy regime, which is dominated by only the latter. The glass transition region for the simulated PVDF extends between 300 and 400 K, compared to the experimentally determined T_g of 260 K. This discrepancy can be attributed to the very much higher quench rates in simulations than in experiments, a known shortcoming of MD simulations. Upon applying an electric field we observe an intermediate regime between glass and supercooled liquid, which becomes more pronounced, the stronger the field. The intermediate regime is essentially apparent

by a more extensive, on the temperature axis, glass transition region, characterized by a deviation towards larger volumes relative to the bracketing linear regimes.

Note that upon applying the field at high temperature, the liquid phase is already compacted, more so, the higher field. This is reflective of packing and partial ordering, i.e., alignment of dipoles. Hence, in the glass formation process a part of the structural reorganization that would normally take place upon lowering the temperature and thereby removing entropic contributions to the free energy of the liquid, has been forcefully removed by the applied field, thus shifting the onset of the glassy behavior towards higher temperature, perhaps due to the formation of glass-like domains. Surprisingly, however, structural relaxation does continue to take place, albeit to a lesser extent in terms of the absolute volume change, down to temperatures close to that for a system cooled with no field applied, i.e., approximately 300 K. This indeed points towards structural heterogeneity, i.e., the transition between structurally distinct states, present in spatially adjacent domains, as an aspect of glass formation – especially, since we anticipate partial ordering to result from the application of a strong electric field. Thermal conductivity calculations show a possible positive correlation between the glass transition temperature and the thermal conductivity, i.e., the higher T_g, the higher the thermal conductivity. However, more data are needed to fully establish such a correlation, which is beyond the scope of this thesis.
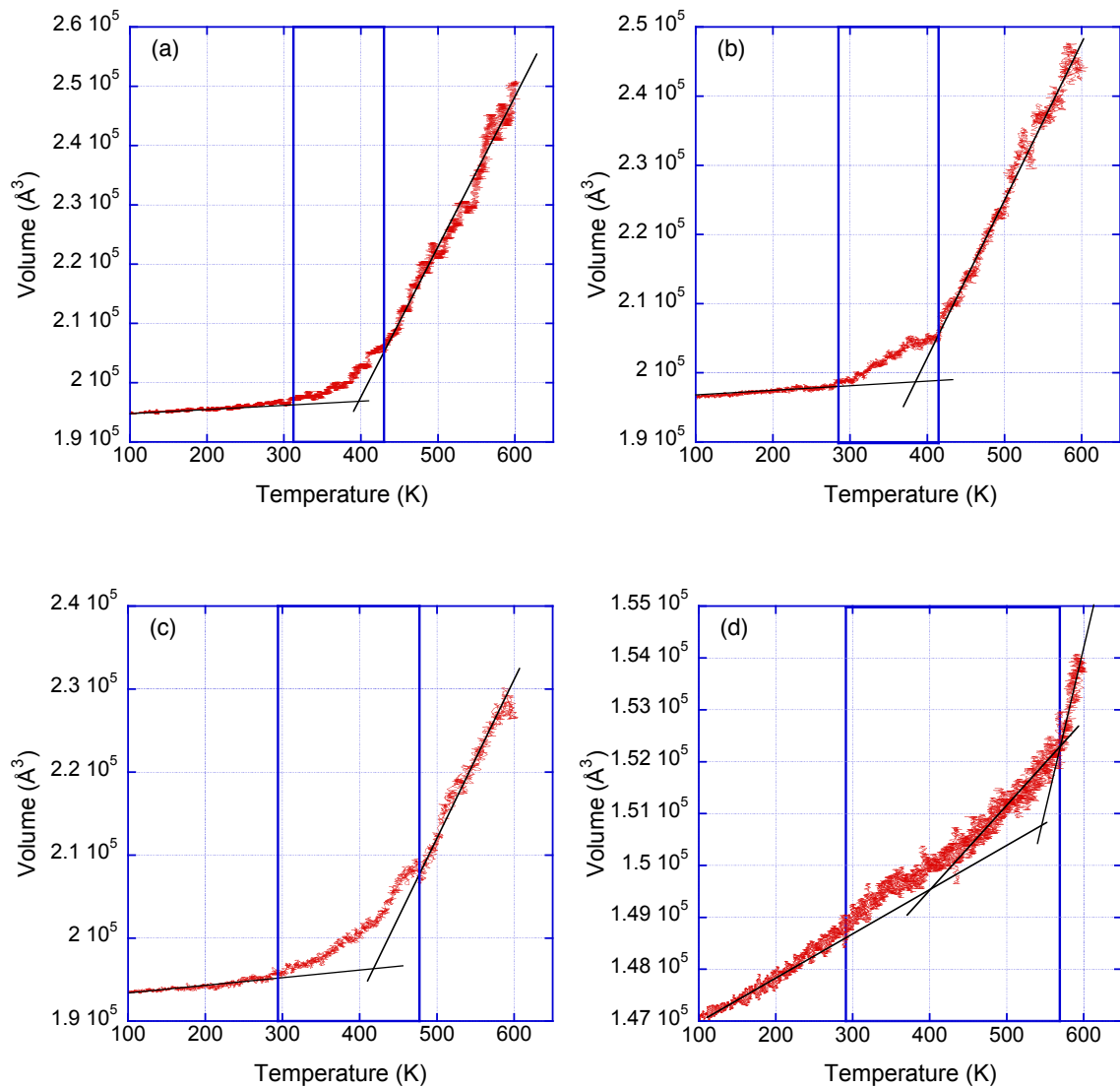
Figure 4.4 Glass transition behavior of PVDF polymeric configurations subject to different applied electric fields during cooling, as apparent from their volume-temperature relationships: (a) $E = 0$, (b) $E = 0.01$ V/Å, (c) $E = 0.1$ V/Å, and (d) $E = 1$ V/Å.

4.4.2 Behavior of PVDF thin films poled at high temperature

Industry practice implies that, in order to achieve decent electro-active responses in PVDF, intensification of β-phase via poling at high temperature is required. We therefore first focused on generating and characterizing poled PVDF structures. In this study, a number of different PVDF systems were prepared by applying electric fields ranging from 10^{-5} to 1 V/Å while annealing at 600 K and during cooling. In all cases do we observe the formation of a net dipole moment, and after removing the applied field, a remnant dipole moment in the PVDF structures. These dipole moments, induced and residual, are roughly commensurate with the applied field for a given quenched structure. Even the changes in thermal conductivity approximately track the field magnitude. However, for fields smaller than about one percent of the breakdown field strength fluctuations in dipole moments and thermal conductivities between PVDF structures quenched from different, independently relaxed starting configurations are larger than the changes as a function of field strength for a single structure. At these small field strengths, structural irregularities, despite the attempt to induce order, seem to overwhelm the induced property changes. For the rest of this discussion we therefore focus on results obtained using field strengths of 0.01 V/Å and above. Four different field strengths are explored here: 0.01, 0.1, 0.5, and 1 V/Å.

After each system reaches a steady state at low temperature, the thermal conductivity calculation is performed while the electric field is still applied. The electric fields are then removed, the polarization of the structure is allowed to relax until steady state is reached again, and the thermal conductivities are calculated once more. Fig. 4.5

shows the comparison of thermal conductivities for systems in the presence and absence of the electric field.
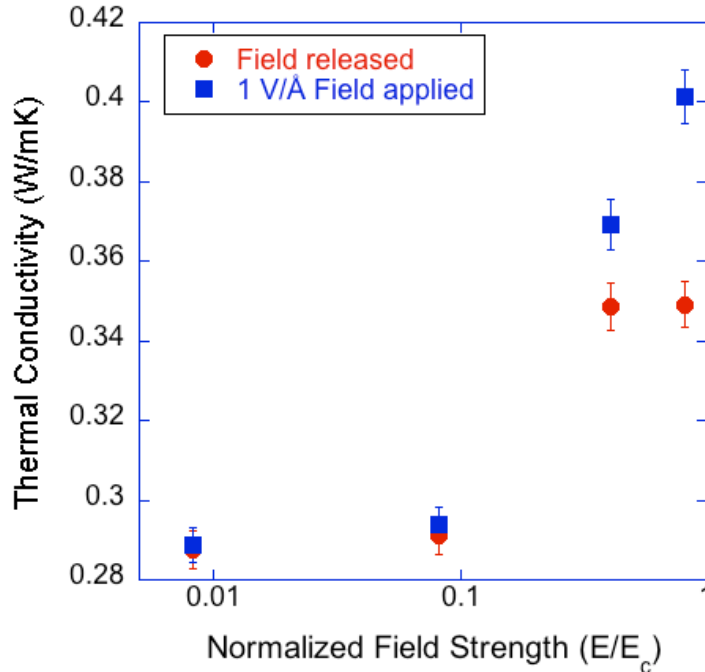
Figure 4.5 Thermal conductivities of poled PVDF layers with and without applied electric field

As Fig. 4.5 reveals, applying electric fields with strengths lower than about 0.1 V/Å has no significant influence on thermal conductivity. Above 0.1 V/Å field strength, we observe a clear increase in thermal conductivity of PVDF. Accordingly, a structure poled at 82% of the breakdown voltage, and with the field applied, exhibits a close to 40% increase in thermal conductivity compared to the unconstrained material. Once the field is removed, the conductivity remains enhanced by still about 20%. Under these conditions the systems possesses a residual dipole moment of 0.8 e·Å per CH_2-CF_2 repeat unit. Apparently, both the direct polarizing influence of the applied field and the

molecular order created during the high temperature poling positively affect the thermal conductivity.

Fig. 4.6 shows the evolution of the net dipole moment vs time for the PVDF layer that had been polarized under a field of 0.5 V/Å, starting at the instant when the electric field is released from the system. We estimate the effective relaxation time constant in our simulations to be between 10 and 100 ps, depending on temperature. The inset of Fig. 4.6 shows the initial stage of the dipole moment relaxation for structures poled under 1 V/Å quenched to different temperatures. Accordingly, the lower this temperature, the stronger the residual dipole moment of the structure, which reveals the thermally activated nature of this process. At high temperatures the effective relaxation time is actually longer than at low temperatures, because thermally energy to activate slower processes has become available, leading to a higher degree of relaxation.
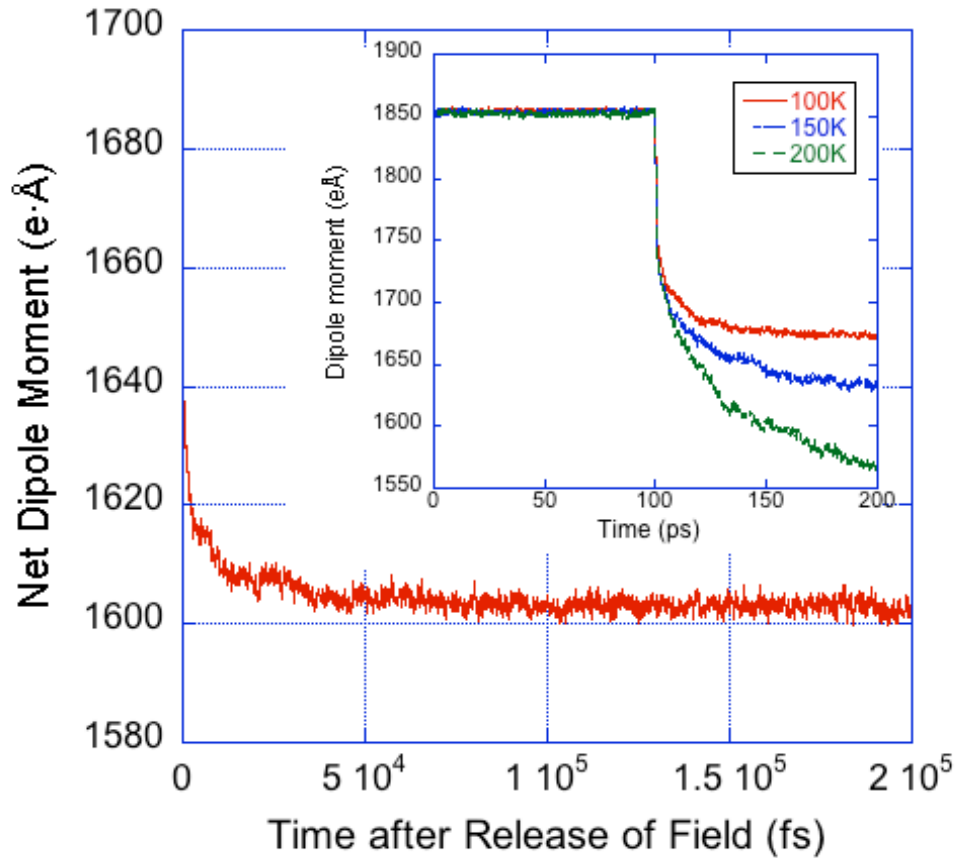
Figure 4.6 Net dipole moment vs time after release of electric field

Conversely, applying an electric field to a poled structure at the low temperature to which it was quenched, in a different direction than the one in which it was originally poled, gradually rotates its residual dipole moment into the direction of the new field. This process, which is illustrated in Fig. 4.7 requires field strengths comparable to those used for the high-temperature poling, but takes vastly longer time. In fact, to reach the saturation level for the dipole moment reorientation was beyond the scope of this study,

but the observed behavior is consistent with the concept that applied electric fields act to overcome activation barriers for structural reorganization.
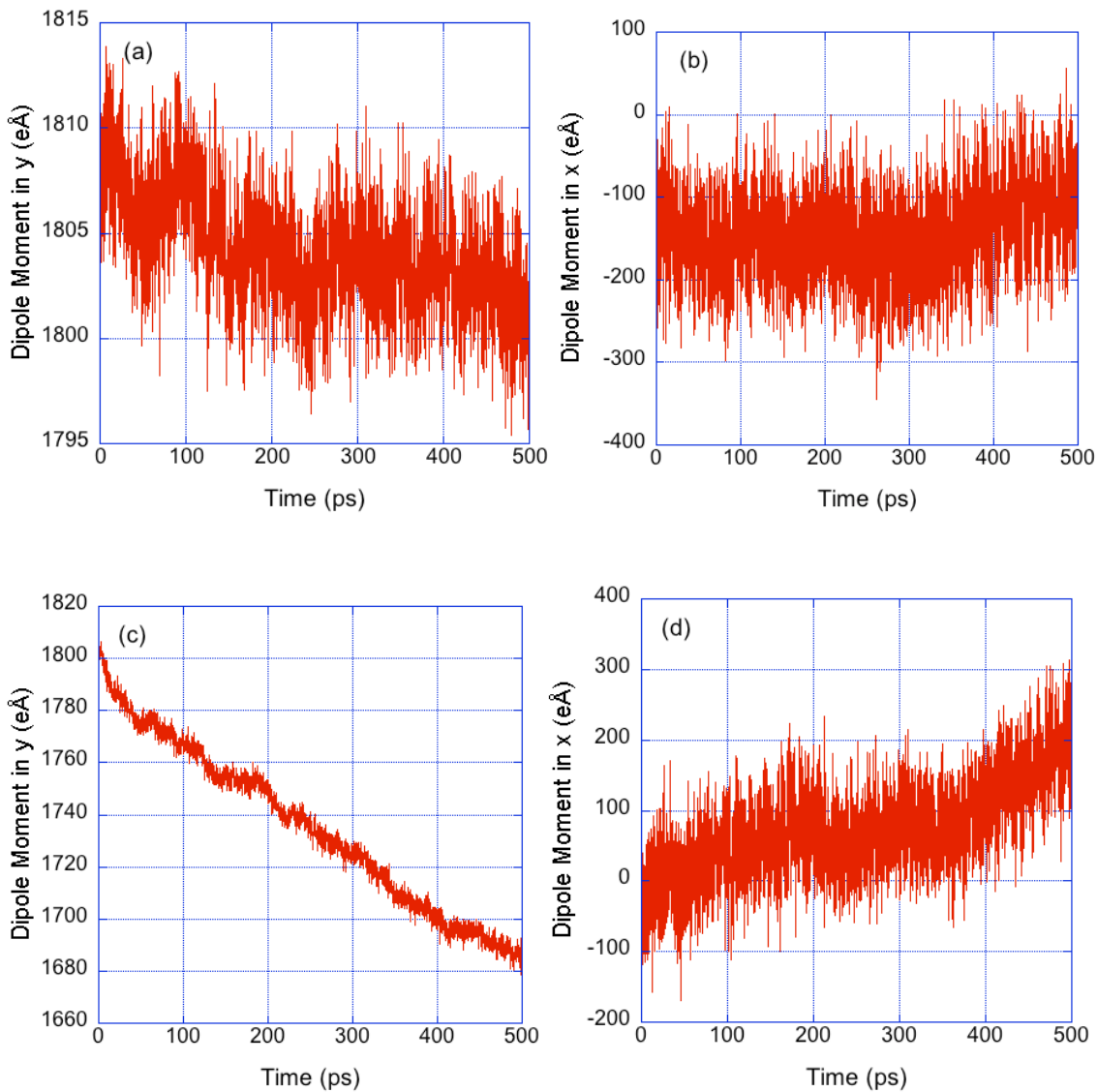
Figure 4.7 System dipole moment after re-polarization in both its original polarized direction (y) and new direction (x) with field strengths of: 0.01 V/Å in (a) and (b); 0.1 V/Å in (c) and (d)

4.4.3 Behavior of disordered PVDF thin films

The fact that significant field induced structural polarization can be achieved at temperatures as low as 100 K in our simulations suggests that the preparatory high-temperature poling of the PVDF films may not be necessary in order to control the thermal transport properties of this material through electric fields. We therefore generate PVDF films without imposing an electric field while the system was thermalized at 600 K, resulting in a disordered PVDF layer with no preferential molecular orientation or ordering. The net dipole moment in any direction is zero within procedural fluctuations. After the disordered PVDF layer was quenched to 100 K, electric fields with strengths of 0.0001, 0.001, 0.01, 0.1, 0.5, and 1 V/Å are applied to the disordered system in direction perpendicular to the film plane. Fig. 4.8 shows the net dipole moment and thickness of the disordered and poled systems in that same direction as a function of the applied field strength.

Consistent with our earlier findings for poled configurations, field strengths below 10% of the breakdown threshold have little effect on the induced dipole moment or film thickness. The applied electric field appears to be too weak to overcome the activation barrier required for PVDF molecules to reorient. Although we observe a film thickness reduction of about 7% between applying a field of 10^{-4}-times the critical value an no field applied, after that the film thickness remains essentially constant up to one tenth of the breakdown field magnitude. When the applied electric field strength exceeds 0.1 V/Å, the thickness of the PVDF film decreases and the dipole moment per CH_2-CF_2 repeat unit increases rapidly. These results indicate that the PVDF molecules reorient in direction of

the applied electric field, forming an ordered PVDF layer. The stronger the electric field strength, the higher level of ordering, as reflected in the higher per unit volume dipole moment.
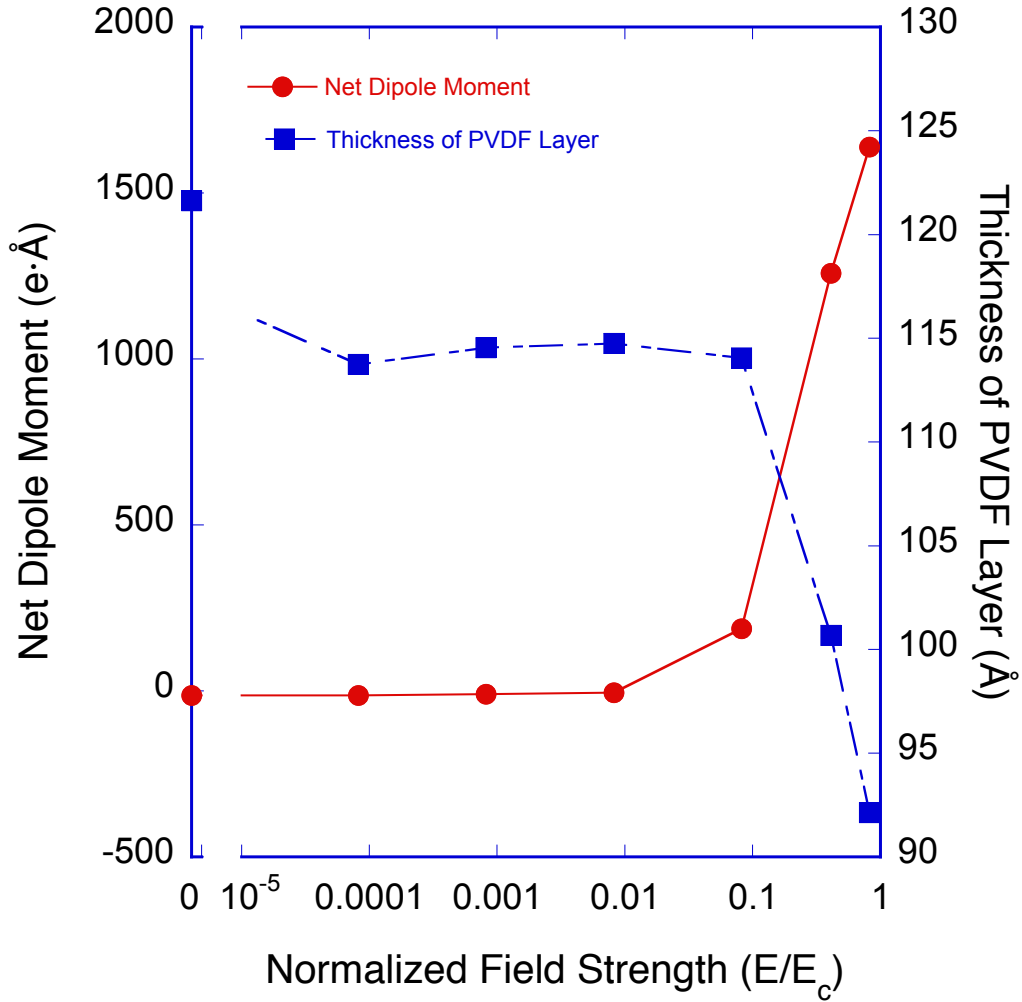
Figure 4.8 Net dipole moment in the direction of applied electric field and thickness of PVDF layer as a function of applied field strength

Thermal conductivity calculations are then performed on both the disordered PVDF films and those subject to applied electric fields using the Müller-Plathe algorithm[24]. The results are presented in Fig. 4.9. We again observe a significant in

thermal conductivity with the magnitude of the applied electric field. The relative change in conductivity is about 34% for the highest field strength, almost as much as for the poled structures. Given the influence of random structural defects, this conductivity enhancement may indeed be quite comparable to that achieved in poled PVDF.
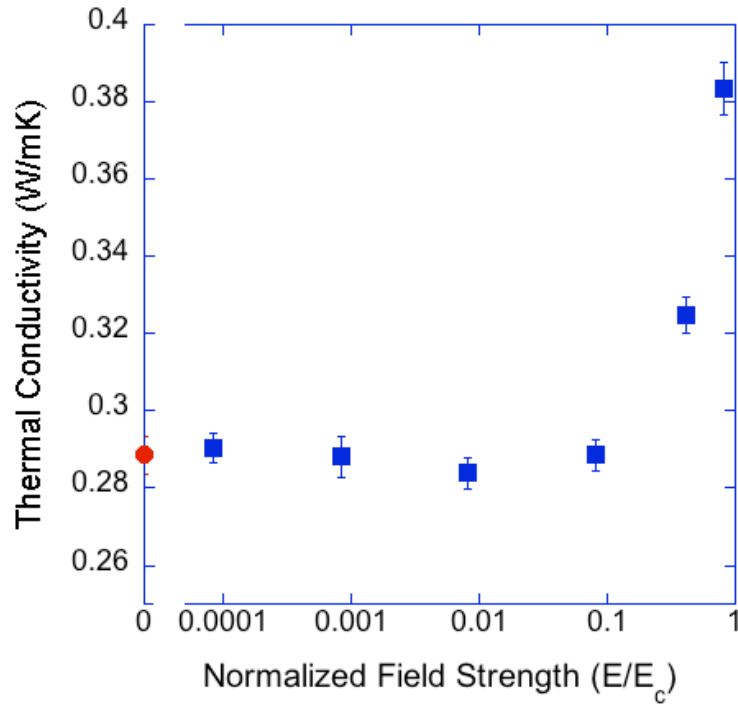
Figure 4.9 Müller-Plathe thermal conductivity calculation results for PVDF layers with different applied electric field strengths

4.4.4 Vibrational density of states (VDOS)

To better understand the reason for the increase in thermal conductivity for PVDF with applied electric field, we computed the vibrational density of states (VDOS), $D(w)$, for systems with and without applied electric field. $D(w)$, is calculated via Fourier transform of the velocity autocorrelation function (VACF), according to

$$D(\omega) = \mathrm{Re}\left(\int_0^\infty \left\langle \frac{\mathbf{v}_j(t)\cdot\mathbf{v}_j(0)}{\left|\mathbf{v}_j(0)\right|^2}\right\rangle e^{i\omega t}\,dt\right) \qquad (4.4)$$

where ω is the frequency and $\mathbf{v}_j(t)$ is the velocity of atom j at time t. The angular brackets indicate both the time and ensemble average of this quantity. Fig. 4.10(a) shows the VDOS calculation results for both the random system and poled system under 1 V/Å field strength.
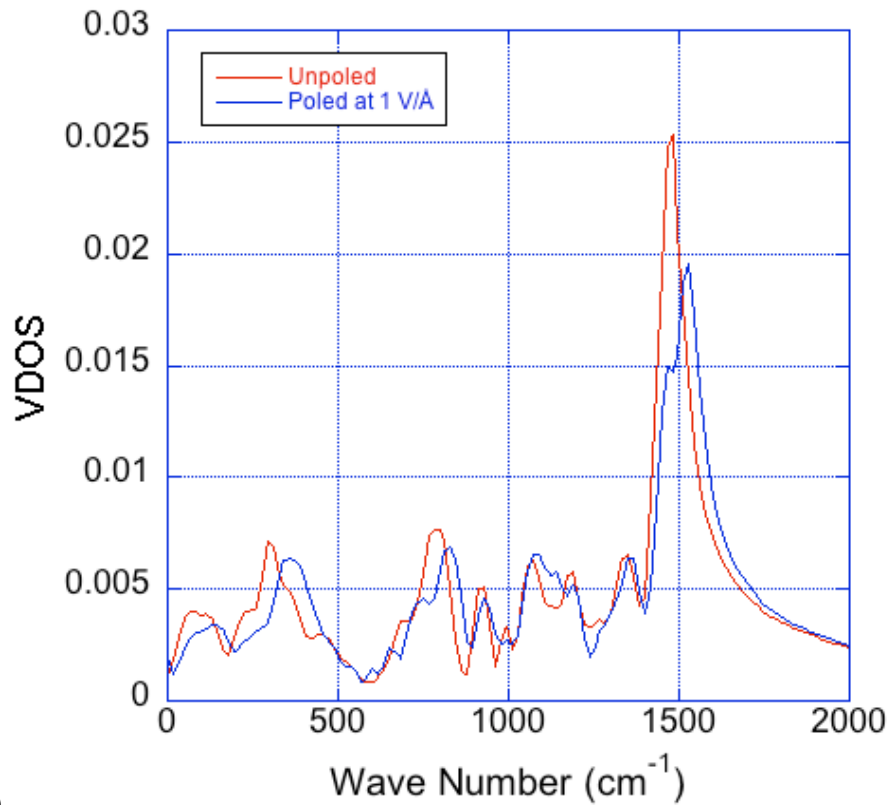
(a)
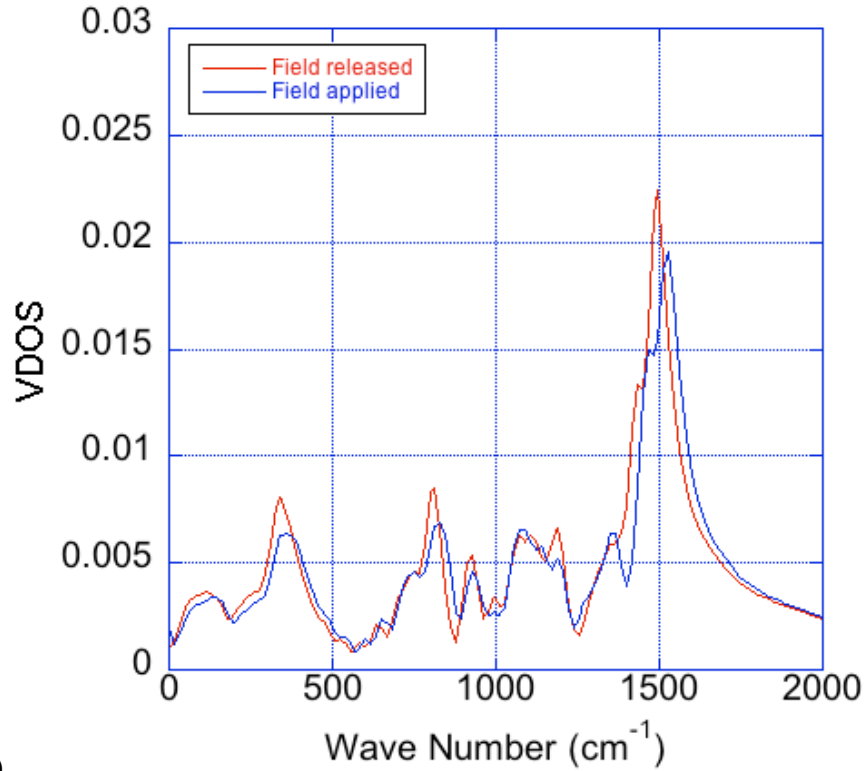
(b)

Figure 4.10 Comparison of phonon DOS for (a) PVDF layers prepared without electric field and subject a field of 1 V/Å, (b) PVDF layers poled at 1 V/Å and the same system with field released.

For a number of spectral features in the VDOS we observe a noticeable shift towards higher frequencies upon applying the electric field is applied to the disordered system, especially in the low-frequency regime (below 500 cm^{-1}), where acoustic phonon modes are located. Higher frequency in acoustic vibrational modes translates into a higher sound velocity, and enhances the phonon contribution to the thermal conductivity. The highest-frequency peak, typically associated with vibrational modes involving the motion of nearest neighbors, and therefore directly reflects the stiffness of interatomic bonds, splits upon applying the field. This indicates that the distortion of the molecular

structure caused by the external electric field pushes the configuration into a region of energy landscape that exhibits sharper curvature. All the ways that the applied field affects the VDOS spectrum supports the notion that bonding in the PVDF structure becomes stiffer under the influence of a strong electric field, and this essentially raises the phonon contribution to the thermal conductivity. Our finding is consistent with that of Shen et al., who report increased thermal conductance due to stiffer bonds.[3] Fig. 4.10(b), compares the VDOS spectrum of the system poled at high temperature and quenched with the field applied to that of the same system after the field has been released. When releasing the field, the VDOS spectral features shift towards the lower frequency, but not as far as to coincide with the unpoled configuration. This partial decrease in structural stiffness is consistent with the decrease in thermal conductivity, observed in Fig. 4.5. The highest-frequency peak still retains the split peak feature, first observed in the poled system, and attributed to local bonding structures. This indicates that even after releasing the field, some interatomic bonds remain in a constrained configuration, which accounts for the strong residual dipole moment in the system. The electric field resulting from this dipole moment may therefore be considered as responsible for the residual enhancement of the thermal conductivity.

4.4.5 Thermal transport across the PVDF-gold interface

In our previous chapters, we have demonstrated that the interfacial adhesive strength dominates thermal boundary conductance across interfaces between weakly bonded dissimilar materials, such as are formed when organic materials are deposited onto inorganic ones.[2] Electrostatic forces acting across such an interface can enhance the

adhesive strength. In this section we describe the possibility of controlling thermal boundary conductance (TBC) across an interface between metal and the polarizable PVDF polymer, via an applied electric field. To this end we sandwich a system of 250 PVDF chains, described earlier, in between gold slabs in the fashion of a Au-PVDF-Au-PVDF periodic structure. The PVDF molecules are melted and thermalized at 600 K to randomize the structure, before it is cooled to 100 K. After reaching steady state the PVDF layer is then placed in contact with the gold slabs on top and bottom. In this case, the electric field is applied to the system by charging the gold atoms, positively in one slab and negatively in the next, which is why the simulation box contains two gold and PVDF layers. The atomic charge is set to be ±0.01 electron unit charges. The dimension of the simulated system is 40 by 40 by 270 Å and periodic boundary condition are applied in all three dimensions. The system is essentially a parallel capacitor with PVDF as the dielectric material. The effective electric field across the PVDF layer, and interfaces, is calculated to be 0.7 V/Å or 0.57 E_c. Thermal transport properties are again determined using the Müller-Plathe method.[24] In this procedure, one metal layer contains a heat source and the other a sink. Kinetic energy is artificially transferred from the heat sink to the heat source and the energy flows back from source to sink layer by heat conduction. Over time this results in a steady-state temperature gradient and thermal transport coefficients can be calculated from temperature profile and heat flux magnitude. Fig. 4.11 shows a comparison of the thermal transport calculation results for a charged system and a neutral system.
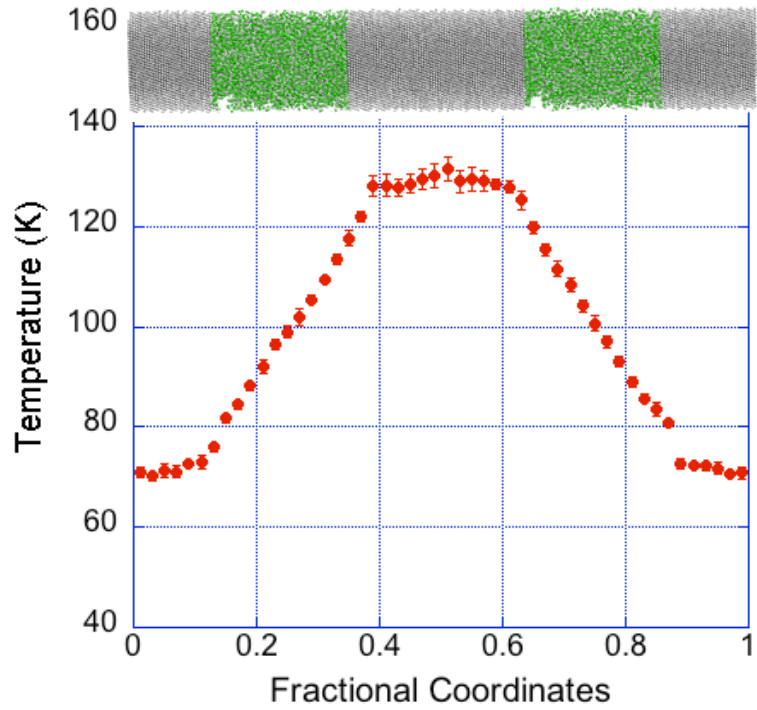
(a)
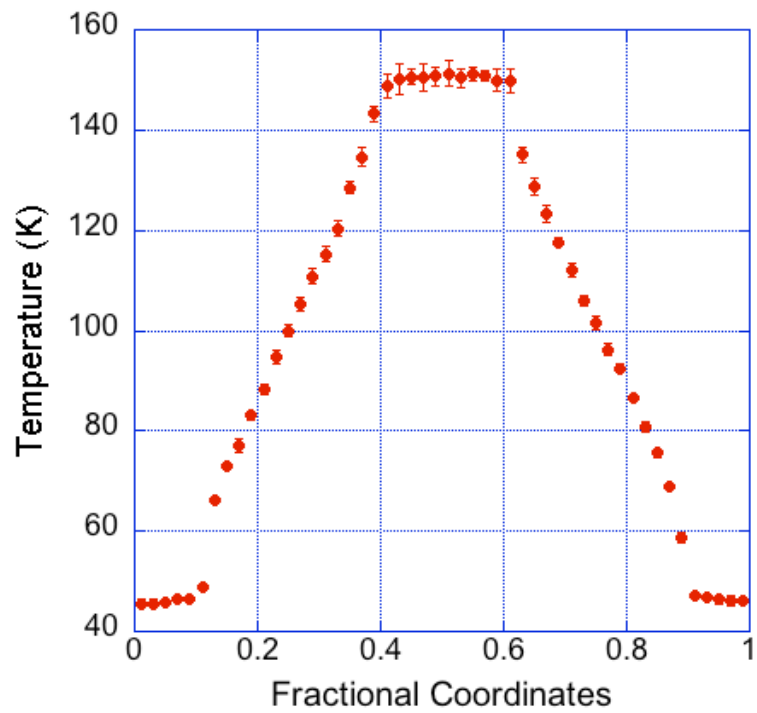
(b)

Figure 4.11 Temperature profile for PVDF junctions (a) with charged gold substrate (b)

neutral gold substrate

The steady-state temperature profile reveals two pieces of information; they can be derived from the temperature gradient across the PVDF layers and the temperature discontinuities, ΔT, at the interfaces. The calculated heat flux divided by the average slope in the temperature profile in PVDF yields the thermal conductivity of this material. Similarly, the heat flux divided by ΔT corresponds to the TBC of the interface. From our simulations we see that the charged system shows distinctly different characteristics than the neutral system. ΔT at the PVDF-gold interface is reduced significantly when the metal is charged, i.e., when an electric field acts on the interface, reflecting a higher TBC. Under the influence of this field, PVDF molecules polarize and reorient, drawing on average hydrogen and carbon atoms with partial positive charges closer to the negatively charged gold substrate, and vice versa, fluorine and carbon atoms with partial negative charges closer to the positively charged gold substrate. The resulting Coulomb interactions between metal and polymer, superimpose onto the weak van der Waals bonding interactions, and strengthen the adhesion. As a result, the TBC at the interface increases from 1.51 ± 0.05 GW/m^{2}K to 9.81 ± 5.13 GW/m^{2}K. Meanwhile, due to the stiffening effect of electric field, the thermal conductivity of PVDF layer is increased from 0.267 W/mK to 0.396 W/mK as expected. Therefore the net effective thermal transport of the bilayer system with charged substrates is 0.349 W/mK as compared to 0.186 W/mK for the neutral system. This gain in effective thermal conductivity can be even more amplified by reducing the PVDF layer thickness.

4.5   Summary and Conclusion

Using non-equilibrium molecular dynamics simulations, we have studied how PVDF films respond to externally applied electric fields of different strengths in terms of their thermal transport properties. We found that a weak electric field ($< 0.1 \, E_c$) has little impact on the thermal conductivity of PVDF layers because it does not offer enough energy to overcome energy barrier for structural rearrangements that lead to significant polarization of the polymer. For PVDF films poled under strong electric field, the net dipole moment in the system increases with increasing applied electric field, indicating that PVDF molecules reorient to align with the applied field. Under the influence of strong electric fields thermal transport properties improve significantly, which can be attributed to two mechanisms: (i) charge polarization in the structure causes the interatomic bonds to stiffen, which raises the phonon contribution to the thermal conductivity; (ii) the adhesive strength at the interfaces between PVDF and a charge metallic substrate is enhanced due to the additional Coulomb interactions between the substrate and the polarized PVDF molecules, which results in an increase of the thermal boundary conductance. Our simulations provide proof of concept that by applying electric fields one can control the thermal transport properties in materials systems containing electro-active polymer.

4.6   References

1.   Hu, M., Keblinski, P., Wang, J.-S. & Raravikar, N. Interfacial thermal conductance between silicon and a vertical carbon nanotube. *Journal of Applied Physics* **104**, 083503-083503 (2008).
2.   Jin, Y., Shao, C., Kieffer, J., Pipe, K. P. & Shtein, M. Origins of thermal boundary conductance of interfaces involving organic semiconductors. *Journal of Applied Physics* **112**, 093503 (2012).
3.   Shen, M., Evans, W. J., Cahill, D. & Keblinski, P. Bonding and pressure-tunable interfacial thermal conductance. *Physical Review B* **84**, 195432 (2011).
4.   Stevens, R. J., Zhigilei, L. V. & Norris, P. M. Effects of temperature and disorder on thermal boundary conductance at solid–solid interfaces: Nonequilibrium molecular dynamics simulations. *International Journal of Heat and Mass Transfer* **50**, 3977-3989 (2007).
5.   Eberle, G., Schmidt, H. & Eisenmenger, W. Piezoelectric polymer electrets. *Dielectrics and Electrical Insulation, IEEE Transactions on* **3**, 624-646 (1996).
6.   Hasegawa, R., Takahashi, Y., Chatani, Y. & Tadokoro, H. Crystal structures of three crystalline forms of poly (vinylidene fluoride). *Polymer Journal* **3**, 600-610 (1972).
7.   Lando, J. B., Olf, H. G. & Peterlin, A. Nuclear magnetic resonance and x‑ray determination of the structure of poly (vinylidene fluoride). *Journal of Polymer Science Part A‑1: Polymer Chemistry* **4**, 941-951 (1966).
8.   Weinhold, S., Litt, M. H. & Lando, J. B. The crystal structure of the γ phase of poly (vinylidene fluoride). *Macromolecules* **13**, 1178-1183 (1980).
9.   Chen, S., Yao, K., Tay, F. E. H. & Liow, C. L. Ferroelectric poly (vinylidene fluoride) thin films on Si substrate with the β phase promoted by hydrated magnesium nitrate. *Journal of Applied Physics* **102**, 104108-104108 (2007).
10.   He, X. & Yao, K. Crystallization mechanism and piezoelectric properties of solution-derived ferroelectric poly (vinylidene fluoride) thin films. *Applied physics letters* **89**, 112909-112909 (2006).
11.   Salimi, A. & Yousefi, A. A. Analysis Method: FTIR studies of β-phase crystal formation in stretched PVDF films. *Polymer Testing* **22**, 699-704 (2003).
12.   Salimi, A. & Yousefi, A. A. Conformational changes and phase transformation mechanisms in PVDF solution‑cast films. *Journal of Polymer Science Part B: Polymer Physics* **42**, 3487-3495 (2004).
13.   Zeng, F.-, Sun, Y., Zhou, Y. & Li, Q.-. A molecular dynamics simulation study to investigate the elastic properties of PVDF and POSS nanocomposites. *Modelling and Simulation in Materials Science and Engineering* **19**, 025005 (2011).
14.   Bystrov, V. S. Molecular modeling and molecular dynamics simulation of the polarization switching phenomena in the ferroelectric polymers PVDF at the nanoscale. *Physica B: Condensed Matter* (2014).
15.   Sun, H. COMPASS: An ab initio force-field optimized for condensed-phase applications overview with details on alkane and benzene compounds. *The Journal*

of Physical Chemistry B **102**, 7338-7364 (1998).

16. Ma, X. & Shrotriya, P. Molecular Dynamics simulation of electrical field induced conformational transition and associated frictional performance of monomolecular films. *Journal of Physics D: Applied Physics* **45**, 375306 (2012).

17. Zhou, X. et al. Electrical breakdown and ultrahigh electrical energy density in poly (vinylidene fluoride-hexafluoropropylene) copolymer. *Applied Physics Letters* **94**, 162901-162901 (2009).

18. Stark, K. H. & Garton, C. G. Electric strength of irradiated polythene. (1955).

19. Dissado, L. A. & Fothergill, J. C. Electrical Deeradation and Breakdown in Polsmers ed GC. (1992).

20. Kao, K. C. *Dielectric phenomena in solids* (Access Online via Elsevier, 2004).

21. O'Dwyer, J. J. *The theory of dielectric breakdown of solids* (Clarendon Press Oxford, 1964).

22. Center, N. C. 5TH INTERNATIONAL SYMPOSIUM ON MICRO MACHINE AND HUMAN SCIENCE. *ieeexplore.ieee.org* (1994).

23. Tomohiro, S., Matsukawa, M., Otani, T. & Ohtori, N. Brillouin scattering study on the opto-acoustic properties of thin piezoelectric polymer films. *JAPANESE JOURNAL OF APPLIED PHYSICS PART 1-REGULAR PAPERS SHORT NOTES & REVIEW PAPERS* **43**, 2916-2919 (2004).

24. Müller-Plathe, F. A simple nonequilibrium molecular dynamics method for calculating the thermal conductivity. *The Journal of chemical physics* **106**, 6082 (1997).

Chapter 5 Summary and outlook

5.1 Summary

In this work, we used computational methods to understand the heat transfer process at interface of dissimilar materials, developed a new full atomistic force field that successfully predicts properties of CuPc material, identified most significant factor influencing heat transfer at CuPc-metal interfaces, and presented a new method to actively control thermal transport properties of PVDF piezoelectric polymers.

In Chapter 2, The Hybrid-COMPASS force field has been expanded to accurately simulate CuPc isolated molecules, as well as crystalline and amorphous condensed phases. The structure of the isolated CuPc molecule is in good agreement with experimental observations. The MD simulations also predict α- and β-form CuPc crystal structures at different temperatures with reasonable accuracy when compared with experimental measurements. The vibrational density of states calculated from MD simulation also agrees well with both experimental and theoretical studies of normal mode frequencies of CuPc molecule. Based on this new force field, we analyzed the thermal conduction mechanisms in amorphous and crystalline CuPc using the Green-Kubo formalism. Comparing with experimental measurements we observe reasonable agreement for amorphous samples, and we conclude that the crystalline samples consist

of nano-domains isolated from each other by significant amounts of amorphous domain boundaries, possibly exceeding half the sample volume.

In Chapter 3, metal systems were first explored to analyze the effect of different properties such as density, elastic modulus, acoustic impedance, and velocity of sound etc. The systems were structurally congruent and virtual interfaces were created by the mismatch of various properties. It is found that the thermal boundary resistance still exists even when the acoustic impedance is matched, while diminishes when the velocity of sound is matched. This contradicts predictions from AMM and shows that AMM is not complete in predicting thermal boundary resistance. For the CuPc-metal interface, we first fixed the interfacial bonding strength and only controlled the density and elastic modulus of the metal substrate in CuPc-metal systems, MD calculations of TBC predicted the same trend as the AMM results. However, eliminating the effect of interfacial bonding strength would result in false predictions both from MD and AMM calculations: CuPc-Ag would have a larger TBC than CuPc-Au interface while in experiment, the opposite trend was observed. This clearly indicated that interfacial bonding strength should be the dominant factor on the TBC at CuPc-metal interfaces. Interfacial bonding strength was controlled for different CuPc-metal (Ag, Au, Al) systems and TBC with different bonding strength was calculated from MD simulations. For weak bonding, a clear log-linear relationship was observed between work of adhesion and TBC at CuPc-metal interfaces. For strong bonding, TBC values saturated as expected. The work of adhesion for different CuPc-metal systems in experiment were also estimated from MD simulations: CuPc-Ag ~ 0.046 J/m2, CuPc-Au ~ 0.095 J/m2, CuPc-Al ~ 0.439 J/m2, which agreed with peel-off experiment results very well. From

this we demonstrated strong correlation between interfacial bonding strength and TBC at weakly bonded organic-inorganic interfaces.

In Chapter 4, thermal transport properties of piezoelectric polymer PVDF are studies. Using non-equilibrium molecular dynamics simulations, we have studied how PVDF films response to externally applied electric fields with different strengths. We found that a weak electric field (< 0.1 Ec) has little impact on the thermal conductivity of PVDF layers because it does not offer enough energy to overcome energy barrier between different configurations. For PVDF films poled under strong electric field, we found the net dipole moment in the system increases with increasing applied electric field indicating PVDF molecules are better aligned to the field direction under stronger field. Thermal conductivity calculation results show that the conductivity increases with the increasing electric field. Phonon DOS calculations show that applying strong electric field would enhance intermolecular bonding. This would make the PVDF film stiffer and thus thermal conductivity is increased. Upon releasing the electric field from the poled films, we observed a decrease in net dipole moment due to the temperature effect. We also found strong remnant dipole moment in the films as expected from experiments.{Eberle et al., 1996, #69072} Such decrease in net dipole moment and local electric field leads to a decrease in thermal conductivity. The change in thermal conductivity for PVDF films shows promising future for active control of thermal conductivity in many applications involving organic materials.

Overall, this thesis provides useful insights to both passive and active control to heat transfer at materials' interfaces and offers new directions for the development of thermal management in many applications.

5.2　Future work and outlook

The computational power of simulation allows detailed control of every property of the material and offers solutions to isolating single factors from complex problems. However, such power does not overshadow the importance of experiments and even sophisticated MD modeling cannot replace experiments, which are the benchmarks for every theoretical prediction.

One possible extension of this work would be the experimental validation of the predictions made in Chapter 4 on the active control of thermal transport properties of PVDF. Since the time steps in MD simulations do not reflect the true relaxation time needed in actual experiments, it is necessary to study the response time for the active control of thermal transport with external electric field control. Also in MD simulation, the atomic partial charges are fixed and do not polarize properly with the applied electric field. Therefore, further detailed analysis of the polarization response of PVDF to applied electric field strength is needed in experiments. With these supplemental experiment researches, the study of active control of thermal transport properties of PVDF using electric field is then complete. And the era of active control of heat transfer even in the nano-scale devices shall come to reality.

Appendix A   MATLAB code for multivariable

optimization

```
Refer Fig. 2.1 for atom labeling

% Load necessary data files
load data.mat;
load C_coords.mat;
load N_coords.mat;

%read dx dy dz from file
%x = data(:,1);
%y = data(:,2);
%z = data(:,3);
d = data(:,1:3);
E = data(:,4);
E0= -3307.54079603;
delE = (E-E0)*23.06;

%surrounding N,C coords
%row: 1-8 --> N33-N40
%row: 9-24 -> C1-C16
for i = 1:8,
    n(i,:) = C_coords(i,:);
end
for i = 1:16,
    c(i,:) = N_coords(i,:);
end

b0 = 1.954;
bcn = 1.375;      %bond length of C-N(connecting Cu)
ang0 = 125.8855/180.000*pi();   %Equilibrium angle of C-N-Cu
ang1 = pi()/2;                  %Equilibrium angle of 4 N-Cu-N

%for each random walk out of f configurations

for f = 1:1000,

% Calculate 4 surrounding Cu-N bond lengths
% 1-4 corresponds to N37 - N40
    for i = 1:4,
        y(f,i) = sqrt(dot((d(f,:)-n(i+4,:)),(d(f,:)-n(i+4,:))));
    end

% Calculate 12 surrounding angles
% 1-8 --> C-N-Cu
% 9-12 -> N-Cu-N
    for i = 1:4,
```

```
        y(f,i+4) = acos(dot((c(i,:)-n(i+4,:)),(d(f,:)-
n(i+4,:))))/(bcn*y(f,i)));
        y(f,i+8) = acos(dot((c(i+4,:)-n(i+4,:)),(d(f,:)-
n(i+4,:))))/(bcn*y(f,i)));
    end

    y(f,13) = acos(dot((n(5,:)-d(f,:)),(n(6,:)-
d(f,:))))/(y(f,1)*y(f,2)));        %N37-Cu-N38
    y(f,14) = acos(dot((n(7,:)-d(f,:)),(n(8,:)-
d(f,:))))/(y(f,3)*y(f,4)));        %N39-Cu-N40
    y(f,15) = acos(dot((n(5,:)-d(f,:)),(n(7,:)-
d(f,:))))/(y(f,1)*y(f,3)));        %N37-Cu-N39
    y(f,16) = acos(dot((n(6,:)-d(f,:)),(n(8,:)-
d(f,:))))/(y(f,2)*y(f,4)));        %N38-Cu-N40


% Calculate 32 surrounding dihedrals y(17) - y(48)
% Cu57-N37-C1-C9, Cu57-N38-C2-C10, Cu57-N39-C3-C11, Cu57-N40-C4-C12
    for i = 1:4,
        v_AB = n(i+4,:)-d(f,:);
        v_BC = c(i,:)-n(i+4,:);
        v_CD = c(i+8,:)-c(i,:);

        length_AB = sqrt(dot(v_AB,v_AB));
        length_BC = sqrt(dot(v_BC,v_BC));
        length_CD = sqrt(dot(v_CD,v_CD));

        sin_ABC = sin(acos(dot(-v_AB,v_BC)/(length_AB*length_BC)));
        sin_BCD = sin(acos(dot(-v_BC,v_CD)/(length_BC*length_CD)));

        n_ABC = cross(v_AB,v_BC)/(length_AB*length_BC*sin_ABC);
        n_BCD = cross(v_BC,v_CD)/(length_BC*length_CD*sin_BCD);

        y(f,16+i) = acos(dot(n_ABC,n_BCD));

    end

% Cu57-N37-C5-C13, Cu57-N38-C6-C14, Cu57-N39-C7-C15, Cu57-N40-C8-C16
    for i = 1:4,
        v_AB = n(i+4,:)-d(f,:);
        v_BC = c(i+4,:)-n(i+4,:);
        v_CD = c(i+12,:)-c(i+4,:);

        length_AB = sqrt(dot(v_AB,v_AB));
        length_BC = sqrt(dot(v_BC,v_BC));
        length_CD = sqrt(dot(v_CD,v_CD));

        sin_ABC = sin(acos(dot(-v_AB,v_BC)/(length_AB*length_BC)));
        sin_BCD = sin(acos(dot(-v_BC,v_CD)/(length_BC*length_CD)));

        n_ABC = cross(v_AB,v_BC)/(length_AB*length_BC*sin_ABC);
        n_BCD = cross(v_BC,v_CD)/(length_BC*length_CD*sin_BCD);

        y(f,20+i) = acos(dot(n_ABC,n_BCD));
```

```matlab
    end

% Cu57-N37-C5-N35, Cu57-N37-C1-N33
    for i = 1:2,
        v_AB = n(5,:)-d(f,:);
        v_BC = c(4*i-3,:)-n(5,:);
        v_CD = n(2*i-1,:)-c(4*i-3,:);

        length_AB = sqrt(dot(v_AB,v_AB));
        length_BC = sqrt(dot(v_BC,v_BC));
        length_CD = sqrt(dot(v_CD,v_CD));

        sin_ABC = sin(acos(dot(-v_AB,v_BC)/(length_AB*length_BC)));
        sin_BCD = sin(acos(dot(-v_BC,v_CD)/(length_BC*length_CD)));

        n_ABC = cross(v_AB,v_BC)/(length_AB*length_BC*sin_ABC);
        n_BCD = cross(v_BC,v_CD)/(length_BC*length_CD*sin_BCD);

        y(f,24+i) = acos(dot(n_ABC,n_BCD));

    end

% Cu57-N38-C2-N34, Cu57-N38-C6-N33
    for i = 1:2,
        v_AB = n(6,:)-d(f,:);
        v_BC = c(4*i-2,:)-n(6,:);
        v_CD = n(3-i,:)-c(4*i-2,:);

        length_AB = sqrt(dot(v_AB,v_AB));
        length_BC = sqrt(dot(v_BC,v_BC));
        length_CD = sqrt(dot(v_CD,v_CD));

        sin_ABC = sin(acos(dot(-v_AB,v_BC)/(length_AB*length_BC)));
        sin_BCD = sin(acos(dot(-v_BC,v_CD)/(length_BC*length_CD)));

        n_ABC = cross(v_AB,v_BC)/(length_AB*length_BC*sin_ABC);
        n_BCD = cross(v_BC,v_CD)/(length_BC*length_CD*sin_BCD);

        y(f,26+i) = acos(dot(n_ABC,n_BCD));

    end

% Cu57-N39-C3-N35, Cu57-N39-C7-N36
    for i = 1:2,
        v_AB = n(7,:)-d(f,:);
        v_BC = c(4*i-1,:)-n(7,:);
        v_CD = n(2+i,:)-c(4*i-1,:);

        length_AB = sqrt(dot(v_AB,v_AB));
        length_BC = sqrt(dot(v_BC,v_BC));
        length_CD = sqrt(dot(v_CD,v_CD));

        sin_ABC = sin(acos(dot(-v_AB,v_BC)/(length_AB*length_BC)));
```

```matlab
        sin_BCD = sin(acos(dot(-v_BC,v_CD)/(length_BC*length_CD)));

        n_ABC = cross(v_AB,v_BC)/(length_AB*length_BC*sin_ABC);
        n_BCD = cross(v_BC,v_CD)/(length_BC*length_CD*sin_BCD);

        y(f,28+i) = acos(dot(n_ABC,n_BCD));

    end

% Cu57-N40-C4-N36, Cu57-N40-C8-N34
    for i = 1:2,
        v_AB = n(8,:)-d(f,:);
        v_BC = c(4*i,:)-n(8,:);
        v_CD = n(6-2*i,:)-c(4*i,:);

        length_AB = sqrt(dot(v_AB,v_AB));
        length_BC = sqrt(dot(v_BC,v_BC));
        length_CD = sqrt(dot(v_CD,v_CD));

        sin_ABC = sin(acos(dot(-v_AB,v_BC)/(length_AB*length_BC)));
        sin_BCD = sin(acos(dot(-v_BC,v_CD)/(length_BC*length_CD)));

        n_ABC = cross(v_AB,v_BC)/(length_AB*length_BC*sin_ABC);
        n_BCD = cross(v_BC,v_CD)/(length_BC*length_CD*sin_BCD);

        y(f,30+i) = acos(dot(n_ABC,n_BCD));

    end

% N38-Cu57-N37-C1, N39-Cu57-N37-C1
    for i = 1:2,
        v_AB = d(f,:)-n(i+5,:);
        v_BC = n(5,:)-d(f,:);
        v_CD = c(1,:)-n(5,:);

        length_AB = sqrt(dot(v_AB,v_AB));
        length_BC = sqrt(dot(v_BC,v_BC));
        length_CD = sqrt(dot(v_CD,v_CD));

        sin_ABC = sin(acos(dot(-v_AB,v_BC)/(length_AB*length_BC)));
        sin_BCD = sin(acos(dot(-v_BC,v_CD)/(length_BC*length_CD)));

        n_ABC = cross(v_AB,v_BC)/(length_AB*length_BC*sin_ABC);
        n_BCD = cross(v_BC,v_CD)/(length_BC*length_CD*sin_BCD);

        y(f,32+i) = acos(dot(n_ABC,n_BCD));

    end

% N38-Cu57-N37-C5, N39-Cu57-N37-C5
    for i = 1:2,
        v_AB = d(f,:)-n(i+5,:);
        v_BC = n(5,:)-d(f,:);
        v_CD = c(5,:)-n(5,:);
```

```
        length_AB = sqrt(dot(v_AB,v_AB));
        length_BC = sqrt(dot(v_BC,v_BC));
        length_CD = sqrt(dot(v_CD,v_CD));

        sin_ABC = sin(acos(dot(-v_AB,v_BC)/(length_AB*length_BC)));
        sin_BCD = sin(acos(dot(-v_BC,v_CD)/(length_BC*length_CD)));

        n_ABC = cross(v_AB,v_BC)/(length_AB*length_BC*sin_ABC);
        n_BCD = cross(v_BC,v_CD)/(length_BC*length_CD*sin_BCD);

        y(f,34+i) = acos(dot(n_ABC,n_BCD));

    end

% N37-Cu57-N38-C2, N40-Cu57-N38-C2
    for i = 1:2,
        v_AB = d(f,:)-n(3*i+2,:);
        v_BC = n(6,:)-d(f,:);
        v_CD = c(2,:)-n(6,:);

        length_AB = sqrt(dot(v_AB,v_AB));
        length_BC = sqrt(dot(v_BC,v_BC));
        length_CD = sqrt(dot(v_CD,v_CD));

        sin_ABC = sin(acos(dot(-v_AB,v_BC)/(length_AB*length_BC)));
        sin_BCD = sin(acos(dot(-v_BC,v_CD)/(length_BC*length_CD)));

        n_ABC = cross(v_AB,v_BC)/(length_AB*length_BC*sin_ABC);
        n_BCD = cross(v_BC,v_CD)/(length_BC*length_CD*sin_BCD);

        y(f,36+i) = acos(dot(n_ABC,n_BCD));

    end

% N37-Cu57-N38-C6, N40-Cu57-N38-C6
    for i = 1:2,
        v_AB = d(f,:)-n(3*i+2,:);
        v_BC = n(6,:)-d(f,:);
        v_CD = c(6,:)-n(6,:);

        length_AB = sqrt(dot(v_AB,v_AB));
        length_BC = sqrt(dot(v_BC,v_BC));
        length_CD = sqrt(dot(v_CD,v_CD));

        sin_ABC = sin(acos(dot(-v_AB,v_BC)/(length_AB*length_BC)));
        sin_BCD = sin(acos(dot(-v_BC,v_CD)/(length_BC*length_CD)));

        n_ABC = cross(v_AB,v_BC)/(length_AB*length_BC*sin_ABC);
        n_BCD = cross(v_BC,v_CD)/(length_BC*length_CD*sin_BCD);

        y(f,38+i) = acos(dot(n_ABC,n_BCD));

    end
```

137

```matlab
% N37-Cu57-N39-C3, N40-Cu57-N39-C3
    for i = 1:2,
        v_AB = d(f,:)-n(3*i+2,:);
        v_BC = n(7,:)-d(f,:);
        v_CD = c(3,:)-n(7,:);

        length_AB = sqrt(dot(v_AB,v_AB));
        length_BC = sqrt(dot(v_BC,v_BC));
        length_CD = sqrt(dot(v_CD,v_CD));

        sin_ABC = sin(acos(dot(-v_AB,v_BC)/(length_AB*length_BC)));
        sin_BCD = sin(acos(dot(-v_BC,v_CD)/(length_BC*length_CD)));

        n_ABC = cross(v_AB,v_BC)/(length_AB*length_BC*sin_ABC);
        n_BCD = cross(v_BC,v_CD)/(length_BC*length_CD*sin_BCD);

        y(f,40+i) = acos(dot(n_ABC,n_BCD));

    end

% N37-Cu57-N39-C7, N40-Cu57-N39-C7
    for i = 1:2,
        v_AB = d(f,:)-n(3*i+2,:);
        v_BC = n(7,:)-d(f,:);
        v_CD = c(7,:)-n(7,:);

        length_AB = sqrt(dot(v_AB,v_AB));
        length_BC = sqrt(dot(v_BC,v_BC));
        length_CD = sqrt(dot(v_CD,v_CD));

        sin_ABC = sin(acos(dot(-v_AB,v_BC)/(length_AB*length_BC)));
        sin_BCD = sin(acos(dot(-v_BC,v_CD)/(length_BC*length_CD)));

        n_ABC = cross(v_AB,v_BC)/(length_AB*length_BC*sin_ABC);
        n_BCD = cross(v_BC,v_CD)/(length_BC*length_CD*sin_BCD);

        y(f,42+i) = acos(dot(n_ABC,n_BCD));

    end

% N38-Cu57-N40-C4, N39-Cu57-N40-C4
    for i = 1:2,
        v_AB = d(f,:)-n(i+5,:);
        v_BC = n(8,:)-d(f,:);
        v_CD = c(4,:)-n(8,:);

        length_AB = sqrt(dot(v_AB,v_AB));
        length_BC = sqrt(dot(v_BC,v_BC));
        length_CD = sqrt(dot(v_CD,v_CD));

        sin_ABC = sin(acos(dot(-v_AB,v_BC)/(length_AB*length_BC)));
        sin_BCD = sin(acos(dot(-v_BC,v_CD)/(length_BC*length_CD)));
```

```
            n_ABC = cross(v_AB,v_BC)/(length_AB*length_BC*sin_ABC);
            n_BCD = cross(v_BC,v_CD)/(length_BC*length_CD*sin_BCD);

            y(f,44+i) = acos(dot(n_ABC,n_BCD));

        end

    % N38-Cu57-N40-C8, N39-Cu57-N40-C8
        for i = 1:2,
            v_AB = d(f,:)-n(i+5,:);
            v_BC = n(8,:)-d(f,:);
            v_CD = c(8,:)-n(8,:);

            length_AB = sqrt(dot(v_AB,v_AB));
            length_BC = sqrt(dot(v_BC,v_BC));
            length_CD = sqrt(dot(v_CD,v_CD));

            sin_ABC = sin(acos(dot(-v_AB,v_BC)/(length_AB*length_BC)));
            sin_BCD = sin(acos(dot(-v_BC,v_CD)/(length_BC*length_CD)));

            n_ABC = cross(v_AB,v_BC)/(length_AB*length_BC*sin_ABC);
            n_BCD = cross(v_BC,v_CD)/(length_BC*length_CD*sin_BCD);

            y(f,46+i) = acos(dot(n_ABC,n_BCD));

        end

    %Calculate 4 impropers: Cu57-N37-C1-C5, Cu57-N38-C2-C6, Cu57-N39-C3-C7,
    %Cu57-N40-C4-C8
        for i = 1:4,
            %Calculate 3 torsional angles
            v_AB = n(i+4,:)-d(f,:);
            v_BC = c(i,:)-n(i+4,:);
            v_CD = c(i+4,:)-c(i,:);

            length_AB = sqrt(dot(v_AB,v_AB));
            length_BC = sqrt(dot(v_BC,v_BC));
            length_CD = sqrt(dot(v_CD,v_CD));

            sin_ABC = sin(acos(dot(-v_AB,v_BC)/(length_AB*length_BC)));
            sin_BCD = sin(acos(dot(-v_BC,v_CD)/(length_BC*length_CD)));

            n_ABC = cross(v_AB,v_BC)/(length_AB*length_BC*sin_ABC);
            n_BCD = cross(v_BC,v_CD)/(length_BC*length_CD*sin_BCD);

            kai(1) = acos(dot(n_ABC,n_BCD));
            %second angle C-N-Cu-C'
            v_AB = n(i+4,:)-c(i,:);
            v_BC = c(i+4,:)-n(i+4,:);
            v_CD = d(f,:)-c(i+4,:);

            length_AB = sqrt(dot(v_AB,v_AB));
            length_BC = sqrt(dot(v_BC,v_BC));
            length_CD = sqrt(dot(v_CD,v_CD));
```

```
        sin_ABC = sin(acos(dot(-v_AB,v_BC)/(length_AB*length_BC)));
        sin_BCD = sin(acos(dot(-v_BC,v_CD)/(length_BC*length_CD)));

        n_ABC = cross(v_AB,v_BC)/(length_AB*length_BC*sin_ABC);
        n_BCD = cross(v_BC,v_CD)/(length_BC*length_CD*sin_BCD);

        kai(2) = acos(dot(n_ABC,n_BCD));
        %third angle
        v_AB = n(i+4,:)-c(i+4,:);
        v_BC = d(f,:)-n(i+4,:);
        v_CD = c(i,:)-d(f,:);

        length_AB = sqrt(dot(v_AB,v_AB));
        length_BC = sqrt(dot(v_BC,v_BC));
        length_CD = sqrt(dot(v_CD,v_CD));

        sin_ABC = sin(acos(dot(-v_AB,v_BC)/(length_AB*length_BC)));
        sin_BCD = sin(acos(dot(-v_BC,v_CD)/(length_BC*length_CD)));

        n_ABC = cross(v_AB,v_BC)/(length_AB*length_BC*sin_ABC);
        n_BCD = cross(v_BC,v_CD)/(length_BC*length_CD*sin_BCD);

        kai(3) = acos(dot(n_ABC,n_BCD));

        %average 3 angles
        y(f,48+i) = 1/3*(kai(1)+kai(2)+kai(3));
    end

end

% Starting guess of Coefs
x0 = [ 245,     -90,     -50, ...        Cu-N bond
        60,     -35,      15, ...        angle C-N-Cu
        60,     -35,      15, ...        angle N-Cu-N
         0,       1,       0, ...        dih of Cu-N-C-C
         0,       1,       0, ...        dih of Cu-N-C-N
        -7,      18,      -5, ...        dih of N-Cu-N-C
         5, ...                          improper Cu-N-C-C
        20, ...                          Ebb of N-Cu-N
        10, ...                          Eba of C-N-Cu
        20,      10, ...                 Eba of N-Cu-N
         0,       0,       0, ...        Embt of N-Cu-N-C
         0,       0,       0, ...        Eebt of Cu-N-C-C
         0,       0,       0, ...        Eebt of Cu-N-C-N
         0,       0,       0, ...        Eebt of N-Cu-N-C
         0,       0,       0, ...        Eat of Cu-N-C-C
         0,       0,       0, ...        Eat of Cu-N-C-N
         0,       0,       0, ...        Eat of N-Cu-N-C
         0];                             %Eaa of Cu-N-C-C

ub = [ 2000,    2000,    2000, ...       Cu-N bond
        100,     100,     100, ...       angle C-N-Cu
        100,     100,     100, ...       angle N-Cu-N
```

```
            10,    10,    10, ...          dih of Cu-N-C-C
            10,    10,    10, ...          dih of Cu-N-C-N
            20,    30,    10, ...          dih of N-Cu-N-C
            20, ...                        improper Cu-N-C-C
            100, ...                       Ebb of N-Cu-N
            100, ...                       Eba of C-N-Cu
            100,    50, ...                Eba of N-Cu-N
            30,    30,    30, ...          Embt of N-Cu-N-C
            10,    10,    10, ...          Eebt of Cu-N-C-C
            10,    10,    10, ...          Eebt of Cu-N-C-N
            10,    10,    10, ...          Eebt of N-Cu-N-C
            10,    10,    10, ...          Eat of Cu-N-C-C
            10,    10,    10, ...          Eat of Cu-N-C-N
            10,    10,    10, ...          Eat of N-Cu-N-C
            10];                           %Eaa of Cu-N-C-C

lb = -ub;


options = optimset('TolX',1e-15,'TolFun',1e-15,'MaxFunEvals',1000000);

[x,~,resnorm] = lsqcurvefit(@Fitting,x0,y,delE,lb,ub,options);




%%%%%%%%%%%%%%%%% Cu_coef %%%%%%%%%%%%%%%%%%%
function P = Fitting(x,y)
% potential takes Cu coordinates and calculated bond, angle, dihedral
% values to calculate the energy of the molecule. x are coefficient
% vectors containing 18 elements. y contains bonds, angles, dihedrals

b0 = 1.954;
ang0 = 125.8855/180.000*pi();   %Equilibrium angle of C-N-Cu
ang1 = pi()/2;                  %Equilibrium angle of 4 N-Cu-N


% Expression of the function P contains 3 parts: bonding, angle,
dihedral
%P =    sum((x(1)*(y(:,1:4)-b0).^2+x(2)*(y(:,1:4)-b0).^3+x(3)*(y(:,1:4)-
b0).^4),2)...                                  % x(1-3)    Cu-N Bonding
energy
P =    sum((245*(y(:,1:4)-b0).^2-88.9193*(y(:,1:4)-b0).^3-
55.4174*(y(:,1:4)-b0).^4),2)...                                 % x(1-
3)    Cu-N Bonding energy
    + sum((x(4)*(y(:,5:12)-ang0).^2+x(5)*(y(:,5:12)-
ang0).^3+x(6)*(y(:,5:12)-ang0).^4),2)...                        % x(4-
6)    angle of C-N-Cu
    + sum((x(7)*(y(:,13:16)-ang1).^2+x(8)*(y(:,13:16)-
ang1).^3+x(9)*(y(:,13:16)-ang1).^4),2)...                       % x(7-9)
angle of N-Cu-N
    + sum((x(10)*(1-cos(y(:,17:24)))+x(11)*(1-
```

```
cos(2*y(:,17:24)))+x(12)*(1-cos(3*y(:,17:24))))),2)...              %
x(10-12)    dih of Cu-N-C-C
    + sum((x(13)*(1-cos(y(:,25:32)))+x(14)*(1-
cos(2*y(:,25:32)))+x(15)*(1-cos(3*y(:,25:32))))),2)...             %
x(13-15)    dih of Cu-N-C-N
    + sum((x(16)*(1-cos(y(:,33:48)))+x(17)*(1-
cos(2*y(:,33:48)))+x(18)*(1-cos(3*y(:,33:48))))),2)...             %
x(16-18)    dih of N-Cu-N-C
    + sum((x(19)*(y(:,49:52)).^2),2)...
% x(19)     improper of Cu-N-C-C
    + sum((x(20)*((y(:,13)-b0).*(y(:,14)-b0)+(y(:,13)-b0).*(y(:,15)-
b0)+(y(:,13)-b0).*(y(:,16)-b0)...
    + (y(:,14)-b0).*(y(:,15)-b0)+(y(:,14)-b0).*(y(:,16)-b0)+(y(:,15)-
b0).*(y(:,16)-b0))),2)...                         % x(20)    Ebb of N-Cu-N
    + sum((x(21)*((y(:,1:4)-b0).*(y(:,5:8)-ang0)+(y(:,1:4)-
b0).*(y(:,9:12)-ang0))),2)...                     % x(21)    Eba
of C-N-Cu
    + sum((x(22)*(y(:,1)-b0).*(y(:,13)-ang0)+x(23)*(y(:,2)-
b0).*(y(:,13)-ang0)),2)...                        % x(22-23)
Eba of N-Cu-N
    + sum((x(22)*(y(:,3)-b0).*(y(:,14)-ang0)+x(23)*(y(:,4)-
b0).*(y(:,14)-ang0)),2)...                        % x(22-23)
Eba of N-Cu-N
    + sum((x(22)*(y(:,1)-b0).*(y(:,15)-ang0)+x(23)*(y(:,3)-
b0).*(y(:,15)-ang0)),2)...                        % x(22-23)
Eba of N-Cu-N
    + sum((x(22)*(y(:,2)-b0).*(y(:,16)-ang0)+x(23)*(y(:,4)-
b0).*(y(:,16)-ang0)),2)...                        % x(22-23)
Eba of N-Cu-N
    + sum((y(:,1)-b0).*(x(24)*(1-cos(y(:,33)))+x(25)*(1-
cos(2*y(:,33)))+x(26)*(1-cos(3*y(:,33)))),2)...        % x(24-26)
Embt of N-Cu-N-C
    + sum((y(:,1)-b0).*(x(24)*(1-cos(y(:,34)))+x(25)*(1-
cos(2*y(:,34)))+x(26)*(1-cos(3*y(:,34)))),2)...        % x(24-26)
Embt of N-Cu-N-C
    + sum((y(:,1)-b0).*(x(24)*(1-cos(y(:,35)))+x(25)*(1-
cos(2*y(:,35)))+x(26)*(1-cos(3*y(:,35)))),2)...        % x(24-26)
Embt of N-Cu-N-C
    + sum((y(:,1)-b0).*(x(24)*(1-cos(y(:,36)))+x(25)*(1-
cos(2*y(:,36)))+x(26)*(1-cos(3*y(:,36)))),2)...        % x(24-26)
Embt of N-Cu-N-C
    + sum((y(:,2)-b0).*(x(24)*(1-cos(y(:,37)))+x(25)*(1-
cos(2*y(:,37)))+x(26)*(1-cos(3*y(:,37)))),2)...        % x(24-26)
Embt of N-Cu-N-C
    + sum((y(:,2)-b0).*(x(24)*(1-cos(y(:,38)))+x(25)*(1-
cos(2*y(:,38)))+x(26)*(1-cos(3*y(:,38)))),2)...        % x(24-26)
Embt of N-Cu-N-C
    + sum((y(:,2)-b0).*(x(24)*(1-cos(y(:,39)))+x(25)*(1-
cos(2*y(:,39)))+x(26)*(1-cos(3*y(:,39)))),2)...        % x(24-26)
Embt of N-Cu-N-C
    + sum((y(:,2)-b0).*(x(24)*(1-cos(y(:,40)))+x(25)*(1-
cos(2*y(:,40)))+x(26)*(1-cos(3*y(:,40)))),2)...        % x(24-26)
Embt of N-Cu-N-C
    + sum((y(:,3)-b0).*(x(24)*(1-cos(y(:,41)))+x(25)*(1-
```

```
cos(2*y(:,41)))+x(26)*(1-cos(3*y(:,41)))),2)...            % x(24-26)
Embt of N-Cu-N-C
    + sum((y(:,3)-b0).*(x(24)*(1-cos(y(:,42)))+x(25)*(1-
cos(2*y(:,42)))+x(26)*(1-cos(3*y(:,42)))),2)...            % x(24-26)
Embt of N-Cu-N-C
    + sum((y(:,3)-b0).*(x(24)*(1-cos(y(:,43)))+x(25)*(1-
cos(2*y(:,43)))+x(26)*(1-cos(3*y(:,43)))),2)...            % x(24-26)
Embt of N-Cu-N-C
    + sum((y(:,3)-b0).*(x(24)*(1-cos(y(:,44)))+x(25)*(1-
cos(2*y(:,44)))+x(26)*(1-cos(3*y(:,44)))),2)...            % x(24-26)
Embt of N-Cu-N-C
    + sum((y(:,4)-b0).*(x(24)*(1-cos(y(:,45)))+x(25)*(1-
cos(2*y(:,45)))+x(26)*(1-cos(3*y(:,45)))),2)...            % x(24-26)
Embt of N-Cu-N-C
    + sum((y(:,4)-b0).*(x(24)*(1-cos(y(:,46)))+x(25)*(1-
cos(2*y(:,46)))+x(26)*(1-cos(3*y(:,46)))),2)...            % x(24-26)
Embt of N-Cu-N-C
    + sum((y(:,4)-b0).*(x(24)*(1-cos(y(:,47)))+x(25)*(1-
cos(2*y(:,47)))+x(26)*(1-cos(3*y(:,47)))),2)...            % x(24-26)
Embt of N-Cu-N-C
    + sum((y(:,4)-b0).*(x(24)*(1-cos(y(:,48)))+x(25)*(1-
cos(2*y(:,48)))+x(26)*(1-cos(3*y(:,48)))),2)...            % x(24-26)
Embt of N-Cu-N-C
    + sum((y(:,1:4)-b0).*(x(27)*(1-cos(y(:,17:20)))+x(28)*(1-
cos(2*y(:,17:20)))+x(29)*(1-cos(3*y(:,17:20)))),2)...  % x(27-29)
Eebt of Cu-N-C-C
    + sum((y(:,1:4)-b0).*(x(27)*(1-cos(y(:,21:24)))+x(28)*(1-
cos(2*y(:,21:24)))+x(29)*(1-cos(3*y(:,21:24)))),2)...  % x(27-29)
Eebt of Cu-N-C-C
    + sum((y(:,1)-b0).*(x(30)*(1-cos(y(:,25)))+x(31)*(1-
cos(2*y(:,25)))+x(32)*(1-cos(3*y(:,25)))),2)...            % x(30-32)
Eebt of Cu-N-C-N
    + sum((y(:,1)-b0).*(x(30)*(1-cos(y(:,26)))+x(31)*(1-
cos(2*y(:,26)))+x(32)*(1-cos(3*y(:,26)))),2)...            % x(30-32)
Eebt of Cu-N-C-N
    + sum((y(:,2)-b0).*(x(30)*(1-cos(y(:,27)))+x(31)*(1-
cos(2*y(:,27)))+x(32)*(1-cos(3*y(:,27)))),2)...            % x(30-32)
Eebt of Cu-N-C-N
    + sum((y(:,2)-b0).*(x(30)*(1-cos(y(:,28)))+x(31)*(1-
cos(2*y(:,28)))+x(32)*(1-cos(3*y(:,28)))),2)...            % x(30-32)
Eebt of Cu-N-C-N
    + sum((y(:,3)-b0).*(x(30)*(1-cos(y(:,29)))+x(31)*(1-
cos(2*y(:,29)))+x(32)*(1-cos(3*y(:,29)))),2)...            % x(30-32)
Eebt of Cu-N-C-N
    + sum((y(:,3)-b0).*(x(30)*(1-cos(y(:,30)))+x(31)*(1-
cos(2*y(:,30)))+x(32)*(1-cos(3*y(:,30)))),2)...            % x(30-32)
Eebt of Cu-N-C-N
    + sum((y(:,4)-b0).*(x(30)*(1-cos(y(:,31)))+x(31)*(1-
cos(2*y(:,31)))+x(32)*(1-cos(3*y(:,31)))),2)...            % x(30-32)
Eebt of Cu-N-C-N
    + sum((y(:,4)-b0).*(x(30)*(1-cos(y(:,32)))+x(31)*(1-
cos(2*y(:,32)))+x(32)*(1-cos(3*y(:,32)))),2)...            % x(30-32)
Eebt of Cu-N-C-N
    + sum((y(:,2)-b0).*(x(33)*(1-cos(y(:,33)))+x(34)*(1-
```

```
cos(2*y(:,33)))+x(35)*(1-cos(3*y(:,33)))),2)...          % x(33-35)
Eebt of N-Cu-N-C
    + sum((y(:,3)-b0).*(x(33)*(1-cos(y(:,34)))+x(34)*(1-
cos(2*y(:,34)))+x(35)*(1-cos(3*y(:,34)))),2)...          % x(33-35)
Eebt of N-Cu-N-C
    + sum((y(:,2)-b0).*(x(33)*(1-cos(y(:,35)))+x(34)*(1-
cos(2*y(:,35)))+x(35)*(1-cos(3*y(:,35)))),2)...          % x(33-35)
Eebt of N-Cu-N-C
    + sum((y(:,3)-b0).*(x(33)*(1-cos(y(:,36)))+x(34)*(1-
cos(2*y(:,36)))+x(35)*(1-cos(3*y(:,36)))),2)...          % x(33-35)
Eebt of N-Cu-N-C
    + sum((y(:,1)-b0).*(x(33)*(1-cos(y(:,37)))+x(34)*(1-
cos(2*y(:,37)))+x(35)*(1-cos(3*y(:,37)))),2)...          % x(33-35)
Eebt of N-Cu-N-C
    + sum((y(:,4)-b0).*(x(33)*(1-cos(y(:,38)))+x(34)*(1-
cos(2*y(:,38)))+x(35)*(1-cos(3*y(:,38)))),2)...          % x(33-35)
Eebt of N-Cu-N-C
    + sum((y(:,1)-b0).*(x(33)*(1-cos(y(:,39)))+x(34)*(1-
cos(2*y(:,39)))+x(35)*(1-cos(3*y(:,39)))),2)...          % x(33-35)
Eebt of N-Cu-N-C
    + sum((y(:,4)-b0).*(x(33)*(1-cos(y(:,40)))+x(34)*(1-
cos(2*y(:,40)))+x(35)*(1-cos(3*y(:,40)))),2)...          % x(33-35)
Eebt of N-Cu-N-C
    + sum((y(:,1)-b0).*(x(33)*(1-cos(y(:,41)))+x(34)*(1-
cos(2*y(:,41)))+x(35)*(1-cos(3*y(:,41)))),2)...          % x(33-35)
Eebt of N-Cu-N-C
    + sum((y(:,4)-b0).*(x(33)*(1-cos(y(:,42)))+x(34)*(1-
cos(2*y(:,42)))+x(35)*(1-cos(3*y(:,42)))),2)...          % x(33-35)
Eebt of N-Cu-N-C
    + sum((y(:,1)-b0).*(x(33)*(1-cos(y(:,43)))+x(34)*(1-
cos(2*y(:,43)))+x(35)*(1-cos(3*y(:,43)))),2)...          % x(33-35)
Eebt of N-Cu-N-C
    + sum((y(:,4)-b0).*(x(33)*(1-cos(y(:,44)))+x(34)*(1-
cos(2*y(:,44)))+x(35)*(1-cos(3*y(:,44)))),2)...          % x(33-35)
Eebt of N-Cu-N-C
    + sum((y(:,2)-b0).*(x(33)*(1-cos(y(:,45)))+x(34)*(1-
cos(2*y(:,45)))+x(35)*(1-cos(3*y(:,45)))),2)...          % x(33-35)
Eebt of N-Cu-N-C
    + sum((y(:,3)-b0).*(x(33)*(1-cos(y(:,46)))+x(34)*(1-
cos(2*y(:,46)))+x(35)*(1-cos(3*y(:,46)))),2)...          % x(33-35)
Eebt of N-Cu-N-C
    + sum((y(:,2)-b0).*(x(33)*(1-cos(y(:,47)))+x(34)*(1-
cos(2*y(:,47)))+x(35)*(1-cos(3*y(:,47)))),2)...          % x(33-35)
Eebt of N-Cu-N-C
    + sum((y(:,3)-b0).*(x(33)*(1-cos(y(:,48)))+x(34)*(1-
cos(2*y(:,48)))+x(35)*(1-cos(3*y(:,48)))),2)...          % x(33-35)
Eebt of N-Cu-N-C
    + sum((y(:,5:8)-ang0).*(x(36)*(1-cos(y(:,17:20)))+x(37)*(1-
cos(2*y(:,17:20)))+x(38)*(1-cos(3*y(:,17:20)))),2)...   % x(36-38)
Eat of Cu-N-C-C
    + sum((y(:,9:12)-ang0).*(x(36)*(1-cos(y(:,21:24)))+x(37)*(1-
cos(2*y(:,21:24)))+x(38)*(1-cos(3*y(:,21:24)))),2)...   % x(36-38)
Eat of Cu-N-C-C
    + sum((y(:,5)-ang0).*(x(39)*(1-cos(y(:,25)))+x(40)*(1-
```

```
cos(2*y(:,25)))+x(41)*(1-cos(3*y(:,25)))),2)...        % x(39-41)
Eat of Cu-N-C-N
    + sum((y(:,9)-ang0).*(x(39)*(1-cos(y(:,26)))+x(40)*(1-
cos(2*y(:,26)))+x(41)*(1-cos(3*y(:,26)))),2)...        % x(39-41)
Eat of Cu-N-C-N
    + sum((y(:,6)-ang0).*(x(39)*(1-cos(y(:,27)))+x(40)*(1-
cos(2*y(:,27)))+x(41)*(1-cos(3*y(:,27)))),2)...        % x(39-41)
Eat of Cu-N-C-N
    + sum((y(:,10)-ang0).*(x(39)*(1-cos(y(:,28)))+x(40)*(1-
cos(2*y(:,28)))+x(41)*(1-cos(3*y(:,28)))),2)...        % x(39-41)
Eat of Cu-N-C-N
    + sum((y(:,7)-ang0).*(x(39)*(1-cos(y(:,29)))+x(40)*(1-
cos(2*y(:,29)))+x(41)*(1-cos(3*y(:,29)))),2)...        % x(39-41)
Eat of Cu-N-C-N
    + sum((y(:,11)-ang0).*(x(39)*(1-cos(y(:,30)))+x(40)*(1-
cos(2*y(:,30)))+x(41)*(1-cos(3*y(:,30)))),2)...        % x(39-41)
Eat of Cu-N-C-N
    + sum((y(:,8)-ang0).*(x(39)*(1-cos(y(:,31)))+x(40)*(1-
cos(2*y(:,31)))+x(41)*(1-cos(3*y(:,31)))),2)...        % x(39-41)
Eat of Cu-N-C-N
    + sum((y(:,12)-ang0).*(x(39)*(1-cos(y(:,32)))+x(40)*(1-
cos(2*y(:,32)))+x(41)*(1-cos(3*y(:,32)))),2)...        % x(39-41)
Eat of Cu-N-C-N
    + sum((y(:,13)-ang1).*(x(42)*(1-cos(y(:,33)))+x(43)*(1-
cos(2*y(:,33)))+x(44)*(1-cos(3*y(:,33)))),2)...        % x(42-44)
Eat of N-Cu-N-C
    + sum((y(:,15)-ang1).*(x(42)*(1-cos(y(:,34)))+x(43)*(1-
cos(2*y(:,34)))+x(44)*(1-cos(3*y(:,34)))),2)...        % x(42-44)
Eat of N-Cu-N-C
    + sum((y(:,13)-ang1).*(x(42)*(1-cos(y(:,35)))+x(43)*(1-
cos(2*y(:,35)))+x(44)*(1-cos(3*y(:,35)))),2)...        % x(42-44)
Eat of N-Cu-N-C
    + sum((y(:,15)-ang1).*(x(42)*(1-cos(y(:,36)))+x(43)*(1-
cos(2*y(:,36)))+x(44)*(1-cos(3*y(:,36)))),2)...        % x(42-44)
Eat of N-Cu-N-C
    + sum((y(:,13)-ang1).*(x(42)*(1-cos(y(:,37)))+x(43)*(1-
cos(2*y(:,37)))+x(44)*(1-cos(3*y(:,37)))),2)...        % x(42-44)
Eat of N-Cu-N-C
    + sum((y(:,16)-ang1).*(x(42)*(1-cos(y(:,38)))+x(43)*(1-
cos(2*y(:,38)))+x(44)*(1-cos(3*y(:,38)))),2)...        % x(42-44)
Eat of N-Cu-N-C
    + sum((y(:,13)-ang1).*(x(42)*(1-cos(y(:,39)))+x(43)*(1-
cos(2*y(:,39)))+x(44)*(1-cos(3*y(:,39)))),2)...        % x(42-44)
Eat of N-Cu-N-C
    + sum((y(:,16)-ang1).*(x(42)*(1-cos(y(:,40)))+x(43)*(1-
cos(2*y(:,40)))+x(44)*(1-cos(3*y(:,40)))),2)...        % x(42-44)
Eat of N-Cu-N-C
    + sum((y(:,15)-ang1).*(x(42)*(1-cos(y(:,41)))+x(43)*(1-
cos(2*y(:,41)))+x(44)*(1-cos(3*y(:,41)))),2)...        % x(42-44)
Eat of N-Cu-N-C
    + sum((y(:,14)-ang1).*(x(42)*(1-cos(y(:,42)))+x(43)*(1-
cos(2*y(:,42)))+x(44)*(1-cos(3*y(:,42)))),2)...        % x(42-44)
Eat of N-Cu-N-C
    + sum((y(:,15)-ang1).*(x(42)*(1-cos(y(:,43)))+x(43)*(1-
```

```
cos(2*y(:,43)))+x(44)*(1-cos(3*y(:,43)))),2)...        % x(42-44)
Eat of N-Cu-N-C
    + sum((y(:,14)-ang1).*(x(42)*(1-cos(y(:,44)))+x(43)*(1-
cos(2*y(:,44)))+x(44)*(1-cos(3*y(:,44)))),2)...        % x(42-44)
Eat of N-Cu-N-C
    + sum((y(:,16)-ang1).*(x(42)*(1-cos(y(:,45)))+x(43)*(1-
cos(2*y(:,45)))+x(44)*(1-cos(3*y(:,45)))),2)...        % x(42-44)
Eat of N-Cu-N-C
    + sum((y(:,14)-ang1).*(x(42)*(1-cos(y(:,46)))+x(43)*(1-
cos(2*y(:,46)))+x(44)*(1-cos(3*y(:,46)))),2)...        % x(42-44)
Eat of N-Cu-N-C
    + sum((y(:,16)-ang1).*(x(42)*(1-cos(y(:,47)))+x(43)*(1-
cos(2*y(:,47)))+x(44)*(1-cos(3*y(:,47)))),2)...        % x(42-44)
Eat of N-Cu-N-C
    + sum((y(:,14)-ang1).*(x(42)*(1-cos(y(:,48)))+x(43)*(1-
cos(2*y(:,48)))+x(44)*(1-cos(3*y(:,48)))),2)...        % x(42-44)
Eat of N-Cu-N-C
    + sum((x(45)*(y(:,5:8)-ang0).*(y(:,9:12)-ang0)),2);
% x(45)    Eaa of Cu-N-C-C


end
%%%%%%%%%%%%%%%%%%%%%%%%%%%%%%%%%%%%%%%%%%%%%%
```

Appendix B Source code for LAMMPS extensions

B1   compute style: dipole

Syntax:

```
compute ID group-ID dipole
```
- ID, group-ID are documented in <u>compute</u> command on LAMMPS website
- dipole = style name of this compute command

Examples:

```
compute 1 all dipole
compute myDipole mobile dipole
```

Description:

Define a computation that calculates the net dipole moment of a group of atoms.

This compute will output a global vector of length 4. First 3 elements of the vector will be the net dipole moment in x, y, and z direction. The fourth element will be the net positive charge of the atoms in the group.

The number of atoms contributing to the temperature is assumed to be constant for the duration of the run; use the *dynamic* option of the <u>compute_modify</u> command if this is not the case.

Header file:

```
/* -------------------------------------------------------------
--------
 Lammps compute to calculate net dipole moment
 Author: Chen Shao, MSE, University of Michigan
 -------------------------------------------------------------
--------- */

#ifdef COMPUTE_CLASS

ComputeStyle(dipole,ComputeDipole)
```

```cpp
#else

#ifndef LMP_COMPUTE_DIPOLE_H
#define LMP_COMPUTE_DIPOLE_H

#include "compute.h"

namespace LAMMPS_NS {

class ComputeDipole : public Compute {
 public:
  ComputeDipole(class LAMMPS *, int, char **);
  virtual ~ComputeDipole();
  void init();
  void compute_vector();

};

}

#endif
#endif

/* ERROR/WARNING messages:

E: Illegal ... command

Self-explanatory.  Check the input script syntax and compare to
the
documentation for the command.  You can use -echo screen as a
command-line option when running LAMMPS to see the offending
line.

*/
```

cpp file:

```cpp
/* ----------------------------------------------------------------
--------
 Lammps compute to calculate net dipole moment
 Author: Chen Shao, MSE, University of Michigan
 ----------------------------------------------------------------
--------- */

#include "mpi.h"
#include "compute_dipole.h"
```

```cpp
#include "atom.h"
#include "update.h"
#include "force.h"
#include "domain.h"
#include "group.h"
#include "error.h"

using namespace LAMMPS_NS;

/* ----------------------------------------------------------------
---------- */

ComputeDipole::ComputeDipole(LAMMPS *lmp, int narg, char **arg) :
Compute(lmp, narg, arg)
{
    if (narg != 3) error->all(FLERR,"Illegal compute dipole
command");

    vector_flag = 1;
    size_vector = 4;
    extvector = 1;

    vector = new double[4];
}

/* ----------------------------------------------------------------
---------- */

ComputeDipole::~ComputeDipole()
{
    delete [] vector;
}

/* ----------------------------------------------------------------
---------- */

void ComputeDipole::init()
{

}

/* ----------------------------------------------------------------
---------- */

void ComputeDipole::compute_vector()
{
    invoked_vector = update->ntimestep;

    double **x= atom->x;
```

```
        double *q = atom->q;
        int *mask = atom->mask;
        int *type = atom->type;
        int nlocal = atom->nlocal;
        double netq = 0.0;

        double D[3];

        int i,j;

        for (i = 0; i < 3; i++) D[i] = 0.0;

/*
        for (i = 0; i < nlocal; i++) {
         if (mask[i] & groupbit) {
              if (q[i] > 0) netq += q[i];
         }
        }
*/

        // simulation box bounds
        double *boxlo = domain->boxlo;
        double *boxhi = domain->boxhi;

        for (i = 0; i < nlocal; i++) {
         int xbox = (atom->image[i] & IMGMASK) - IMGMAX;
         int ybox = (atom->image[i] >> IMGBITS & IMGMASK) - IMGMAX;
         int zbox = (atom->image[i] >> IMG2BITS) - IMGMAX;

         if (mask[i] & groupbit) {
              if (q[i] > 0) netq += q[i];
              D[0] += q[i]*(x[i][0] + xbox*(boxhi[0]-boxlo[0]));
              D[1] += q[i]*(x[i][1] + ybox*(boxhi[1]-boxlo[1]));
              D[2] += q[i]*(x[i][2] + zbox*(boxhi[2]-boxlo[2]));
         }
        }

        double data[4] = {D[0],D[1],D[2],netq};
        MPI_Allreduce(data,vector,4,MPI_DOUBLE,MPI_SUM,world);
}
```

B2   fix style: vacf

Syntax:

```
fix ID group-ID vacf correlation-length filename
```
- ID, group-ID are documented in [fix](fix) command
- vacf = style name of this compute command
- correlation-length = time length of the correlation function
- filename = file where vacf results will be outputed

Examples:

```
fix 1 all vacf 1024 log.vacf
fix 1 mobile vacf 20000 myVacf
```

Description:

Define a fix that calculates the velocity autocorrelation function (VACF) of a group of atoms. This fix will calculate the average of the correlation function over all the atoms in the group and over all time steps.

This fix will sample every timestep to calculate VACF. During the simulation, this fix will generate a global vector of length correlation-length to store the calculation results. When simulation is finished, this fix will output the final result into the file specified. Take a discrete Fourier transform on the calculated velocity autocorrelaiton function will result in a power spectrum of the system, which is essentially the vibrational density of states.

The number of atoms contributing to the temperature is assumed to be constant for the duration of the run; use the *dynamic* option of the compute_modify command if this is not the case.

Output info:

This fix will output the calculation results at the end of the fix. If the specied file is already existed, new file will overwrite the old file.

Header file:

```cpp
/* ----------------------------------------------------------------
--------
 Lammps fix to calculate velocity auto-correlation function
 Author: Chen Shao, MSE, University of Michigan
 ----------------------------------------------------------------
--------- */

#ifdef FIX_CLASS

FixStyle(vacf,FixVacf)

#else

#ifndef LMP_FIX_VACF_H
#define LMP_FIX_VACF_H

#include "stdio.h"
#include "fix.h"

namespace LAMMPS_NS {

    class FixVacf : public Fix {
    public:
     FixVacf(class LAMMPS *, int, char **);
     ~FixVacf();
     int setmask();
     void init();
     void setup(int);
     void end_of_step();
     void reset_timestep(bigint);

    private:
     int me,nvalues;
     int nrepeat,nfreq,irepeat;
     bigint nvalid;
     int *which,*argindex,*value2index,*offcol;
     char **ids;
     FILE *fp;
     int nrows;
     long filepos;

     double *result;
     double ***data;


     int firstindex;      // index in values ring of earliest
time sample
     int startstep;
     int nlocal;
```

```
        int *count;

        void accumulate();
        bigint nextvalid();
    };

}

#endif
#endif

/* ERROR/WARNING messages:

 E: Illegal ... command

 Self-explanatory.  Check the input script syntax and compare to
the
 documentation for the command.  You can use -echo screen as a
 command-line option when running LAMMPS to see the offending
line.

 E: Cannot open fix ave/correlate file %s

 The specified file cannot be opened.  Check that the path and
name are
 correct.

 E: Compute ID for fix ave/correlate does not exist

 Self-explanatory.

 E: Fix ave/correlate compute does not calculate a scalar

 Self-explanatory.

 E: Fix ave/correlate compute does not calculate a vector

 Self-explanatory.

 E: Fix ave/correlate compute vector is accessed out-of-range

 The index for the vector is out of bounds.

 E: Fix ID for fix ave/correlate does not exist

 Self-explanatory.

 E: Fix ave/correlate fix does not calculate a scalar
```

Self-explanatory.

 E: Fix ave/correlate fix does not calculate a vector

 Self-explanatory.

 E: Fix ave/correlate fix vector is accessed out-of-range

 The index for the vector is out of bounds.

 E: Fix for fix ave/correlate not computed at compatible time

 Fixes generate their values on specific timesteps. Fix ave/correlate
 is requesting a value on a non-allowed timestep.

 E: Variable name for fix ave/correlate does not exist

 Self-explanatory.

 E: Fix ave/correlate variable is not equal-style variable

 Self-explanatory.

 E: Fix ave/correlate missed timestep

 You cannot reset the timestep to a value beyond where the fix
 expects to next perform averaging.

 */

cpp file:

```
/* ----------------------------------------------------------------
--------
Lammps fix to calculate velocity auto-correlation function
 Author: Chen Shao, MSE, University of Michigan
------------------------------------------------------------------
-------- */

#include "stdlib.h"
#include "string.h"
#include "fix_vacf.h"
#include "update.h"
#include "modify.h"
#include "compute.h"
```

```cpp
#include "input.h"
#include "variable.h"
#include "memory.h"
#include "error.h"
#include "atom.h"

using namespace LAMMPS_NS;
using namespace FixConst;

#define INVOKED_SCALAR 1
#define INVOKED_VECTOR 2
#define INVOKED_ARRAY 4

/* ----------------------------------------------------------------
---------- */

FixVacf::FixVacf(LAMMPS * lmp, int narg, char **arg):
Fix (lmp, narg, arg)
{
    if (narg < 5) error->all(FLERR,"Illegal fix vacf command");

    MPI_Comm_rank(world,&me);

    nevery = 1; //atoi(arg[3]);
    nrepeat = atoi(arg[3]);
    nfreq = atoi(arg[3]);

    global_freq = nfreq;

    int iarg = 4;

    // we will use atomic velocities as input
    which = argindex = value2index = offcol = NULL;
    ids = NULL;
    int maxvalues = nvalues = 0;

    // setup and error check
    // for fix inputs, check that fix frequency is acceptable
    if (nevery <= 0 || nrepeat <= 0 || nfreq <= 0)
     error->all(FLERR,"Illegal fix vacf command");
    if (nfreq % nevery || (nrepeat-1)*nevery >= nfreq)
     error->all(FLERR,"Illegal fix vacf command");

    // print file comment lines
    fp = fopen(arg[iarg],"w+");
    if (fp && me == 0) {
     fprintf(fp,"# Velocity autocorrelation data\n");
     fprintf(fp,"# Correlation-Timestep Count VACF\n");
     //filepos = ftell(fp);
```

```
}

firstindex = 0;
startstep = 0;

// this fix produces a global intensive vector
extvector = 1;
size_vector = nrepeat + 1;

// Allocate memory
nlocal = atom->nlocal;
result = NULL;
count = NULL;
data = NULL;
memory->create(result,nrepeat+1,"vacf:result");
memory->create(count,nrepeat+1,"vacf:count");
memory->create(data,nrepeat+1,nlocal,3,"vacf:data");


//vacf_result = new double[nrepeat + 1];
//vacf_count = new int[nrepeat + 1];
/**
 // Allocate memory
 int i,j;

 data = new double**[nrepeat + 1];
 for (i = 0; i < nrepeat + 1; ++i) {
 data[i] = new double*[nlocal];

 for (j = 0; j < nlocal; ++j)
 data[i][j] = new double[3];
 }
 **/

// initialization
for (int i=0; i<nrepeat+1; i++) {
 for (int j=0; j<nlocal; j++) {
      for (int k=0; k<3; k++) {
           data[i][j][k] = 0.0;
      }
 }
}

for (int i = 0; i < nrepeat + 1; i++) {
 result[i] = 0.0;
 count[i] = 0;
}
```

```cpp
    // nvalid = next step on which end_of_step does something
    // add nvalid to all computes that store invocation times
    // since don't know a priori which are invoked by this fix
    // once in end_of_step() can set timestep for ones actually
invoked

    nvalid = nextvalid();
    modify->addstep_compute_all(nvalid);

}

/* ----------------------------------------------------------------
-------- */

FixVacf::~FixVacf()
{
    if (fp && me == 0) {
      bigint ntimestep = update->ntimestep;
      fprintf(fp,BIGINT_FORMAT "\n",ntimestep);
      for (int i = 0; i < nrepeat+1; i++) {
          fprintf(fp,"%d %g",i,result[i]/count[i]);
          //fprintf(fp," %g %g
%g",data[i][1][0],data[i][1][1],data[i][1][2]);
          fprintf(fp,"\n");
      }
      fflush(fp);
      fclose(fp);
    }

    memory->destroy(result);
    memory->destroy(count);
    memory->destroy(data);
    /**
     for (int i = 0; i < nrepeat; i++) {
     for (int j=0; j<nlocal; j++)
     delete [] vacf_data[i][j];
     delete [] vacf_data[i];
     }
     delete [] vacf_result;
     delete [] vacf_count;
     **/
    //if (fp && me == 0) fclose(fp);
}

/* ----------------------------------------------------------------
-------- */

int FixVacf::setmask()
{
```

```cpp
    int mask = 0;
    mask |= END_OF_STEP;
    return mask;
}

/* ------------------------------------------------------------
-------- */

void FixVacf::init()
{

}

/* ------------------------------------------------------------
--------
 only does something if nvalid = current timestep
 ------------------------------------------------------------
--------- */

void FixVacf::setup(int vflag)
{
    end_of_step();
}

/* ------------------------------------------------------------
-------- */

void FixVacf::end_of_step()
{
    // output result to file
    bigint ntimestep = update->ntimestep;
    double **tmp = atom->v;

    int i, j, k;
    if (firstindex <= nrepeat) {
     // copy atom velocities into data
      for (i=0; i<nlocal; i++) {
            for (j=0; j<3; j++) {
                    data[firstindex][i][j] = tmp[i][j];
            }
      }
      firstindex++;
    } else {
      //fprintf(fp," %g %g
%g",data[0][1][0],data[0][1][1],data[0][1][2]);
      // update stored velocities
      for (i=0; i<nrepeat; i++) {
            for (j=0; j<nlocal; j++) {
                    for (k=0; k<3; k++) {
```

```
                            data[i][j][k] = data[i+1][j][k];
                    }
            }
        }

        for (i=0; i<nlocal; i++) {
            for (j=0; j<3; j++) {
                    data[nrepeat][i][j] = tmp[i][j];
            }
        }

        // calculate all vacf
        accumulate();
        firstindex++;
    }

    //delete []tmp;
    /**
    if (fp && me == 0) {
      fprintf(fp,BIGINT_FORMAT "\n",ntimestep);
      for (i = 0; i < nrepeat+1; i++) {
            fprintf(fp,"%d %g",i,result[i]/count[i]);
            //fprintf(fp," %g %g
%g",data[i][1][0],data[i][1][1],data[i][1][2]);
            fprintf(fp,"\n");
      }
      fflush(fp);
    }
    **/
}

/* ----------------------------------------------------------------
--------
  accumulate correlation data using more recently added values
  ----------------------------------------------------------------
--------- */

void FixVacf::accumulate()
{
    int i,j,k;
    double tmp;
    for (k = 0; k < nrepeat+1; k++) {
     count[k]++;
     tmp = 0.0;
     for (i=0; i<nlocal; i++) {
            for (j=0; j<3; j++) {
                    tmp += data[0][i][j]*data[0+k][i][j];
            }
     }
```

159

```
        result[k] += tmp/nlocal;
    }
}


/* ----------------------------------------------------------------
--------
 calculate nvalid = next step on which end_of_step does something
 can be this timestep if multiple of nfreq and nrepeat = 1
 else backup from next multiple of nfreq
 startstep is lower bound on nfreq multiple
 ----------------------------------------------------------------
--------- */

bigint FixVacf::nextvalid()
{
    bigint nvalid = (update->ntimestep/nfreq)*nfreq + nfreq;
    while (nvalid < startstep) nvalid += nfreq;
    if (nvalid-nfreq == update->ntimestep && nrepeat == 1)
     nvalid = update->ntimestep;
    else
     nvalid -= (nrepeat-1)*nevery;
    if (nvalid < update->ntimestep) nvalid += nfreq;
    return nvalid;
}

/* ----------------------------------------------------------------
-------- */

void FixVacf::reset_timestep(bigint ntimestep)
{
    if (ntimestep > nvalid) error->all(FLERR,"Fix vacf missed
timestep");
}
```